# Bilateral Macro-Micro Teleoperation Using A Magnetic Actuation Mechanism

by

Moein Mehrtash

A thesis
presented to the University of Waterloo
in fulfillment of the
thesis requirement for the degree of
Doctor of Philosophy
in
Mechanical Engineering

Waterloo, Ontario, Canada, 2013

I hereby declare that I am the sole author of this thesis. This is a true copy of the thesis, including any required final revisions, as accepted by my examiners.

I understand that my thesis may be made electronically available to the public.

# Abstract

In recent years, there has been increasing interest in the advancement of micro-robotic systems in micro-engineering, micro-fabrication, biological research and biomedical applications. Untethered magnetic-based microrobotic systems are one of the most widely developing groups of microrobotic systems that have been extensively explored for biological and biomedical micro-manipulations. These systems show promise in resolving problems related to on-board power supply limitations as well as mechanical contact sealing and lubrication. In this thesis, a high precision magnetic untethered microrobotic system is demonstrated for micro-handling tasks. A key aspect of the proposed platform concerns the integration of magnetic levitation technology and bilateral macro-micro teleoperation for human intervention to avoid imperceptible failures in poorly observed micro-domain environments.

The developed platform has three basic subsystems: a magnetic untethered microrobotic system (MUMS), a haptic device, and a scaled bilateral teleoperation system. The MUMS produces and regulates a magnetic field for non-contact propelling of a microrobot. In order to achieve a controlled motion of the magnetically levitated microrobot, a mathematical force model of the magnetic propulsion mechanism is developed and used to design various control systems. In the workspace of $30 \times 32 \times 32 \ mm^3$, both PID and LQG\LTR controllers perform similarly the position accuracy of 10 $\mu$m in a vertical direction and 2 $\mu$m in a horizontal motion.

The MUMS is equipped with an eddy-current damper to enhance its inherent damping factor in the microrobot's horizontal motions. This paper deals with the modeling and analysis of an eddy-current damper that is formed by a conductive plate placed below the levitated microrobot to overcome inherent dynamical vibrations and improve motion precision. The modeling of eddy-current distribution in the conductive plate is investigated by solving the diffusion equation for vector magnetic potential, and an analytical expression for the horizontal damping force is presented and experimentally validated. It is demonstrated that eddy-current damping is a crucial technique for increasing the damping coefficient in a non-contact way and for improving levitation performance. The damping can be

widely used in applications of magnetic actuation systems in micro-manipulation and micro-fabrication.

To determine the position of the microrobot in a workspace, the MUMS uses high-accuracy laser sensors. However, laser positioning techniques can only be used in highly transparent environments. A novel technique based on real-time magnetic flux measurement has been proposed for the position estimation of the microrobot in case of laser beam blockage, whereby a combination of Hall-effect sensors is employed to find the microrobot's position in free motion by using the produced magnetic flux. In free motion, the microrobot tends to move toward the horizontally zero magnetic field gradient, $B_{max}$ location. As another key feature of the magnetic flux measurement, it was realized that the applied force from the environment to the microrobot can be estimated as linearly proportional to the distance of the microrobot from the $B_{max}$ location. The developed micro-domain force estimation method is verified experimentally with an accuracy of 1.27 $\mu$N.

A bilateral macro-micro teleoperation technique is employed in the MUMS for the telepresence of a human operator in the task environment. A gain-switching position-position teleoperation scheme is employed and a human operator controls the motion of the microrobot via a master manipulator for dexterous micro-manipulation tasks. The operator can sense a strong force during micro-domain tasks if the microrobot encounters a stiff environment, and the effect of hard contact is fed back to the operator's hand. The position-position method works for both free motion and hard contact. However, to enhance the feeling of a micro-domain environment in the human operator, the scaled force must be transferred to a human, thereby realizing a direct-force-reflection bilateral teleoperation. Additionally, a human-assisted virtual reality interface is developed to improve a human operator's skills in using the haptic-enabled platform, before carrying out an actual dexterous task.

## Acknowledgements

First and foremost, I would like to express my sincere gratitude to my advisor Dr. M. B. Khamesee for the continuous support of my Ph.D study and research, for his patience, motivation, enthusiasm, and immense knowledge. His guidance helped me in all the time of research and writing of this thesis.

Besides my advisor, I owe a debt of gratitude to my committee members Dr. Jan P. Huissoon, Dr. Eihab Abdel-Rahman, and Dr. Soo Jeon for serving in my examination. I would like to thank Dr. Pierre E. Dupont for participating in my defence exam as the external member and providing invaluable feedback.

Thank you to Mohsen Baratvand, Dr. Javad Behruzi, Dr. Pooya Mahboubi, Dr. Babak Ebrahimi, Dr. Ehsan Shameli, Dr. Caglar Elbuken, Dr. Payam Azizi, Saman Nasirahmadi, Bahador Biglari, and Mostafa Mehrtash. it is their endless friendship, moral support and inspirational advice that I will never ever forget throughout my life. Thank you all to my dearest friends and brain-mates.

I extend my deepest heartfelt thanks to my family for their faithful support and confidence in me. I would always be indebted to them.

# Contents

# List of Tables

# List of Figures

xiii

# Chapter 1

# Introduction

The past decade has seen the rapid development of micro- and nano-based systems across various disciplines, such as microsurgery, biological/biomedical manipulations, optics, and micro-devices. However, the development of high precision devices for machining, assembly and manipulation present some challenges in the development of microsystem tools. Although intense research has been undertaken on the fabrication of MEMS[1] and MOEMS[2], few studies have explored the field of micro-assembly, micro-manipulation and bio-micromanipulation. The first generation of micro-manipulation systems involves semiconductor manufacturing techniques that offer promising results for mass production. However, these costly systems have not been well adapted (low flexibility) for human hand-operated tasks, such as cell micro-manipulation, microsurgery or micro-assembly of small series micro-products. In comparison with manipulation in the macro-world, the main research in micromanipulations is focused on: 1) the design and manufacturing of miniaturized parts, and 2) the modeling complexities of scaling effect phenomena in micro- and nano-domain environments[3].

The miniaturization of macro-world manipulation techniques incorporates the advancement of the micro-domain actuators, sensors, electrical circuits, and power supplies. However, these modules have not been well modified for minia-

---

[1]1micro-electro-mechanical-systems

[2]micro-opto-electro-mechanical systems

[3]The insignificant un-modeled forces in the macro-world such as friction and adhesion act as dominant sources of force in the micro-world [95]

turized applications, and their integration restricts the construction of micro- and nano-based manipulation platforms.

In addition, the generally poor understating of micro-domain physical properties causes dilemmas in the design of micro-manipulation systems, as the accurate mathematical modeling of systems for automatic micro-manipulation is indispensable. A substantial and growing body of literature has reported solutions consisting either of accurate mathematical models of micro-mechanics and micro-mechanisms or human interventions to enhance the performance of micro-manipulation tasks.

In order to satisfy the need for low cost, high accuracy, high flexibility and bio-compatibility, a novel research-made micro-manipulation platform was developed from scratch at the Maglev Microrobotics Lab, University of Waterloo. This thesis addresses micro-manipulation challenges by a non-contact-actuated mechanism using a controlled magnetic field. A magnetic drive unit is designed to produce and regulate the magnetic field for the non-contact propelling of a micro-robot, which consists of a magnetic head, electronic circuits, and an end-effector. By integrating this magnetic-based mechanism with a haptic interface, the human operator intervenes in dexterous micro-manipulations or micro-assemblies to compensate the lack of information from the micro-task's environment

## 1.1  Microrobotic Platform Literature Review [1]

This research deals with numerous challenges across various disciplines. The present section starts with a comprehensive literature review discussing the advantages, limitations and drawbacks of various micro-manipulation techniques. A general overview of magnetic-based actuation technology is subsequently carried out, followed by a literature review of human intervention importance and proposed solutions for reliable micro-manipulation follows in Section 1.1.3. As a final

---

[1]Portions of this section are published by Moein Mehrtash and Mir Behrad Khamesee, Design and Implementation of LQG/LTR Controller for a Magnetic Tele-manipulation System-Performance Evaluation and Energy Saving, Microsystem Technologies, 17(5-7), pp. 1145-1152 and Moein Mehrtash, Noaoki Tsuda, and Mir Behrad Khamesee, Bilateral Macro-Micro Tele-operation Using Magnetic Levitation, Mechatronics, IEEE/ASME Transactions on, 16(3),pp. 459-469

point in this chapter, the research objective statement and outline are provided.

### 1.1.1  Review of Micro-manipulation

A considerable amount of research has been devoted to micro-to-nano-sized object manipulation with micron or sub-micron precision. Based on the overall review of these studies, the micro-manipulation techniques can be categorized in several different ways, depending on the application and manipulation environment. According to the interaction mechanism between the tool and the manipulated object, the micro-manipulation can generally be classified into "non-contact" and "contact" types.

**Non-contact Methods**

The currently developed non-contact micro-manipulation techniques are optical trapping [4], magnetic tweezers [44; 108], and electric trapping [5]. Additionally, there are numerous contact micro-manipulation methods that have been developed based on microrobotic technologies such as atomic force microscopy (AFM), probe-based micro-manipulators, micro-positioners, and micro-grippers. All of these techniques provide manipulation in various scales and applications (Fig. 1.1). Figure 1.1 presents some examples of manipulated objects and required precision for various tasks.

Non-contact micro-manipulation methods have been recently applied to realize the manipulation of particles and biological cells. Despite their promise, these techniques nonetheless lack the dexterity to undertake complex tasks that involve maneuvering in relatively unreachable environments. Such a non-contact method is called optical trapping. In this method, a laser beam is focused on a dielectric object, which has higher refractive index than the surrounding environment, and a polarizing force is applied to the manipulated object in the direction of the laser beam's focal point. By changing the focal point of the laser beam, the manipulated object can then be moved.

However, there are some major drawbacks of this method. First of all, the produced trapping force is in the sub-pN range, so that it can be used for gentle movement of small particles, single DNA molecule [105] or cells [104; 117].
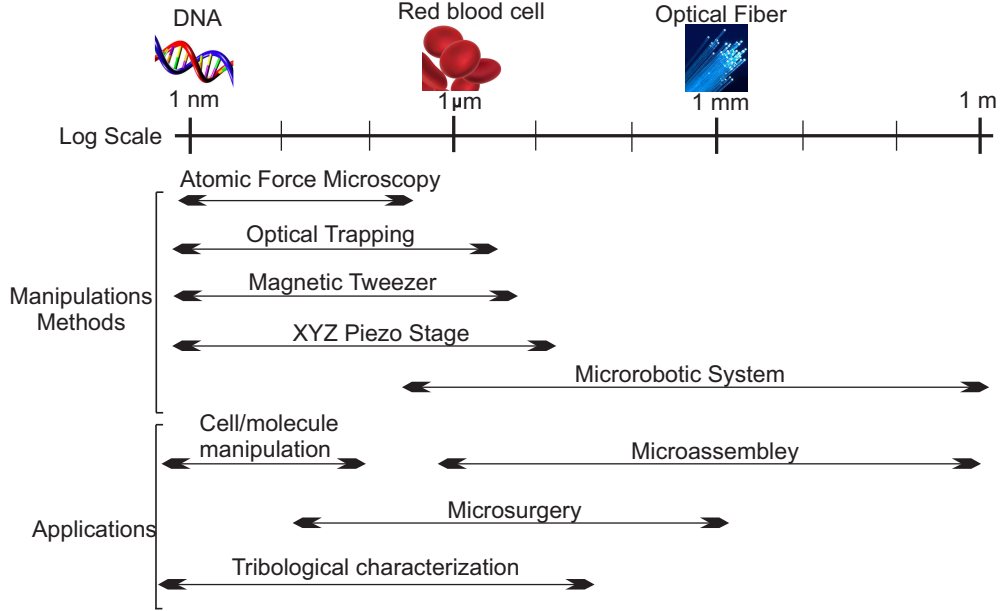
Figure 1.1: The operational working envelopes and applications of micromanipulation techniques [32; 66; 88]

Secondly, a polarizing force can be applied to dielectric materials only. Thus, for the manipulation of conductive objects, a dielectric micro-bead must be attached to the object, which is a labor-intensive task. A third drawback is that a high intensity light source can cause photo-damage to the living objects for bio-micromanipulation applications [24].

In addition, dielectrophoresis (DEP) and electrorotation are two other non-contact techniques have been proposed for micro/nano manipulation. These techniques involve the manipulation of dielectric particles using electric fields. The gas bubbling formation (electrolytic process) in aqueous environments and the increase of the environment's temperature are two main restrictions of using an electric field for micro-manipulation in bio-applications, as these restrictions can also damage living cells, bacteria, and DNA [24].Nonetheless, magnetic micro-manipulation shows enormous potential in micro-assembly and bio-micromanipulation, whereby ferromagnetic objects can be manipulated with an external source magnetic field [64; 109]. The magnetic manipulation is preferred over optical and electric methods for bi-micromanipulation, since the magnetic field causes no physical damage to living cells and the growth rate of living cells

4
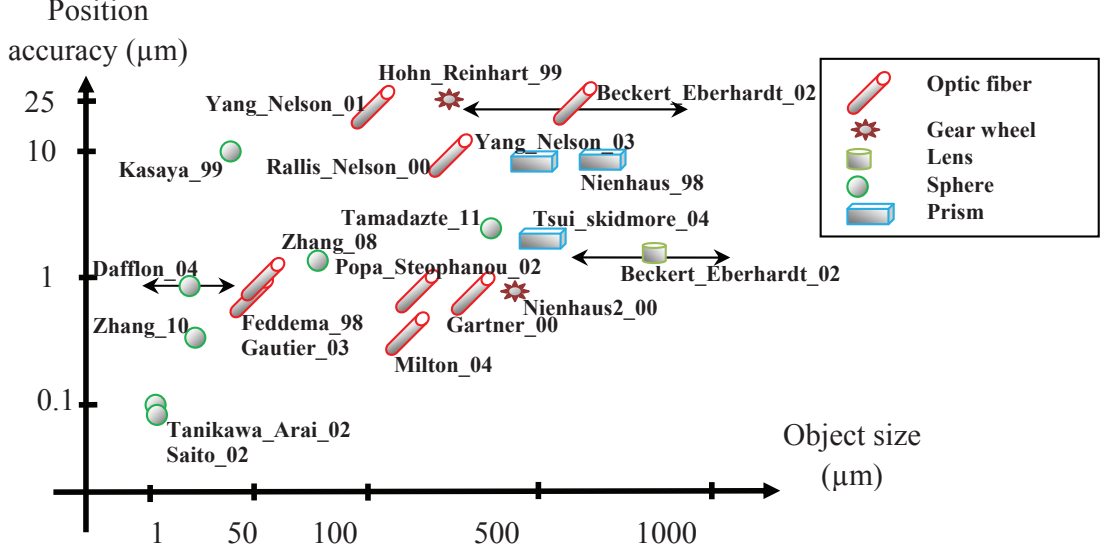
Figure 1.2: Manipulated objects and the precision of contact-based manipulations [18; 114; 127; 128]

is also not affected [108; 109].

## Contact Methods

The most common and reliable method of micro-manipulation involves using contact-based techniques. The literature validates several unindustrialized microrobotic systems for contact-based micro-manipulation applications as well for mass production and small series productions. Figure 1.2 summarizes the accuracy-versus-object-size for various contact-based micro-manipulation platforms. Performing dexterous tasks with a higher order of flexibility is a significant target of micro-manipulation platforms, but most research explores fundamental subsystems such as locomotion mechanism, end-effectors, and sensors [18]. The locomotion mechanism permits end-effector motions to be produced for micro-object manipulation. Based on the applications and constraints of the workspace, many locomotion mechanisms have been proposed, such as:

1. High precision macro-domain robots [62; 90; 114; 127; 128]
2. Micro-domain robots [59]
3. Mobile microrobots [38; 96]

a. Carl Zeiss micromanipulation platform- SteREO Discovery V20 [12]

b. Automatic microassembly station for MEMS integrations [120]
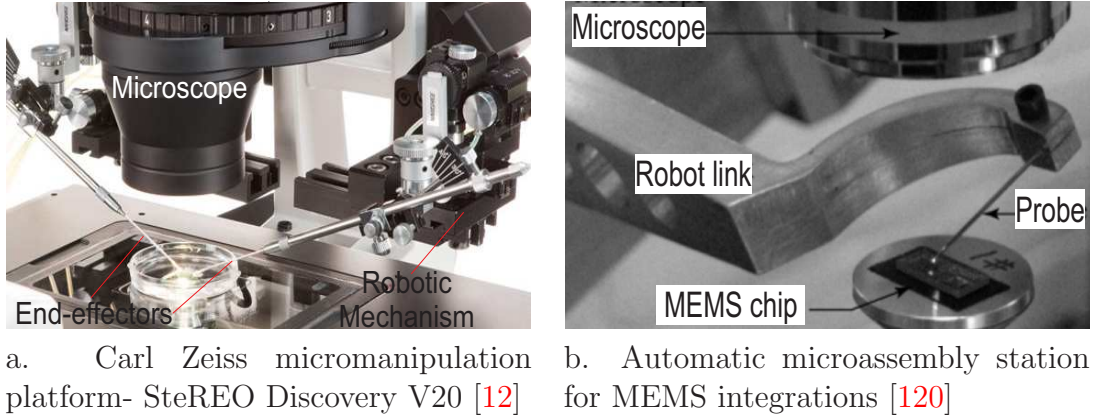
Figure 1.3: Macro-domain robots for micromanipulation and microassembly

A large body of literature addresses the micro-domain pick-and-place by employing a MEMS end-effector attached to a high precision macro-domain robot. Perhaps the most serious drawback of these bulky macro-domain robots as locomotion mechanisms is that the arms and connections of macro-domain robots constrain the working envelope of end-effectors, Fig. 1.3 shows some examples of macro-domain robots that have been used in micro-manipulation stations [The Carl Zeiss Corp. [12] constructed SteREO Discovery V20 for manipulation of living cells and genetic material by using a macro-domain robotic platform with micro-sized end-effectors. In a similar way, a research-made micro-assembly station [120] is constructed for MEMS integration by using a macro-domain robot.]. Furthermore, although macro-domain robots provide micro- and nano-ordered position accuracy, they are not designed to apply micro-domain forces and may even destroy manipulated objects by applying high order force/torque.

Numerous research has proposed the miniaturization of macro-domain robots for performing micro-domain tasks. These micro-domain robots are generally composed of elementary micro-domain units such as piezoelectric/ultrasonic actuator and DC miniaturized step motors [23]. Electric motors promptly lose their efficiency once downsized, as the torque required to turn an object around increases exponentially according to size [42; 97] ( whereas the force produced by an electromagnet cuts down at the cube of its length [42; 97]).Although some provide sub-micron resolution, limitations such as slow response time and high

nonlinearity in dynamics cause control issues with this kind of locomotion mechanism [125].Piezoelectric-based actuation mechanisms show promise for micro- and nano-scale robotic systems, but their small working range and high voltage requirements make them unfeasible for the current scale of connectors, power supply, and controllers [11].

Mobile microrobots offer the desired capability, versatility, and flexibility in micromanipulation and micro-assembly fields. These microrobots use numerous locomotion techniques such as swimming [46; 68; 68; 129], paddling [57; 81; 103], walking [1], and flying [8]. Figure 1.4 illustrates some mobile-microrobotic stations. Although the literature reports consequential advances in the design and implementation of this type of microrobotic system, integrating the on-board miniaturized power supply (which significantly increases the size of microrobots) remains a considerable challenge. However, untethered microrobotic systems show excellent potential in accommodating power supply constraints. These systems use off-board power sources through various methods such as electrostatic, photo-thermal, and magnetic transformation and carry out the required power transfers to mobile microrobots without direct hardware connections. Moreover, the magnetic actuation provides a cell-friendly environment for bio-micromanipulations. In [34], a magnetic untethered microrobotic system (MUMS) has been developed for micro-manipulation applications. This platform shows promise for extensive biological/biomedical applications, as the power required for the manipulation of a micro-gripper, shown in Fig. 1.4 (c) , is produced by an external magnetic drive unit.

Table 1.1 compares and summarizes the advantages and drawbacks of various locomotion strategies for contact-based micro-manipulation stations. As we can see, the micro-mobile robot provides superior locomotion mechanism such that their major drawbacks and on-board power supply and connection can be covered up by using untethered techniques.

## Micro-sized end-effectors and sensors

The end-effectors of micro-manipulation platforms have also been investigated and proposed for various applications. The most widespread of these mechanisms

a. Smart flexible microrobots for scanning electron microscope (Miniman III (left) and Miniman IV (right)) [96]
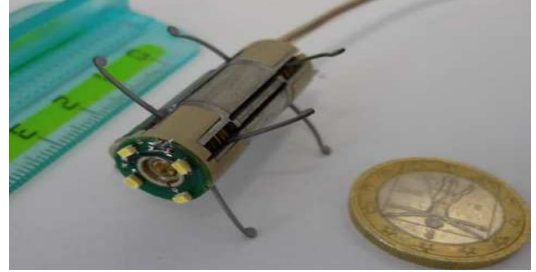
b. Endoscopic capsule prototype equipped with 8 mini-legs and 4 white LEDs (Vector)[1]
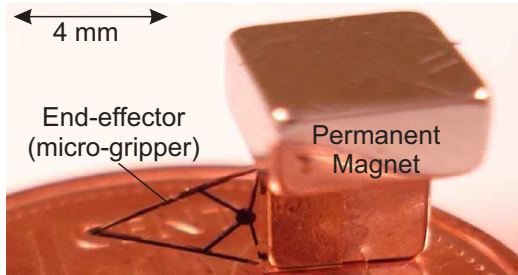
c. Magnetic levitated microrobot[32]
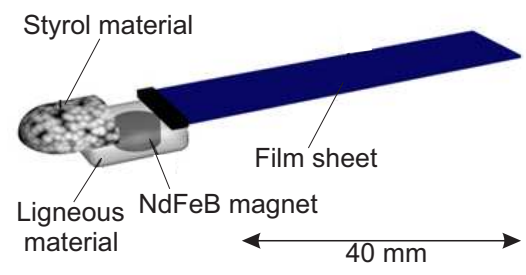
d. Fish-like microrobot [46]

Figure 1.4: Mobile microrobots for micro-manipulation and micro-assembly

are MEMS-based grippers, vacuum grippers, and needles. MEMS-based grippers have been proposed based on piezoelectric elements, shape memory alloys, fluidic actuated systems, and electrostatic actuators. The main advantage of MEMS-based grippers is that they enable the control of the grasp-and-release position with limited rotation of micro-objects. Vacuum grippers are generally flexible and simple mechanism tools for micro-manipulation of any shape micro-objects. The promising usefulness of these kinds of grippers is that they guarantee the deposition in spite of a large adhesion effect in a micro-domain environment [75].

Needles are also simple devices for pushing and pulling micro-objects, but their use is limited in pick-and-place tasks. To pick up a micro-object with needles, an adhesion force acting between the tool and the micro-object must be larger than forces between the micro-object and environment. On the other hand, the reverse action has to be performed to guarantee the deposition. The literature reports numerous investigations toward resolving these conflicting requirements,

Table 1.1: Comparison of various locomotion mechanisms

| Locomotion | Pros | Cons |
|---|---|---|
| Macro-domain Robot | ●High precision<br>●Commercialized | ●Damage to micro-objects<br>●Arms and connections constraints |
| Micro-domain Robot | ●Sub-micron resolutions | ●Slow time response<br>●High nonlinearity in dynamics<br>●High voltage required |
| Micro-mobile Robot | ●Sub-micron resolutions<br>●High flexibility | ●On-board power supply constraints<br>●Connection constraints |
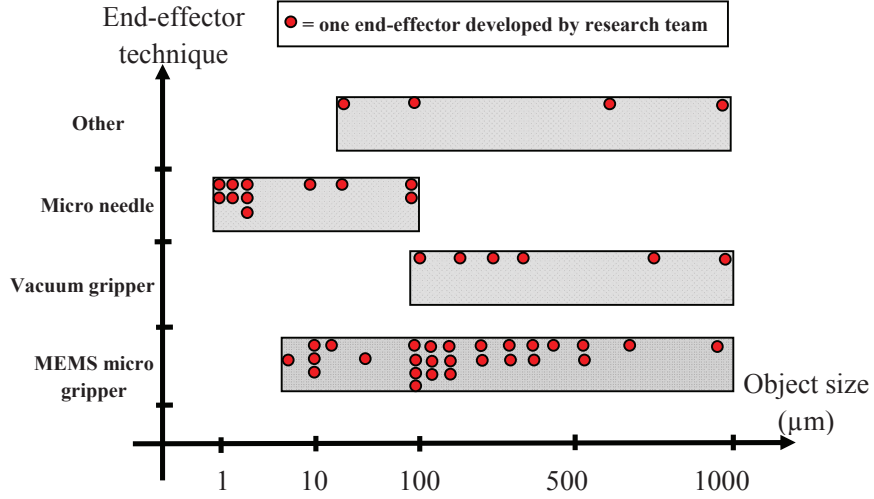


Figure 1.5: End-effector mechanism Vs. size of manipulated objects, each point presents one developed end-effector technique [15; 17; 18; 127]

such as: 1) using two tools [61], 2) using rotation techniques [52], and 3)using a specific tool trajectory [92]. The specific application has led to the development of a particular end-effector. To select one strategy for end-effector development, the size of the manipulated objects, the physical properties of the manipulation environment, and the geometry of the micro-objects all need to be considered, Fig. 1.5 references various developed end-effector techniques contrasted to the size of manipulated objects, from 1 $\mu$m to 1 mm.

Sensors are essential components of micro-manipulation platforms. These highly sensitive components provide feedback from physical properties of a micro-domain environment, which is significantly complex and poorly understood. To

perform micro-manipulation tasks, the precise measurement of force and position is a great challenge in providing accurate feedback to the control system, particularly in teleoperated and automatic mode. In particular, force sensing can be used to prevent damaging fragile micro-parts and to identify the characterization of micro-domain forces. Strain gages [52; 58], capacitance sensors [123], and PVDF (piezoelectric polymer) [41; 70; 100]have been investigated as force sensors, with resolutions ranging from 1 $n$N to 400 $\mu$N. For position feedback, numerous techniques have been proposed, such as optical microscopes, high resolution laser sensors, and scanning electron microscopes. An appropriate technique can be chosen based on the size of micro-parts and the required accuracy.

**Concluding remarks**

This dissertation will focus on developing a precise untethered magnetic-based locomotion mechanism for contact-based microrobotic platforms. A controlled magnetic field is used for non-contact manipulation of a microrobot that carries the end-effector. Advancing the end-effector technique and micro-sensors are not the key aspect of this research; instead, a simple end-effector will be used for experimental verification. Nonetheless, the proposed locomotion mechanism has the potential to be equipped with sophisticated end-effectors. A novel micro-domain force sensing method will also be introduced that does not require attaching force sensors to the end-effector.

## 1.1.2 Review of Magnetic Propulsion Mechanisms

Magnetic-based actuation mechanisms show great potential for non-contact energy transmission, (the untethered method) in microrobotic systems. These systems generally consist of a magnetic drive unit (the manipulator) which generates a magnetic field to provide the actuation energy for a ferromagnetic object (the manipulated object or an end-effector). Such a system is described in [40], in which a giant magnetostrictive alloy (GMA) is designed to provide actuation energy for an in-pipe micro mobile robot. The primary benefit of this mechanism is that the operating life time of the microrobot would last as long as power is provided to the drive unit. Thus, it will always be possible to generate enough force

to overcome surface forces for micro-domain applications, with no need to increase the on-board power supply size. The non-contact nature of a magnetic actuation mechanism makes it suitable for use in out-of-reach and hard-to-reach locations, such as hazardous environments and inside the human body [13; 14; 94; 102; 124]. In [71; 115], a clinical MRI platform is proposed for the navigation of a ferromagnetic bead inside the human body. This system has been validated *in vivo* in the artery of a living animal [71]. In [13; 14; 94; 102; 124], various endoscopic capsules have also been developed by using magnetic maneuvering concepts with robotic navigation systems. Eliminating the need for moving parts during the energy transfer not only reduces the maintenance and servicing expenses but also provides a dust-free environment for clean operation applications such as semiconductor manufacturing [130] and biological manipulations.

A considerable amount of literature has been published on magnetic actuation mechanisms that contain a small magnetic gap between the manipulator and manipulated objects [60; 130]. In a general small gap system, a magnetically floated stage is moved without problems caused by contact friction, and extra-high resolution position control can be achieved. These systems can typically produce a large horizontal working envelope, but the vertical working range is generally small. Therefore, the manipulated object cannot be sufficiently separated from the manipulator for remote applications, like in the workspace of a floating plate in [130] is $2\times2\times2$ $mm^3$. In [60],a multi-axis maglev stage with a horizontal operating range of $5\times5$ $mm^2$ and vertical operating range of $500$ $\mu m$ is presented. A contact-free planner system in [51] provides a horizontal workspace of $32\times32$ $mm^2$ and a vertical range of 1.5 $\mu m$.

Difficulties arise, however, when an attempt involves the large magnetic gap needed for telemanipulation applications [15; 21; 34; 55; 78; 115].To achieve a desired magnetic field in large magnetic gap systems, a proper magnetic circuit has to be designed. In [76], the concept of the pole-piece is introduced to augment the magnetic field for large gap systems. This concept has been investigated extensively in [55].Achieving motion control of manipulated objects in large gap systems means that the system has sufficient potential to operate in a remote or an enclosed environment.

A large and growing body of literature on large gap systems has investigated

one-DOF motions with a one-axis manipulator. Perhaps the most serious disadvantage of these approaches is that a three-axis manipulator is required to achieve the 3-D manipulation. Due to the limited space, the three-axis manipulator interferes with access to the manipulated object. In [76], a novel prototype mechanism is introduced for the 3-D motion of a small permanent magnet (PM) with a one-axis manipulator. In this system, the regulation of magnetic field for 3-D motion is intensely related to the geometric design of the pole-piece [55]. The combination of the electromagnets and the pole-piece configures the flux leakages in such a way as to produce 3-D actuation energy in the device workspace. In this system, a permanent magnet with a mass of 1 g is manipulated within a volume of $28\times28\times30$ $mm^3$. This large gap system is developed in [54] to manipulate a microrobot with a mass of 8.1 g in a volume of $29\times29\times26$ $mm^3$. The microrobot consists of a magnetic head, electronic circuits and fingers. A shape memory alloy (SMA) actuator activates the fingers to grasp or release the micro-objects. Based on the design in [54], a large gap system was developed at the University of Waterloo [21]. This system has the potential to manipulate a 11.19 $g$ microrobot in working envelope of $30\times22\times20$ $mm^3$.

In this study, a large gap system based on *Craig*'s research [21] has been developed with the purpose of improving the 3-D motion control for a magnetic untethered microrobotic system (MUMS).

## 1.1.3    Review of Teleoperation

One of the most important challenges in the design of micro-manipulation systems is the scaling effect phenomenon that changes the dominance of physical phenomena in micro-domain [95]. The insignificant unmodeled forces in the macro-world such as friction and adhesion act as dominant sources of force in the micro-world. Therefore, the better these forces are modeled in the design process of micro-robotic systems, the more reliable are the micro-object interactions are achieved. However, these complicated forces have been weakly observed, so human intervention can significantly enhance the micro-manipulation tasks with avoiding of imperceptible failures. In addition, a tactile or haptic feedback to the human operator shows a great promise for improving the dexterity and accuracy of task

suck as a robot-assisted minimally invasive surgery.

In such a system [3], the "Haptic Loupe" was developed to perform micro-manipulations by a human operator without stress and tension. Similar haptic micro-manipulation systems were proposed for micro-manufacturing and micro-assembly [36; 56; 118]. Moreover, haptic microrobotic systems show a significant promise in biological/biomedical applications that professional human operators perform dexterous micromanipulations, such systems as *da vinci* telerobotic surgical system in conjunction with tension measuring device [7], haptic-enabled tumor localization system [113], cell injection platforms [6; 101; 126], and cell/scaffold force-feedback manipulator [127]. Therefore, to advance our research-made prototype for bio-micromanipulation and medical applications, a "Haptic Loupe" is integrated with our magnetic untethered microrobotic system.

Moreover, using haptic interface coupled with a robotic platform in the biological and biomedical intervention can offer advantages including high resolution manipulation capability, good repeatability, high reliability, and fatigue reduction. Most of the interventions are either accurate procedure (cell manipulation, micro-surgery, and *etc*) or a minimal access to task environment (hazardous manipulation environment, inter vascular surgery, and *etc*). In teleoperated tools, the operational motion of a manipulator (slave robotic platform) is controlled by a human operator's interface (master platform). This master-slave robotic system enables human operators to handle complications in terms of dexterity, fine manipulation, and force-feedback capability.

The strategy of adjusting the master and slave controllers in a bilateral technique has been applied in some research on teleoperations. Salcudean *et al.* [93] presents "matched impedance" method, which uses the contact forces and velocities to adjust the master and slave target impedances to match high or low impedance environments. The variable damping impedance control has been proposed in a similar concept [29]. Various teleoperation control architecture proposed in literature can be classified as [116]

- 2-channel architecture [Position-error-based (PEB)]: the master and slave controller does not use force measurements and merely tries to minimize the difference between master and salve position. Thus, the reflecting force is proportional to this difference.

- 2-channel architecture [direct-force-reflection (DFR)]: This method uses direct force measurements to transfer the interaction between the slave and the environment.

- 4-channel architecture: This method uses a combination of direct position and force measurement for implementing the bilateral teleoperation.

The DFR and 4-channel architecture control schemes for bilateral teleoperation assume that the contact information is measured by force/torque sensors directly. However, force/torque sensors are expensive, sensitive to temperature variations, and noise-prone. An alternative approach is PEB bilateral teleoperation. Lawrence [63] showed that, with linear time-invariant controllers, the PEB architecture provides poor transparency. To improve the transparency, the position controllers are needed to be re-adjusted when the dynamics at the slave site changes, such as hitting a hard object [77]. In our study, the gain-switching control scheme for PEB bilateral teleoperation proposed by Ni [77] is employed as a strategy of the scaled bilateral teleoperation system (SBTS).

This study introduces a novel micro-domain force estimation method for applications in the magnetic untethered microrobotic system (MUMS). Due to the size restriction, attaching force sensors to our microrobot is impractical. A combination of Hall-effect sensor is used in the structure of the MUMS to estimate a single-axis environmental force with no need of attaching force sensors to the MUMS's microrobot. Thus, the measured force can be fedback to human operator's hand for higher transparency by a 2-channel DFR or 4-channel architecture.

## 1.2 Problem statement and objectives

Previous sections review various microrobotics system and challenges for micro-domain manipulation. Based on the reviewed literature, various micro-manipulation techniques have been investigated and compared. This study finally introduces a novel magnetic-haptic micro-manipulation platform (MHMP) with promising potential for extensive biological and biomedical applications. The platform includes three basic subsystems: a magnetic untethered microrobotic system (MUMS),

**Problem Statement**

Requirements for locomotion mechanism ⟫⟫ Magnetic Untethered Microrobotic Sys.
- On-Board power supply
- Arms and contact constraints
- Bio-comptibility

Requirements for dexterity and accuracy ⟫⟫ Haptic Interface - Bilateral Teleoperation
- Unknown source of environmental force/torque
- Professional user experience and human intervention

Requirements for transparency ⟫⟫ Hall-effect-based Force Estimation
- Measuring environmental force
- Attaching force sensor to microrobot is impractical- Size restrictions

**Research Objective**

**Magnetic-Haptic Micromanipulation Platform (MHMP)**

Figure 1.6: Problem statement and research objectives in brief

a haptic device , and a scaled bilateral teleoperation system (SBTS). There-fore, many challenges in different research fields are addressed as demonstrated schematically in Fig. 1.6.

As explained in Section 1.1, the magnetic untethered microrobotic technol-ogy presents a great deal of promise for bio-compatible micromanipulations. This technology transfers the actuation energy to the end-effector with no need of con-nections and moving parts, as well as creating a dust-free working environment. Thus, the inconvenience and restriction of arms and wires of macro-domain robots can be completely eliminated by magnetic-based actuation mechanism. More-over, the magnetic-based actuation mechanism can be employed for operation in hazardous and hard-to-reach working environments.

The next big challenge in magnetic-based micro-manipulation is accomplish-ing a dexterous task in a roughly known environment. A human-assisted interface with professional user intervention can accommodate some large uncertainties of working environments. In the developed haptic interface, the human opera-tor performs from and receives the force feedback via a haptic device while the magnetic untethered microrobotic system mimics the operator's hand motion on

the working space. There is possibility to reflect environment interaction forces to the operator's hand based on the difference between the operator's position command and the real position of the end-effector and without measuring the environment contact force, Position-error-based (PEB) technique. However, the transparency and reliability of the haptic interface can be advanced by feeding the environmental forces to the scaled bilateral teleoperation system (SBTS). Our micro-manipulation platform is equipped with a novel force measurement method to feedback the environmental forces to the operator's hand through the SBTS. A key aspect of this research concerns the integration of magnetic levitation technology and bilateral macro-micro control system challenges that leads to design and construct a "Magnetic-Haptic Micro-manipulation Platform (MHMP)". This platform is not only addressed the mentioned problems in Fig. 1.6, but also advanced exclusive aspect as dust-free working space and functioning in enclosed environments.

## 1.3 Thesis outline

This thesis will focus on design and implementation a novel haptic magnetic levitation device. This platform allows a human operator to control the macro slave robot through manipulating the macro master haptic robot. This thesis is structured around published or accepted manuscripts.

- **Chapter 1** has already introduced the research objectives of this dissertation. Furthermore, a comprehensive literature review on the recent research conducted on the micro-manipulation platforms has been carried out.

- **Chapter 2** describes the principle of magnetic levitation and demonstrates the overall structure of a haptic equipped micro-manipulation platform. By the end of this chapter, the background of the thesis will be finished and the original study will be initiated by Chapter 3.

- **Chapter 3** formulates the produced magnetic forces for motion control purposes. In addition, the dynamical model and experimental motion control of the magnetic untethered microrobotic system (MUMS) will be discussed in this chapter.

- **Chapter 4** demonstrates the analytical modeling of eddy-current damping mechanism to achieve higher position accuracy. The experimental measurements validate the correctness of the modeling and the proposed mathematical relation.

- **Chapter 5** introduces two novel concepts for position determination and environmental micro-domain force sensing. Using the magnetic flux measurement, the microrobot's position can be determined in non-transparent environment that the optical devices cannot be used. Furthermore, the value of magnetic flux can be used to estimate the environmental micro-domain force applied to the microrobot with no need of attaching force sensors to the microrobot.

- **Chapter 6** demonstrates the bilateral teleoperation control system design which is integrated with the MUMS. In addition, a human-assisted virtual reality platform is also presented that can be used for visualization and training purposes.

- **Chapter 7** presents the conclusions and recommendations of this dissertation. This research has resulted in the numerous journal and conference publications listed in Appendix C.

# Chapter 2

# Principle of Magnetic Levitation and Platform Description

This chapter first introduces the principle of magnetic levitation mechanism and the magnetic manipulation platform developed at the Maglev Microrobotic Laboratory, University of Waterloo. Then, to demonstrate the capability of the magnetic drive unit (MDU) to generate a controllable large gap magnetic field, details on the MDU (the backbone of the magnetic-untethered microrobotic system [MUMS]) are provided, along with optimal design parameter selection and numerical analyses. The intensive magneto-static design analysis of MDU plays a significant role in enhancing the performance of the MUMS, including its working envelope, motion stability, and motion accuracy. Magnetic circuit modeling is another analysis that demonstrates the importance of physical parameters such as geometry and material properties in an MDU'S design. In addition, the magneto-static numerical analysis, coupled with experimental verification in the design/analysis process, provides a good approximation of magnetic field mathematical modeling produced by the MDU. Finally, this chapter presents the basic components of the magnetic-haptic manipulation platform (MHMP), including two separate sites (a master site and a slave site) that can communicate with each other via analog and/or Ethernet connections. The Ethernet/UDP[1] communication enables the human operator to accomplish a task from a remote site

---

[1]User datagram protocol

connected to Internet.

This chapter is organized as follows. Section 2.1 presents the principle of magnetic force calculation for a magneto-static condition. Section 2.2 presents the concept of a stable 3D motion by controlling the magnetic field. Section 2.3 introduces the basic components of the developed MDU's structure. In Section 2.4, the 2D analyses of the MDU is explained including the magnetic reluctance model and numerical simulation. Section 2.5 describes the constructed platform for experimental measurement of magnetic flux produced by the MDU. Section 2.6 explains in detail the structure of the MUMS and the MHMP.

## 2.1   Magnetostatic Fields

It is crucial to have a basic understanding of magnetic field-related problems to initiate magnetic levitation-based manipulation. Maxwell's four field equations and three medium-dependent equations cover the entire theory of electromagnetics (EM). The classification of a magnetic problem is an important concept for selecting appropriate and simplified types of EM equations and is generally based on factors such as load, boundary conditions and solution region. According to these characteristics, the magnetic levitation is classified as a magneto-static type [99]. The magneto-static formulation is also an approximation even when the current is not static [99]. The equations satisfied by a stationary field are obtained by placing the time-varying terms in Maxwell's equation equal to zero as

$$\nabla \times \mathbf{H} = \mathbf{J} \tag{2.1}$$

$$\nabla \cdot \mathbf{B} = 0 \tag{2.2}$$

where $\mathbf{H}$ is the magnetic field intensity, $\mathbf{J}$ is the electric current density and $\mathbf{B}$ is the magnetic flux density. In terms of magnetic vector potential $\mathbf{A}$

$$\mathbf{B} = \nabla \times \mathbf{A} \tag{2.3}$$

19

applying Lagrange's formula of vector cross-product identity

$$\nabla \times (\nabla \times \mathbf{F}) = \nabla (\nabla \cdot \mathbf{F}) - \nabla^2 \mathbf{F} \tag{2.4}$$

to Eqs. 2.2 and 2.3 leads to Poisson's equation for magneto-static fields as

$$\nabla^2 \mathbf{A} = -\mu \mathbf{J} \tag{2.5}$$

where $\mu = \mathbf{B}/\mathbf{H}$ is the permeability of the medium. In the absence of a current, magnetic flux can be calculated by Laplace's equation. The magnetic field will be used in the calculation of the magnetic force experienced by a magnetic body in magnetic-based actuators. In most of these actuators, permanent magnets are used to increase the magnetic force in the magnetic field. The magnetic force experienced by a permanent magnet in a magnetic field can be calculated as "potential energy" and "magnetic dipole" methods. Using these methods, the calculation of the magnetic force experienced by a permanent magnet in an external magnetic field is presented in sections 2.1.1 and 2.1.2.

## 2.1.1   Potential Energy Method

Analyzing the energy in material bodies in a magnetic field is difficult when the bodies are permanently magnetized, since there is residual field due to inherent magnetization. The relation of the residual field can be expressed as [111],

$$\mathbf{B}_0 = \mu_0 (\mathbf{H}_0 + \mathbf{M}_0) \tag{2.6}$$

where $\mathbf{B}_0$, $\mathbf{H}_0$, and $\mathbf{M}_0$ are residual magnetic field, residual flux intensity and magnetization of a permanent magnet, respectively in the absence of an external magnetic field. There will be induced magnetization ($\mathbf{M}$) in the presence of external source that depends primarily on the resultant field ($\mathbf{H}$). The B-H relation can be presented as [111],

$$\mathbf{B} = \mu_0 (\mathbf{H} + \mathbf{M}_0 + \mathbf{M} (\mathbf{H} + \mathbf{M}_0)) \tag{2.7}$$

To obtain a simple derivation of the potential energy, common assumptions indicate that the inherent magnetization ($\mathbf{M}_0$) is rigid and the induced magnetization ($\mathbf{M}$) is negligible in comparison with $\mathbf{M}_0$. These assumptions are frequently used and fulfilled in practice. The permanent magnet can be modeled with the equivalent current distribution in a body of volume ($V$) bounded by a surface ($S$). The volume and surface current densities of an equivalent permanent magnet are

$$\mathbf{J} = \nabla \times \mathbf{M}_0 \tag{2.8}$$

$$\mathbf{K} = \mathbf{M}_0 \times \mathbf{n} \tag{2.9}$$

where $\mathbf{n}$ is the unit outward vector normal to $S$. The potential energy of a permanent magnet is defined as

$$U = -\int_V \mathbf{J} \cdot \mathbf{A} \mathrm{d}v - \int_S \mathbf{K} \cdot \mathbf{A} \mathrm{d}a \tag{2.10}$$

by substituting Eqs. 2.9 and 2.9 in Eq. 2.10,

$$U = \int_V (\nabla \times \mathbf{M}_0) \cdot \mathbf{A} \mathrm{d}v - \int_S (\mathbf{M}_0 \times \mathbf{n}) \cdot \mathbf{A} \mathrm{d}a \tag{2.11}$$

To simplify Eq. 2.11 the following relation are used [111]:

$$\mathbf{A} \cdot \nabla \times \mathbf{M}_0 = \nabla \cdot (\mathbf{M}_0 \times \mathbf{A}) + \mathbf{M} \cdot \nabla \times \mathbf{A} \tag{2.12}$$

$$(\mathbf{M}_0 \times \mathbf{A}) \cdot \mathbf{n} = (\mathbf{n} \times \mathbf{M}_0) \cdot \mathbf{A} = -(\mathbf{M}_0 \times \mathbf{n}) \cdot \mathbf{A} \tag{2.13}$$

By applying the divergence theorem and using vector potential relation, the total potential energy of a permanent magnet inside external magnetic field ($\mathbf{B}$) can be calculated as

$$U = -\int_V \mathbf{M}_0 \cdot \mathbf{B} \mathrm{d}v \tag{2.14}$$

This relation introduces the work necessary for a permanent magnet as a rigid body from infinity to a position with external magnetic field ($\mathbf{B}$). By using the virtual displacement method and the total potential energy relation, the exerted

force on the unit volume of a permanent magnet can be defined as

$$f = +\nabla\left(\mathbf{M}_0 \cdot \mathbf{B}\right) \tag{2.15}$$

In this study, we use a single dipole permanent magnet (it is assumed that $\mathbf{M}_0 = [0\ 0\ M_0]$); therefore, the induced magnetic force due to the external magnetic field can be represented by

$$f = +\nabla\left(M_0 \cdot B_z\right) \tag{2.16}$$

where $B_z$ is the z-component of the external magnetic field ($\mathbf{B}$). For a small permanent magnet, the magnetization $M_0$[1] can be taken practically as a constant and uniformly distributed throughout the volume. This approach simplifies the induced magnetic force on the permanent magnet as

$$\mathbf{F} = M\left(\nabla B_z\right)v \tag{2.17}$$

Considering the magnetic dipole moment as $P = M_0\ v$, the force components applied by the external magnetic field on the permanent magnet are

$$F_x = P\frac{\partial B_z}{\partial x} \tag{2.18}$$

$$F_y = P\frac{\partial B_z}{\partial y} \tag{2.19}$$

$$F_z = P\frac{\partial B_z}{\partial z} \tag{2.20}$$

As shown, the magnetic forces for 3D motions can be produced and controlled by the z-component gradients of the external magnetic field.

### 2.1.2  Magnetic Dipole Method

A small permanent magnet with a finite dimension can be represented by a single magnetic dipole moment by defining frequently used assumptions as: 1) the mag-

---

[1]the $M_0$ equals to $\left(\frac{B_s}{\mu_0}\right)$, where $B_s$ and $\mu_0$ and are the magnetic fields at the magnet surface, and the permeability of the vacuum, respectively.

netic dipole moment is assumed to be uniformly distributed in the permanent magnet; and 2) the magnet is assumed to be lumped in the center of the magnet. The magnetic dipole of the magnet can be represented by its equivalent electrical loop circuit $C$ with current $i$, area $S$, and normal vector $n$ as follows:

$$\mathbf{P} = iS\mathbf{n} \tag{2.21}$$

The induced magnetic force experienced by a magnetic dipole in the external magnetic field can be calculated by

$$\mathbf{F} = i \int (\mathrm{d}\mathbf{l} \times \mathbf{B}) \tag{2.22}$$

where $\mathbf{l}$ is a line element carrying the current $i$. The force $\mathbf{F}$ on the dipole (the loop $C$) is then calculated as follows:

$$F_x = i \oint_C (\mathrm{d}\mathbf{S} \times \mathbf{B})_x = iS \left( \frac{\partial B_z}{\partial x} \right) = P \left( \frac{\partial B_z}{\partial x} \right) \tag{2.23}$$

$$F_y = i \oint_C (\mathrm{d}\mathbf{S} \times \mathbf{B})_y = iS \left( \frac{\partial B_z}{\partial y} \right) = P \left( \frac{\partial B_z}{\partial y} \right) \tag{2.24}$$

$$F_z = i \oint_C (\mathrm{d}\mathbf{S} \times \mathbf{B})_z = -P \left[ \left( \frac{\partial B_x}{\partial x} \right) + \left( \frac{\partial B_y}{\partial y} \right) \right] \tag{2.25}$$

where $\mathbf{S}$ is the total vector area enclosed by the current. According to Maxwells equations, $\nabla \cdot \mathbf{B} = 0$, and so we can write $(\partial B_x / \partial x) + (\partial B_y / \partial y) = -(\partial B_z / \partial z)$ and magnetic force in z-direction becomes

$$F_z = P \left( \frac{\partial B_z}{\partial z} \right) \tag{2.26}$$

The permanent magnet experienced force inside an external magnetic field has been derived by two methods: "potential energy" and " magnetic dipole". Both methods present the same relations for the calculation of the magnetic force. The external magnetic field also applies magnetic toque $\tau = \mathbf{P} \times \mathbf{B}$ to the magnetic dipole. This magnetic torque makes the magnetic dipole parallel to the magnetic field. Therefore, changing the magnetic field in a single direction results in changing forces in three dimensions and changing the torque in one dimension.

## 2.2 Magnetic Levitation Principles and Operations

Previous sections [2.1.1 and 2.1.2] demonstrated that, to have a force in a certain direction on a single dipole permanent magnet, the magnetic flux density **B** should be non-uniform along that direction. This is because the non-uniform magnetic field causes a magnetic gradient that produces a magnetic force. Physically, within the external magnetic field, the permanent magnet tends to move toward the minimum total potential energy location. At this position, the maximum of the magnetic field, $B_{max}$, is acquired. This is an important criterion for the design of a magnetic drive unit (MDU) that produces an external magnetic field to apply forces and moment to a permanent magnet. Figure 2.1 shows the vertical magnetic field and the $B_{max}$ position generated by a single electromagnet. In steady state, the vertical force balances the gravitational force and the horizontal force equals zero, i.e., the magnet is steady at the location of $B_{max}$, since no external force exists in the horizontal direction. Thus, the position of the magnet can be controlled by regulating the gradient of B and the $B_{max}$ position. Figure 2.1 demonstrates that a single electromagnet is able to change the gradient of B but cannot change the $B_{max}$ position in the horizontal plane, and so the $B_{max}$ is fixed at the centerline of the electromagnets. Hence, a single electromagnet can control the vertical position of a permanent magnet by changing the coil's electromagnetic current.

*Khamesee* [54] has employed multiple electromagnets to control the motion of the $B_{max}$ in the horizontal plane. Multiple electromagnets produce multiple $B_{max}$ positions, making horizontal motion unpredictable. *Khamesee* [55] has proposed a specially designed pole-piece to connect the poles of electromagnets and achieve a unique $B_{max}$ in the horizontal plane. Figure 2.2 qualitatively demonstrates the pole-piece performance of an MDU with two identical electromagnets. As shown, the combination of the pole-piece and the electromagnets configures the vertical magnetic field in such a way that only one $B_{max}$ appears in the horizontal plane below the pole-piece. In a 2-D demonstration, the position of the $B_{max}$ can be controlled by tuning the coil's current of electromagnets.

As shown in Fig. 2.2(a), when the electromagnets are equally loaded, the
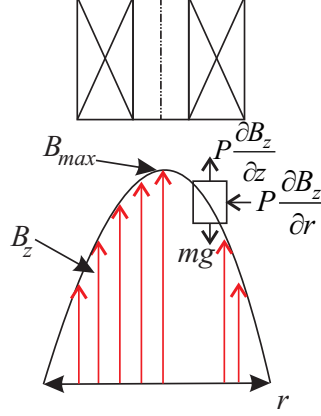
Figure 2.1: Generated $B_{max}$ position by a single electromagnet

distribution of the magnetic field in the vertical direction has multiple $B_{max}$ positions. In same the way, the pole-piece configures the magnetic field for unique $B_{max}$, as shown in Fig. 2.2(b), and the permanent magnet is levitated bellow the center of the pole-piece.

Electromagnets that are unequally loaded cause changes in $B_{max}$ positions, as shown in Figs 2.2(c) and (d). Much like equally loaded electromagnets, the pole-piece plays an important role in configuring the magnetic field into a focal point for a unique $B_{max}$ in horizontal motion. In fact, in the presence of the pole-piece for a 2D demonstration, increasing the current in one electromagnet shifts the $B_{max}$ toward that electromagnet. In the same way, the 3D motion of a levitated object can be achieved with a 3D arrangement of vertical electromagnets and a pole-piece.

*Khamesee* [55] investigated various geometric designs for pole-pieces in parallel with numerous arrangements of electromagnets, showing that each pole-piece has a specific operation working envelope. As well, he developed a combination of four vertical electromagnets and a disk pole-piece for the 3D motion control of a small permanent magnet, demonstrating that the summation of the electromagnet currents determines the vertical position, while the ratio of the currents placed across the center determines the horizontal location.

The following section introduces an MDU based on the design in [54]. The proposed MDU is constructed at the University of Waterloo with the intent

(a) Without Pole-piece, equally loaded  (b) With Pole-piece, equally loaded

(c) Without Pole-piece, unequally loaded  (d) With Pole-piece, unequally loaded
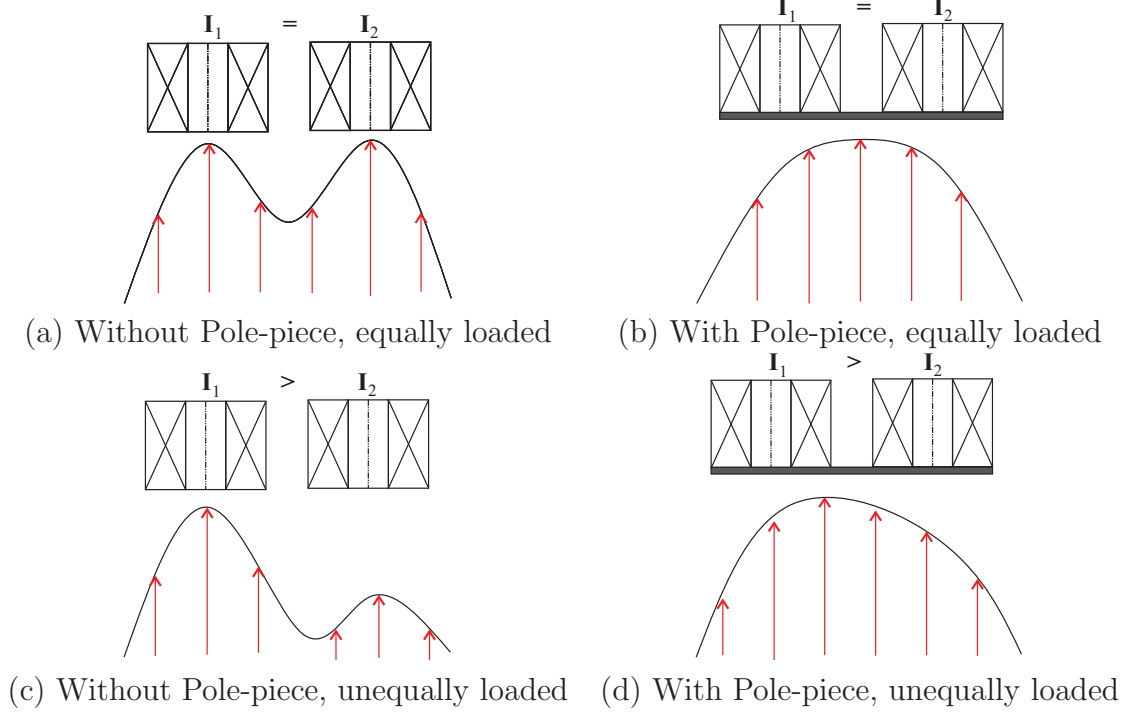
Figure 2.2: Demonstration of the qualitative performance of pole-piece

to develop a micromanipulation platform towards practical biomedical and microassembly applications.

## 2.3 Magnetic Drive Unit (MDU) Structure

The magnetic drive unit (MDU) is the heart of the MUMS in the sense that it produces the required magnetic field for the motion control of a microrobot. The MDU consists of three basic components: electromagnets (six pairs, the six-circular pattern of the electromagnets provides uniform magnetic gradient distribution in the horizontal working space, and also the pair configuration has smaller coil inductance that results in faster dynamical response of the MDU), a pole-piece, and a yoke, as shown in Fig. 2.3. The electromagnets provide the source for generating a magnetic field from an external source of electric energy. As described in section 2.2, a single electromagnet can be used for one-dimensional (vertical) magnetic levitation but cannot control the distribution of the magnetic

field on the horizontal plane. Thus, for 3D levitated movement of objects, an arrangement of multiple electromagnets is required. Figure 2.3 illustrates such an arrangement of electromagnets, the outer diameter,length, and turns of each electromagnets are 42 $mm$, 40 $mm$, and 840 turns respectively. The geometrical properties of the electromagnets were determined based on the MDU's required working envelope.



(a) Schematic view of the MDU    (b) Arrangement of electromagnets
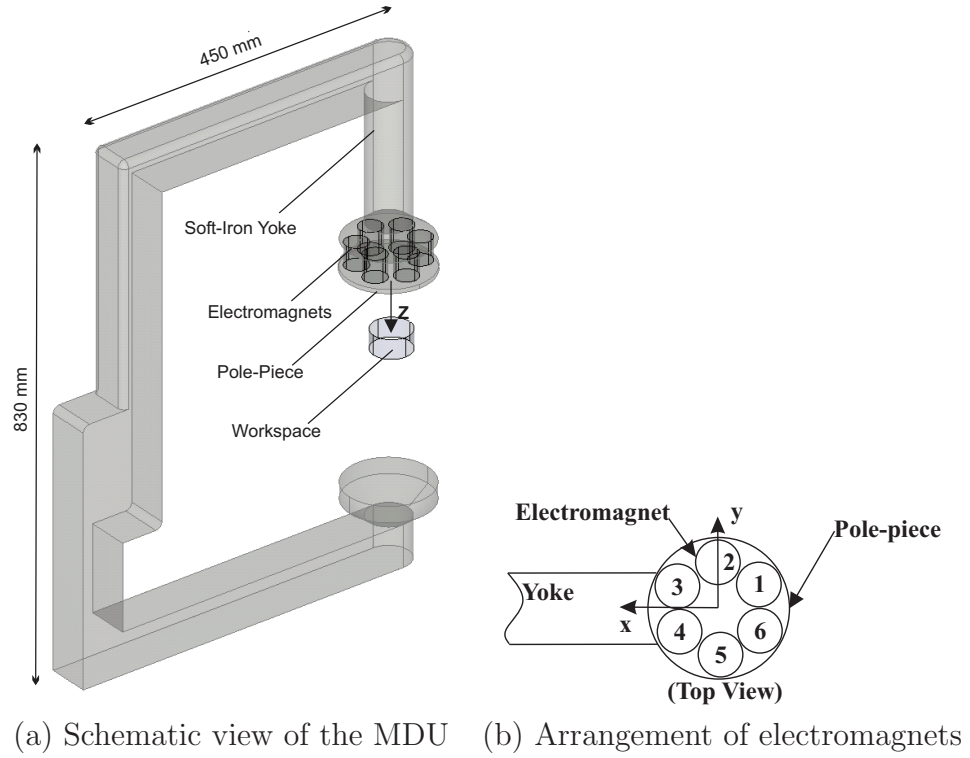
Figure 2.3: Basic components of the magnetic drive unit

A pole-piece can connect individual poles of electromagnets to eliminate the appearance of multiple poles and produce a focal point of maximum magnetic field in the horizontal plane. *Khamesee* [55] investigated the effects of various pole-piece profiles in controlling the $B_{max}$ through finite-element simulations, as well as experimental measurements and profiles such as flat plate, disk, cylinder, cross, cylinder-plate, and cylinder-cross. Based on *Khamesee*'s research, a disk pole-piece has been chosen in the present research to achieve an appropriate magnetic flux control.

A soft iron yoke is used to generate a closed loop magnetic circuit and increase
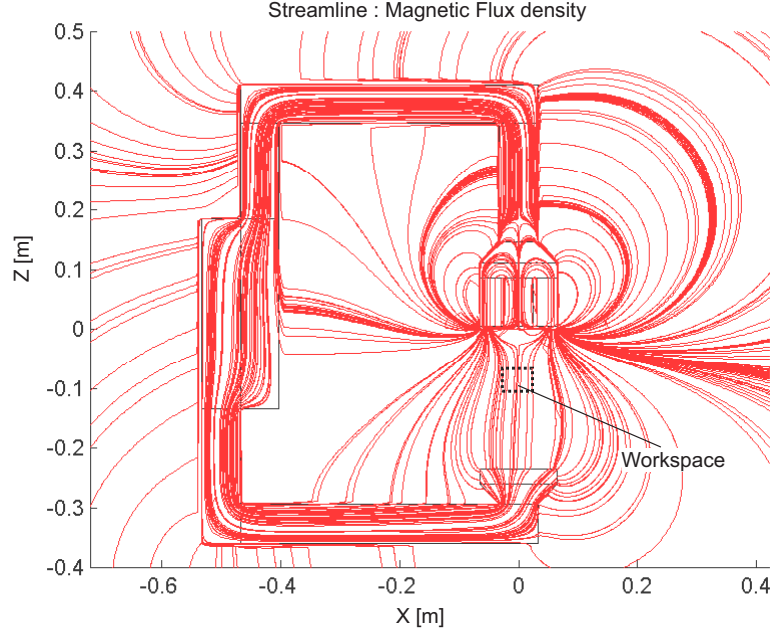
Figure 2.4: Magnetic flux streamlines in the MDU by COMSOL, two electromagnets are equally loaded

the magnetic field intensity in the working space. The yoke aligns the magnetic field in the vertical direction inside the workspace. Since the gravity force is in a vertical direction, the alignment of the magnetic field streamlines with the vertical direction, resulting in a higher magnetic force to levitate larger object with less energy consumption. *Shameli* [99] demonstrated that in situations where the currents fed to the electromagnets are unequal, the yoke increases the horizontal gradient of the magnetic field, which eventually increases the magnitude of the horizontal force of the levitated object.

Figure 2.3 demonstrates the finite element analysis (FEA) of the MDU by the COMSOL's magneto-static module. This figure shows that at distances too close to the pole-piece, the magnetic field is uneven and has multiple maximum points. Hence, in a small region of the MDU's large gap, the magnetic field's streamlines are parallel in the vertical direction ($x, y \in [15, 15]$ mm, reference axes are presented in Fig. 2.3) and also have a unique $B_{max}$ in the horizontal plane. In the vertical direction, the magnetic gradient is drastically reduced by increasing the vertical distance from the pole-piece. Since the current in each electromagnet
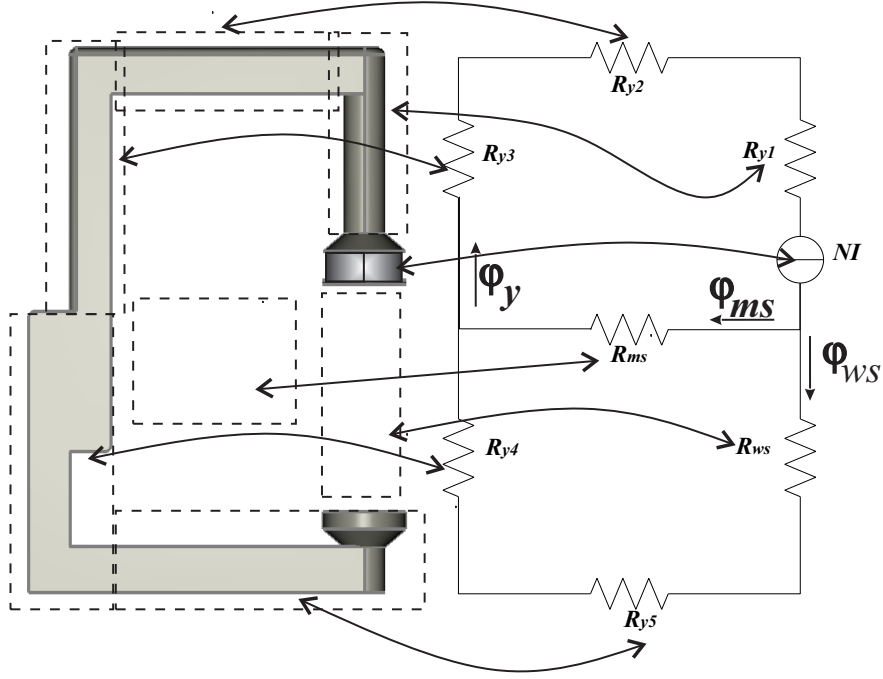
Figure 2.5: The equivalent magnetic reluctance demonstration of the MDU

can be varied between 0 to 3A, the weight of the microrobot determines the working envelope in the vertical direction. In the following section, the physical parameters of the MDU will be investigated by the magnetic reluctance concept.

## 2.4   Magnetic Reluctance Model of The MDU

A basic approach in the estimation of an MDU's performance can be carried out by the application of the magnetic reluctance model (MRM) [49]. This concept is used in the analysis of magnetic circuits and is analogous to a resistance model in electrical circuit analyses. However, rather than dissipating magnetic energy, it stores it. Similar to the way an electric field causes an electric current to follow the path of least resistance, a magnetic field causes a magnetic flux to follow the path of the least magnetic reluctance.

An MRM can give a good estimation of the magnetic flux produced inside the air-gap (workspace), pole-piece and yoke. This approximation provides useful information about the magnetic saturation of an MDU's parts and also enables
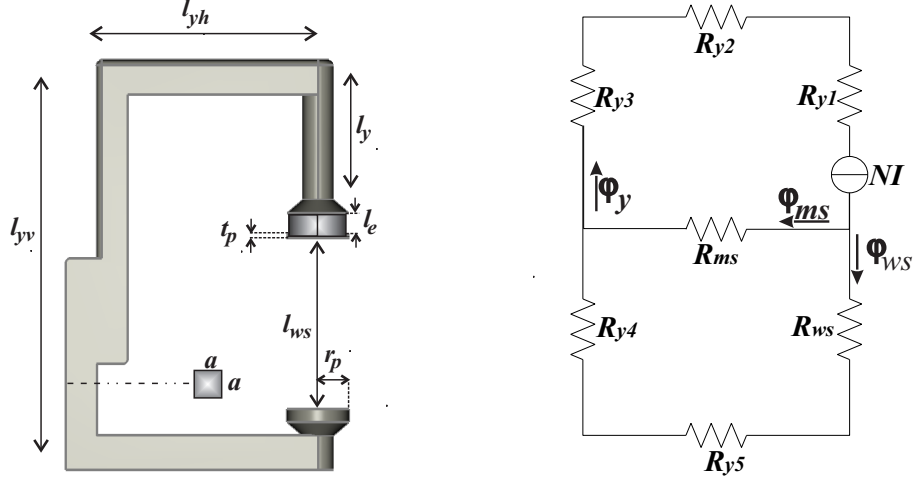
Figure 2.6: Magnetic reluctant model of the MDU

us to approximate the magnetic short-circuit of the MDU. A magnetic short-circuit occurs when the magnetic streamline does not go through the working envelope, a phenomenon which decrease the operational magnetic field in the working envelope and thus increases power consumption.

Figures 2.6 and 2.5 demonstrate the MRM of the MDU. As shown, $R_{ws}$ and $R_{ms}$ represent the magnetic reluctance of the air-gap between the two yokes' ends and the magnetic reluctance of the air-gap between the pole-piece and the yoke's internal surface, respectively. The yoke's magnetic reluctance has five parts ($R_{y1}$, $R_{y2}$, $R_{y3}$, $R_{y4}$), as shown in Figs. 2.6 and 2.5. In these two figures, $N$ is the total number of electromagnets with a coil current of I. The magnetic flux leakages inside the workspace and the yoke are demonstrated by $\phi_{ws}$ and $\phi_y$, respectively, with the $\phi_{ms}$ showing an approximation of the magnetic flux short-circuit. Thus, the optimal design for an MDU results in a high ratio of $\phi_{ws}/\phi_{ms}$. The values of magnetic reluctances are approximated as [49],

$$R_{ws} = \frac{l_{yh}}{\mu_0 \, A_y} \tag{2.27}$$

$$R_{ms} = \frac{l_{ws}}{\mu_0 \, A_{ws}} \tag{2.28}$$

$$R_{y1} = R_{y3} = \frac{l_{yh}}{\mu_0 \, \mu_r \, a^2} \tag{2.29}$$

$$R_{y2} = R_{y5} = \frac{l_y}{\mu_0 \, \mu_r \, a^2} \tag{2.30}$$

$$R_{y4} = \frac{l_{yv} - l_y}{\mu_0 \, \mu_r \, a^2} \tag{2.31}$$

where $\mu_0$ and $\mu_r$ refer to the permeability of the air and relative permeability of the yoke's structure, respectively (the yoke is made out of soft iron with $\mu_r$ equals to 4000). $A_y$ and $A_{ws}$ represent the flux penetration surfaces that can be approximated as

$$A_y = (l_e + t_p) \, a \tag{2.32}$$

$$A_{ws} = \pi r_p^2 \tag{2.33}$$

Using the circuit analysis, the magnetic flux in yoke is calculated as,

$$\phi_y = \frac{NI \, (R_{ms} + R_{ws} + R_{y5} + R_{y4})}{(R_{y1} + R_{y2} + R_{y3}) \, (R_{ms} + R_{ws} + R_{y5} + R_{y4}) + R_{ms} \, (R_{ws} + R_{y5} + R_{y4})} \tag{2.34}$$

To investigated the magnetic saturation of the yoke the following numerical values are used: $a = 0.0635$ m, $N$=12×840, and $I$=3.5 A. The $B_{y_{max}}$ is estimated as

$$B_{y_{max}} = \frac{\phi_y}{a \times a} = \frac{0.0035}{0.0635 \times 0.0635} = 0.86 \, (T) \tag{2.35}$$

Since the soft iron reaches magnetic saturation at approximately 2.2 T, the geometry of the yoke ensures that under no condition will magnetic saturation be experienced. The ratio of $\phi_{ws}/\phi_{ws}$ is obtained as

$$\frac{\phi_{ws}}{\phi_{ms}} = \frac{R_{ms}}{R_{ws} + R_{y5} + R_{y4}} = 6.2 \tag{2.36}$$

31

Therefore, the undesired flux leakage to the internal yoke parts magnetic short-circuit will measure approximately 15% of the magnetic flux produced by the yoke's electromagnets. Figure 2.7 shows these undesired flux leakage streamlines produced when all electromagnets are equally loaded. The electromagnets closer to the inner part of the yoke produce more undesired flux leakages, since the produced magnetic flux by these electromagnets experience lower $R_{ms}$. This phenomenon shifts the $B_{max}$ position away from the inner part of the yoke, a shift that is especially significant in the yoke structure xz-plane. Figure 2.8 presents a numerical simulation by COMSOL that verifies this phenomenon, demonstrating a $B_{max}$ shift across the vertical distance from the center of the pole-piece when all of the electromagnets are equally loaded. Increasing the distance from the pole-piece causes additional $B_{max}$ shifts in the horizontal plane. The experimental measurements also verify the $B_{max}$'s shifting away from the yoke structure. While a permanent magnet is levitated with equally loaded MDUS's electromagnets, the horizontal steady-state position of the permanent magnet changes with its vertical distance from the yoke. Because the portion of undesired flux leakage to the inner part of the yoke is varied by the distance from the pole-piece, a 3D position control strategy needs to be employed to achieve high accuracy magnetic manipulation.

## 2.5 Automated Magnetic Field Scanner (AMFS)

Magnetic force modeling is the first step in controlling the motion of a microrobot. As explained in section 2.1, magnetic force determination requires an accurate magnetic field model. Section 2.4 presents a numerical analysis of the MDU by COMSOL commercial software. Due to the geometrical complexity of the MDU, experimental measurements coupled with FEA results in a more accurate model of the produced magnetic field model. An automated magnetic field scanner (AMFS) has been developed to measure the magnetic flux inside the working envelope of an MDU. The AMFS consists of three components: an Epson robot, a gaussmeter, and a real-time controller. Figure 2.9 shows a schematic diagram of the AMFS and its data flow.

The current for each electromagnet and workspace region are passed to a real-
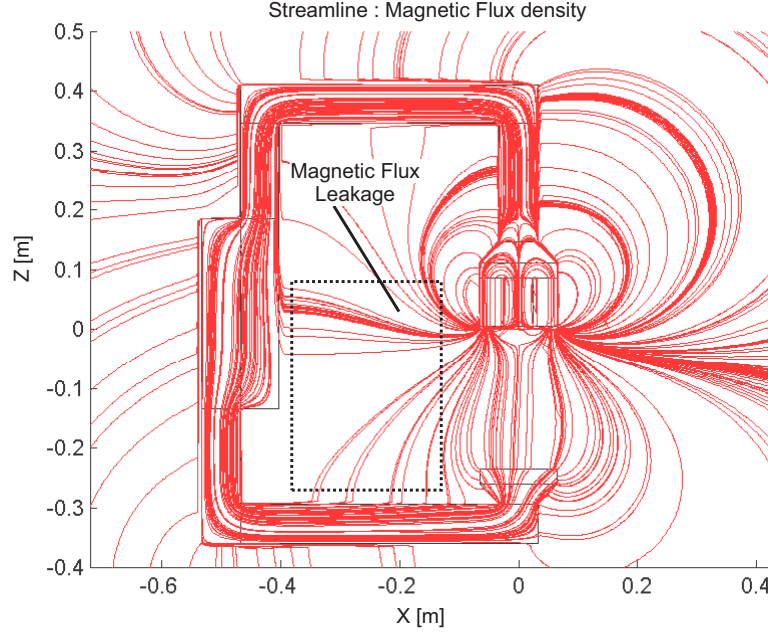
Figure 2.7: Undesired magnetic flux leakage

time computer, which then sends a current command to the MDU and position commands to the Epson robot. The magnetic field inside the air gap has been measured with a gaussmeter probe (Lakeshore 421). The probe is moved inside the workspace by the Epson robot while the z-component of the magnetic field is measured and sent to a real-time computer. The surface and contour plot in Fig. 2.10 illustrate the measured z-component of the magnetic field when the electromagnet number one is loaded with a 1A current. To demonstrate the uniqueness of the $B_{max}$ in the horizontal plane and controlling the position, Fig. 2.11 presents the measured z-component of the magnetic field in different current ratios for the electromagnets (numbers 2 and 5). By decreasing the current ratio of $I_2/I_5$, the $B_{max}$ shifts its position from the positive side of the y-axis to the negative side. Based on an experimental measurement, the next chapter explains the derived mathematical model of a magnetic field produced by an MDU
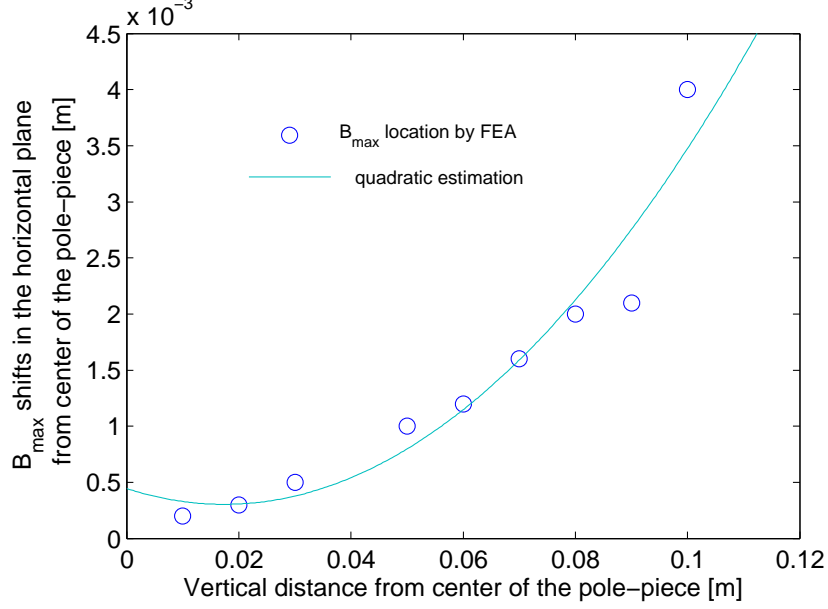
Figure 2.8: $B_{max}$ position shifts away from the yoke while all electromagnets are equally loaded

## 2.6 Magnetic Untethered Microrobotic System (MUMS)

The magnetic untethered microrobotic system (MUMS) is the heart of the the magnetic-haptic micromanipulation platform (MHMP) in the sense that it produces a non-contact motion actuation mechanism. The MUMS consists of three main components: the MDU, the real-time controller, and a microrobot. The schematic data flow and experimental setup are shown in Fig. 2.12. The MDU structure and its performance analyses have already been explained in previous sections.

A dSPACE real-time controller and "Control Desk", commercial software developed by dSPACE Inc., are used to develop the control system and a user interface, respectively. The "Control Desk" provides an intuitive graphical user interface to visualized the selected real-time parameters. The dSPACE real-time controller has a DS-1006 processor board that uses a quad-core AMD opteron
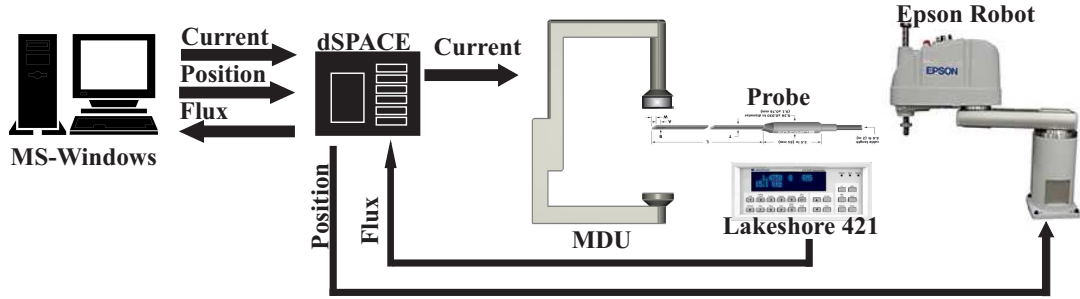
Figure 2.9: Schematic digram of developed automated magnetic field scanner (AMFSC)
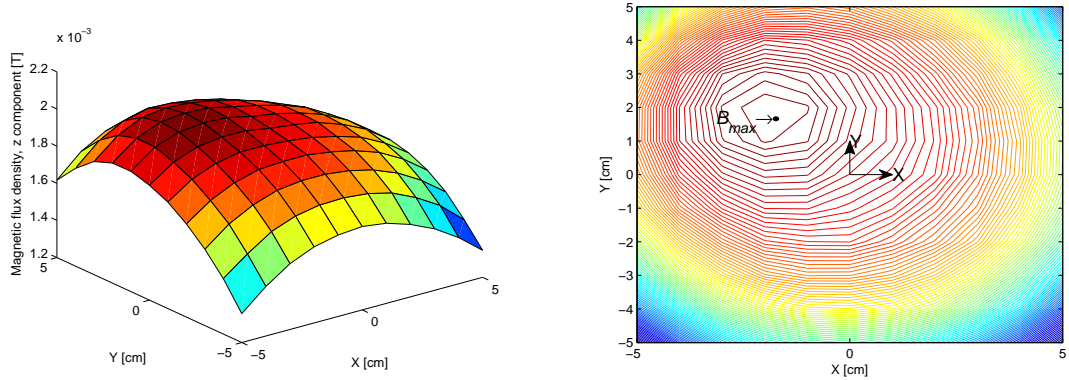


Figure 2.10: Surface and contour plot of magnetic flux density z-component obtained by experimental measurement,at z=75 mm and electromagnet number one current equals 1A

processor[1], which is a high computing power for processing-intensive real-time models. This board is fully programmable in Matlab/Simulink. The processor board is connected by a Bus cable to the DS-2004 A/D[2] board and DS-2103 D/A[3] board. Each of the DS2004's 16 channels has an independent A/D converter with a resolution of 16 bits and differential inputs ranging of $\pm 10$ volts and $\pm 5$ volts.

The DS-2103 board provides 32 channels with a resolution of 16 bits within

---

[1]x86-compatible 64-bit server multi-core processor. It provides 512 kB L2 cache per core and 6 MB shared L3 cache. The DS1006 also has 1 GB local memory for executing real-time models, 128 MB global memory per core for exchanging data with the host PC, and 2 MB on-board boot flash memory [28]

[2]Analog to digital

[3]Digital to analog

(a) current ratio $I_2/I_5 = 2$

(b) current ratio $I_2/I_5 = 1$

(c) current ratio $I_2/I_5 = 0.5$
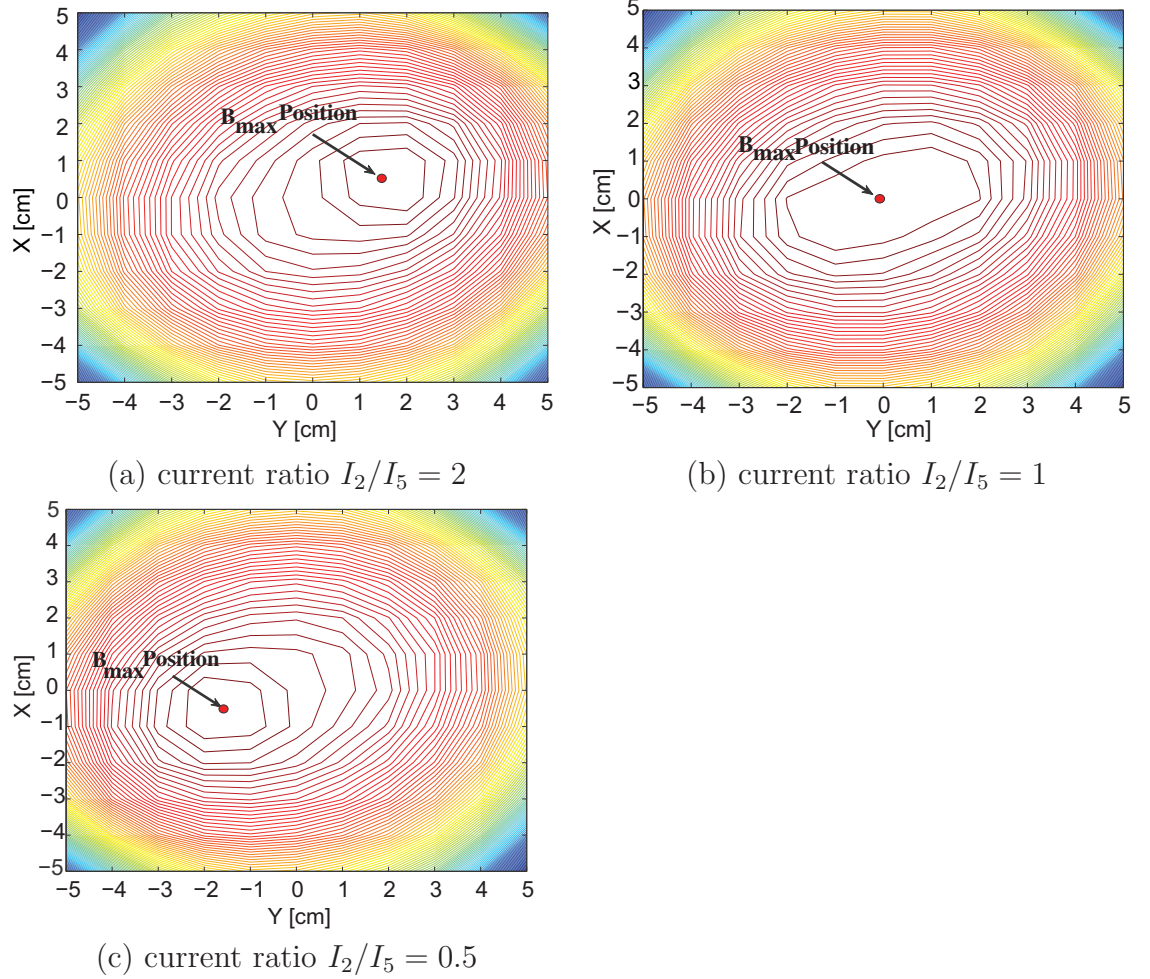
Figure 2.11: The measured magnetic field at 8 $cm$ below the pole-piece, $B_{max}$ position vs. current ratio

a range of $\pm 10$ volts and $\pm 5$ volts. All of the real-time parameters can be accessed or modified via a host computer that connects to the dSPACE real-time controller by an optical fiber and DS 814 link board. A custom-built amplifier with two Sorensen DCS40- 30E DC (more detailed information is provided at [99]) are combined with the dSPACE real-time controller to supply power for the electromagnets, based on the dSPACE real-time computation.

The MUMS's microrobot is basically comprised of a microgripper, electronic circuits, and a very small permanent magnet (PM). In experimental measurements, an uncomplicated microrobot, which consists of a permanent magnet and
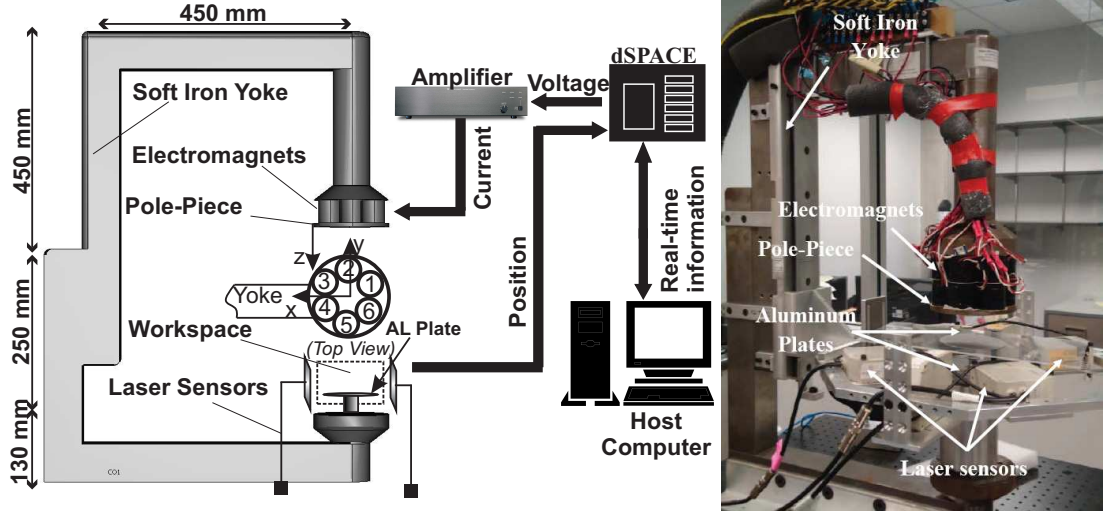
Figure 2.12: Schematic representation of the magnetic untethered microrobotic system (MUMS)

a needle-based end-effector, is used to verify the performance of the proposed platform, Fig. 2.13 presents the structure of the microrobot. However, a more sophisticated robot equipped with various micro-grippers can be used in real applications. The detailed design and development of the microrobot is not considered to be one of the key aspects of this research.
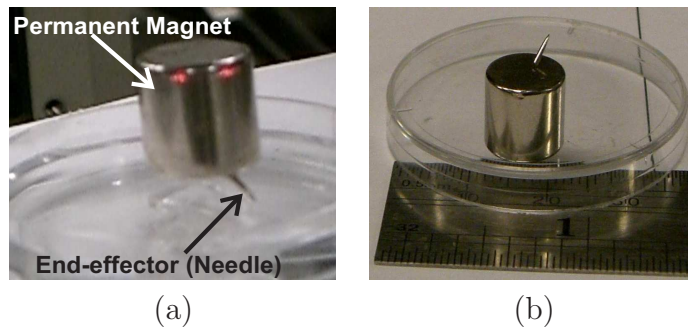


Figure 2.13: The MUMS's microrobot structure: (a) levitated inside the workspace , (b) placed beside a ruler

Three Keyence LS-5000 scanning laser sensors are employed to measure the 3-D positions of the microrobot. These sensors are mounted on a specific frame that surrounds the working envelope. Figure 2.14 shows the accuracy of each

laser sensor vs. the location of the object in the scanning range. The laser sensors typically provide accuracy of around 2-8 $\mu$m (the highest accuracy being at the center region of micrometer's working space, and the lowest at the boundaries [53]). Analog outputs from the laser sensors are used to feed the microrobot's position back to the dSPACE real-time controller. Since the microrobot's radius is pre-determined, the position measurement of the microrobot can be determined. The analog output range of the laser micrometer is $\pm 10$ volts, captured by the DS-2004 board that triggers a 0.6 $\mu$m capturing resolution.
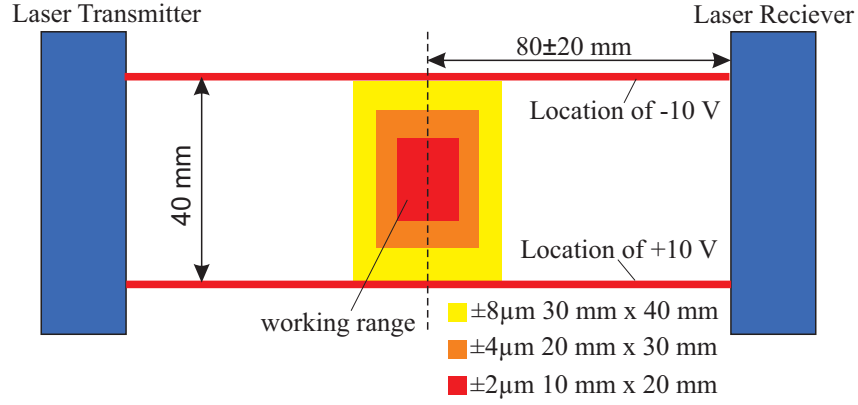


Figure 2.14: Accuracy mapping of the Keyence laser sensor [53]

## 2.7  Magnetic-Haptic Micromanipulation Platform (MHMP)

This section provides an in-depth introduction to the magnetic-haptic manipulation platform (MHMP), with Figure 2.15 presenting a schematic diagram. The platform includes a master site and a slave site that can communicate with each other via analog and/or Ethernet connections. The Ethernet/UDP[1] communication enables the human operator to accomplish a task from a remote site connected to the Internet. In the UDP communication demonstrated in Fig. 2.15.a, the master site communicates with a server computer in the slave site. This server computer updates the real-time parameters on the dSPACE real-time controller.

---

[1]User datagram protocol

In the analogue comunication presented in Fig. 2.15.b, the master site uses DAQ system to communicate directly with the dSPACE real-time controller.

The slave site consists of two basic systems: a magnetic untethered micro-robotic system (MUMS) and a scaled bilateral teleoperation system (SBTS). The MUMS provides motion control and interaction with the environment, while the SBTS implements macro-micro scaling for both position and force, making a micro-domain task more comfortable for the human operator.

The master site consists of two major systems: the haptic-PhanTom omni device (HPOD) and a server computer. The human operator can control the microrobot's position by moving the HPOD's stylus. In addition, the HPOD provides force-feedback on the human operator's hand. A Linux server computer is employed to communicate with the slave site. The server sends position commands from the master site to the slave site and also receives the calculated force-feedback from the slave site through analog and/or Ethernet/UDP. The C++ and Matlab source programs for communication are printed in Appendix A.

The haptic PhanTom Omni device (HPOD), which is often used in haptic and telerobotic research, is an inexpensive portable six degree of freedom positional sensing haptic device made by SensAble Technologies [98] (see Fig. 2.16). The nominal resolution for this device is 0.55 mm and can cover the motion range of hand movements pivoting at the wrist. The maximum exertable force at its nominal position is 3.3 N. Table2.1 represents the technical specification of the HPOD used in this research. The Phantom is connected to a Linux computer by a Firewire IEEE1394 port. To program the PhanTom Omni, C++ language programming was used; however, an HPOD analysis, including DH[1] parameter, forward kinematics, inverse kinematics and controller design, is not a key aspect of this research. SensAble Technologies provides a package in C++ that includes the controllers. To enable communication with a slave site, a general communication package has been developed in C++. This package can send/receive in six separate channels via UDP/IP or analogue inputs/outputs.

---

[1]Denavit-Hartenberg

MHMP Site

a) UDP communication

MHMP Site

b) Analogue communication
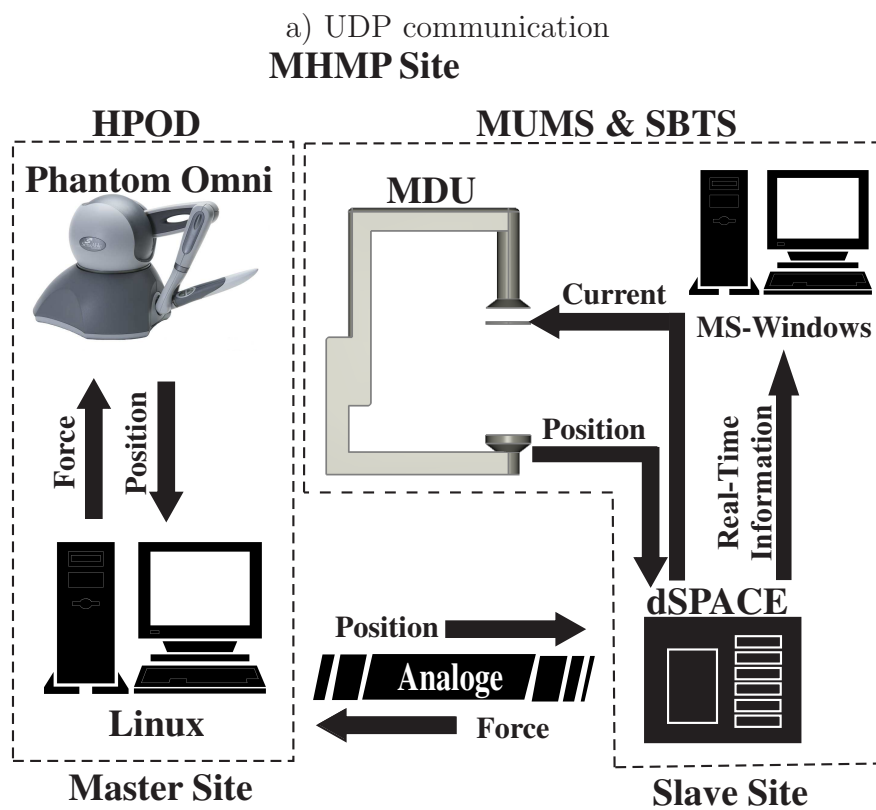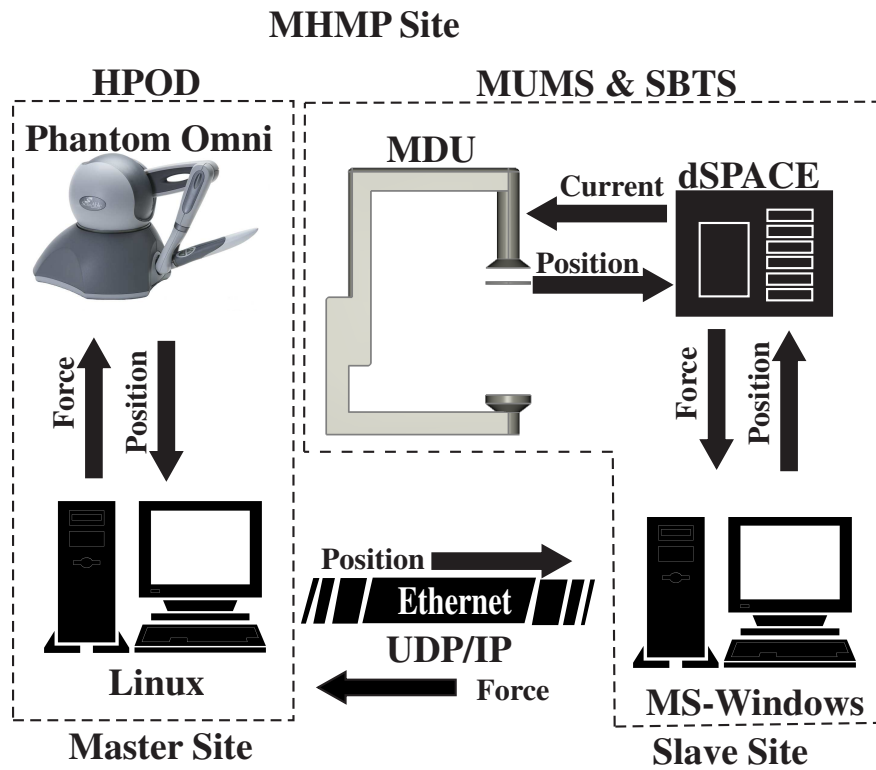
Figure 2.15: Schematic representation of the magnetic haptic micromanipulation platform (MHMP)

Figure 2.16: PhanTom Omni device by SensAble Technologies [98]

Table 2.1: Haptic PhanTom Omni Device Technical Specification [98]

| | |
|---|---|
| Force feedback workspace | $\succ$ 160 W $\times$ 120 H $\times$ 70 D mm |
| Range of motion | Hand movement pivoting at wrist |
| Nominal position resolution | $\succ$ 450 dpi$\approx$0.055 mm. |
| Back drive friction | $\prec$ 1 oz (0.26 N) |
| Maximum exertable force at nominal (orthogonal arms)position | 0.75 lbf. (3.3 N) |
| Continuous exertable force | $\succ$ 0.2 lbf. (0.88 N) |
| Stiffness | x-axis $\succ$ 7.3 lbs./in. (1.26 N/mm.) |
| | y-axis $\succ$ 13.4 lbs./in. (2.31 N/mm.) |
| | z-axis $\succ$ 5.9 lbs./in. (1.02 N/mm.) |
| Inertia (apparent mass at tip) | $\approx$0.101 lbm. (45 g) |
| Force feedback | x, y, z |
| Position sensing [Stylus gimbal] | x, y, z (digital encoders) [Pitch, roll, yaw ($\mp$5% linearity potentiometers) |

## 2.8 Summary

Magnetic levitation can be achieved through the interaction between the magnetic flux density field and the magnetic dipole moment of the levitated object. The source of the magnetic flux is a set of electromagnets, each of which is supplied with an external current source. Problems surrounding magnetic levitation can be classified as magneto-static types; hence, based on magneto-static equations, the magnetic force experienced by a magnetic dipole moment can be calculated in the external magnetic flux.

The magnetic drive unit (MDU) is responsible for generating a controllable magnetic flux distribution within the air gap. The MDU consists of an arrangement of multiple electromagnets, a pole-piece, and a soft iron yoke. The pole-piece connects the poles of the electromagnets to increase the controllability and stability of the system regarding the distribution of the magnetic flux, and the C-shaped yoke is used to generate a closed-loop magnetic circuit that results in a uniform magnetic flux with larger gradients.

In our research, the magnetic reluctant model (MRM) and magneto-static finite element analysis of the MDU revealed a magnetic short-circuit in the MDU. The MRM demonstrated that undesired flux leakages within the internal yoke parts (a magnetic short-circuit) measured 15% of the magnetic flux produced by the yokes' electromagnets. Furthermore, a finite element analysis demonstrated that undesired flux leakages result in horizontal shifts of the $B_{max}$. For experimental analyses of the produced magnetic flux, an automated magnetic field scanner was built to determine the profile of the magnetic gradient.

The magnetic untethered microrobotic system (MUMS) is the heart of the magnetic-haptic micro-manipulation platform (MHMP) in the sense that it produces a non-contact motion actuation mechanism. The MUMS consists of three main components: the MDU, the real-time controller, and a microrobot. The MHMP includes a master site and a slave site that can communicate with each other via analog and/or Ethernet connections. The slave site consists of two basic systems (the MUMS and a scaled bilateral teleoperation system [SBTS]) and the master site also consists of two systems, namely the haptic-PhanTom omni device (HPOD) and a Linux server computer.

# Chapter 3

# Analytical Modeling and Position Control[1]

## 3.1 Introduction

Magnetic force modeling is the first step to achieving high precision motion control. Accordingly, this chapter first demonstrates a mathematical model for the magnetic field gradients produced by the MDU, after which the dynamics of the MUMS is presented, based on the developed magnetic force model, and various control systems are designed and implemented to enhance the performance of the MUMS with regards to motion control and accuracy. Next, a control allocation method as the key concept for over-actuated systems is employed in the control system design for optimal and proper distribution of control inputs. Finally, a pre-magnetized pole-piece acting as a "proof-of-concept" is proposed to reduce the operational energy consumption of the MDU.

---

[1]Portions of this section are published by Moein Mehrtash and Mir Behrad Khamesee, 2011, Design and Implementation of LQG\LTR Controller for a Magnetic Telemanipulation System-Performance Evaluation and Energy Saving, Microsystem Technologies, 17(5-7), pp. 1145-1152, Saman Hosseini, Moein Mehrtash and Mir Behrad Khamesee, 2011, Design, Fabrication and Control of a Magnetic Capsule Robot for the Human Esophagus, Microsystem Technologies, 17(5-7), pp. 1135-1143, and Moein Mehrtash, Noaoki Tsuda, and Mir Behrad Khamesee, 2011, Bilateral Macro-Micro Teleoperation Using Magnetic Levitation, Mechatronics, IEEE/ASME Transactions on, 16(3),pp. 459-469

## 3.2 Magnetic Force Model Calculation

A substantial number of studies on magnetic actuation mechanism have focused on the development of accurate mathematical models for magnetic forces. The proposed models generally assume that magnetic force is directly proportional to the squared coil's current and inversely proportional to the squared distance between the electromagnet and a ferromagnetic object [37; 50; 85; 86]. Lin *et al* [67] introduced a mathematical model whose magnetic force is linearly proportional to the current and inversely proportional to the fourth power of distance.

In the reviewed literature, the magnetic force models have approximately calculated the magnetic force on the axis of an individual electromagnet. For 3-D magnetic force calculation, Craig *et al* [22] proposed a magnetic force model based on the numerical analysis of two electromagnets with parallel axes. *Craig*'s study [22] showed: 1) the magnetic force parallel to the axis of the electromagnet is linearly proportional to current and distance, and 2) in the plane which is perpendicular to axis of the electromagnet, the magnetic force is proportional to the current and inversely proportional to the squared distance. *Shameli* [99] investigated experimental frequency response identifications to derive a dynamic magnetic force model, addressing a time lag between the current and the magnetic field and proposing a magnetic force model that is linearly proportional to current and distance.

Due to the geometrical complexities of the MDU (i.e., that it includes six-pair of electromagnets connected by a pole-piece), the mathematical models found in the literature cannot be fitted to our special case of the MDU. The following sections describe some basic methods to simplify the magnetic field modeling process of the MDU and proposing a novel magnetic forces model based on the experimental system identifications.

### 3.2.1 Horizontal magnetic gradients

Section 2.1 demonstrated that a horizontal force is generated by the gradient of the z-component of a magnetic field (Bz) produced by the MDU. Thus, this section investigates, both numerically and experimentally, the z-component of the produced magnetic field to derive a mathematical model for the magnetic

Load One Electromagnet
of The MDU

Scan The Working Space
By The AMFS

Find Mathematical Model
of Magnetic Gradient

Using Geometric Transformation
To Find All Electromagnets'
Magnetic Gradient

Using Summation Effect To Find
The Total Magnetic Gradient
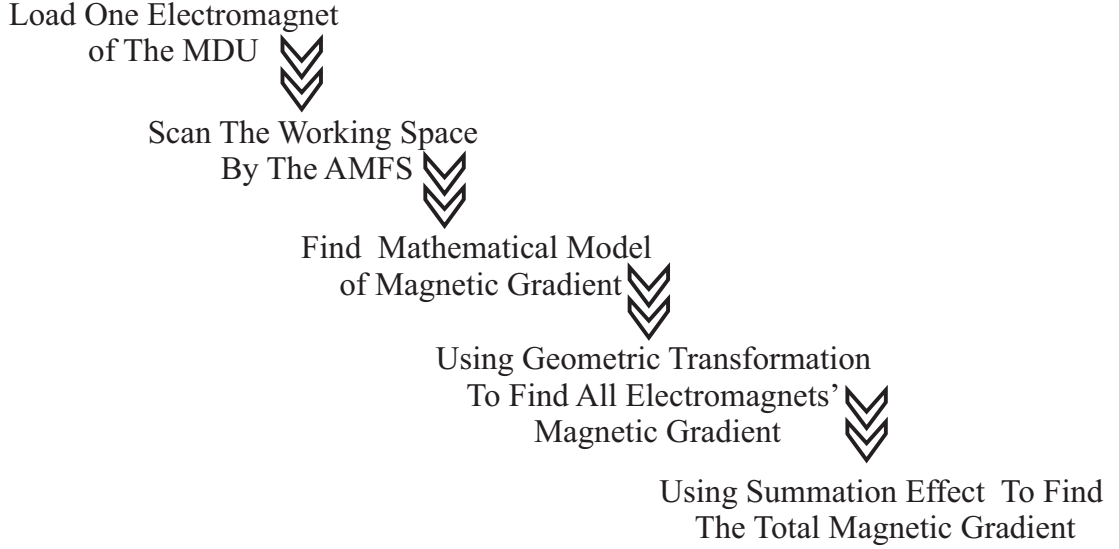
Figure 3.1: The schematic process of the MDU's magnetic gradient identification

force. The experimental measurements are carried out using the developed AMFS discussed in Section 2.5. In the experimental magnetic field measurement, the scanning range is defined as $x, y \in [-50, 50]$ mm and $z \in [-65, 95]$ mm. The AMFS measures the z-component of the magnetic field with 10 mm step in $x$, $y$, and $z$ direction. Experimental measurements validates the numerical analyses by the COMSOL software that the magnitude of magnetic field produced in the z-direction is changed linearly with the uniform current of the electromagnets.

The MDU has six pairs of electromagnets, so labor-intensive system identification with six inputs must be carried out to find an accurate model for the z-component of the magnetic field ($B_z$). To reduce the experimental measurements for magnetic field identification, one electromagnet can be loaded and the produced magnetic field model inside the workspace can be modeled. Then, the MDU magnetic model can be derived by using the geometry transformation and the summation effect. Fig. 3.1 demonstrates this process schematically.

Inside the MDU's workspace, experimental measurements of the magnetic field produced by an individual electromagnet (electromagnet number two) demonstrate the horizontal gradient $\partial B_z / \partial x$, which varies mainly by $x$ and also somewhat by $y$, at a constant vertical position, as shown in Fig. 3.2. Figure 3.4 shows that the horizontal gradient $\partial B_z / \partial y$ varies mainly by $y$ and much less signifi-
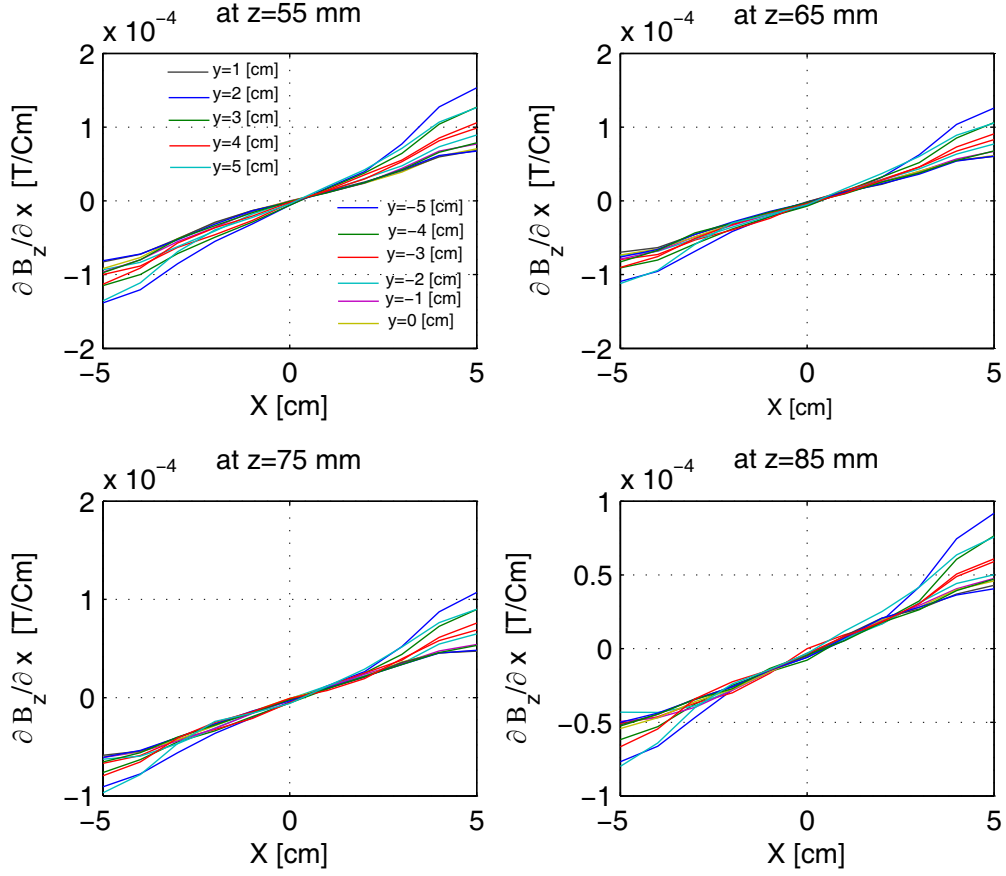
Figure 3.2: variation of horizontal magnetic field gradients ($\partial B_z/\partial x$) Vs. position

cantly by $x$. To obtain mathematical relations for the magnetic gradients, curve
fitting technique is used. Based on experimental measurements, the magnetic
gradients can be properly estimated by linear functions, as shown in Fig. 3.5.
The mathematical relation for magnetic gradients can be defined as

$$\frac{\partial B_z}{\partial x} = (\alpha_x x + \beta_x) I_2 \tag{3.1}$$

$$\frac{\partial B_z}{\partial y} = (\alpha_y y + \beta_y) I_2 \tag{3.2}$$

where $I_2$ presents electromagnet number two's coil current. Parameters $\alpha_x$, $\beta_x$
$\alpha_y$, and $\beta_y$ and are magnetic gradients parameters determined by experimental
measurements and the linear least square curve fitting . Due to geometrical con-
strains, the parameter $\beta_x$ can be assumed as zero. Figure 3.5 represents the linear

trend-lines of magnetic gradients by vertical positions. As shown in Fig. 3.6, the magnetic gradient's coefficients ($\alpha_x$, $\beta_x$, $\alpha_y$, and $\beta_y$) can be linearly approximated with respect to the vertical position [the magnetic gradient's coefficients changes less than 10 percent over the entire vertical working space, so selecting the average of magnetic gradient's coefficients ($\overline{\alpha}_x$, $\overline{\beta}_x$, $\overline{\alpha}_y$, and $\overline{\beta}_y$) over vertical distance can reduce the complexity of the Eq. 3.3 and 3.4]. Thus, the full horizontal magnetic gradients can be stated as ($\beta_x \approx 0$),

$$\frac{\partial B_z}{\partial x} = (\gamma_{x,xz} xz + \gamma_{x,x} x) I_2 \tag{3.3}$$

$$\frac{\partial B_z}{\partial y} = (\gamma_{y,yz} yz + \gamma_{y,y} y + \gamma_{y,z} z + \gamma_{y,0}) I_2 \tag{3.4}$$

where $\gamma$s are parameters of the horizontal magnetic gradients which are determined by experimental measurements. By geometry transformation, magnetic gradients of each electromagnets can be presented by

$$
\begin{aligned}
\frac{\partial B_z}{\partial x}\bigg|_{n=i} &= [(\gamma_{x,xz} z + \gamma_{x,x} - \gamma_{y,yz} z - \gamma_{y,y}) x \, \cos^2 \theta_i + (\gamma_{x,xz} z + \gamma_{x,x}) x + \\
&\quad (\gamma_{y,yz} z + \gamma_{y,y} - \gamma_{x,xz} z - \gamma_{x,x}) \frac{y}{2} \sin 2\theta_i + (\gamma_{y,z} + \gamma_{y,0}) \sin \theta_i] I_i \tag{3.5} \\
\frac{\partial B_z}{\partial y}\bigg|_{n=i} &= [(\gamma_{x,xz} z + \gamma_{x,x} - \gamma_{y,yz} z - \gamma_{y,y}) \left( y \sin^2 \theta_i - \frac{x}{2} \sin 2\theta_i \right) + \\
&\quad (\gamma_{y,yz} z + \gamma_{y,y}) y + (\gamma_{y,z} + \gamma_{y,0}) \cos \theta_i] I_i \tag{3.6}
\end{aligned}
$$

where $\theta_i$ and $I_i$ are the geometrical angle (Fig. 3.3) and coil current of $i^{th}$ electromagnet ($\theta = [-\frac{\pi}{3}, 0, \frac{\pi}{3}, \frac{2\pi}{3}, \pi, -\frac{2\pi}{3}]$ are geometrical angles for electromagnet number one to six), respectively. Using the magnetic field summation effect, the produced horizontal magnetic gradients by the MDU can be derived as

$$\frac{\partial B_z}{\partial x} = \sum_{i=1}^{6} \frac{\partial B_z}{\partial x}\bigg|_{n=i} \tag{3.7}$$

$$\frac{\partial B_z}{\partial y} = \sum_{i=1}^{6} \frac{\partial B_z}{\partial y}\bigg|_{n=i} \tag{3.8}$$

47
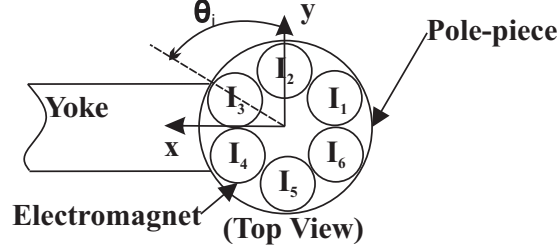
Figure 3.3: geometrical angle and coil current

Furthermore, by substituting the geometrical angles, the horizontal magnetic gradients of the MDU are represented as

$$
\begin{aligned}
\frac{\partial B_z}{\partial x} = {} & \frac{x}{4} \left( \gamma_{x,xz} z + \gamma_{x,x} + 3 \left( \gamma_{y,yz} z + \gamma_{y,y} \right) \right) \left( I_1 + I_3 + I_4 + I_6 \right) + \\
& x \left( \gamma_{x,xz} z + \gamma_{x,x} \right) \left( I_2 + I_5 \right) + \\
& \frac{\sqrt{3} y}{4} \left( \gamma_{x,xz} z + \gamma_{x,x} - \gamma_{y,yz} z - \gamma_{y,y} \right) \left( I_1 - I_3 + I_4 - I_6 \right) + \\
& \frac{-\sqrt{3}}{2} \left( \gamma_{y,z} z + \gamma_{y,0} \right) \left( I_1 - I_3 - I_4 + I_6 \right)
\end{aligned}
\tag{3.9}
$$

$$
\begin{aligned}
\frac{\partial B_z}{\partial y} = {} & \frac{y}{4} \left( \gamma_{y,yz} z + \gamma_{y,y} + 3 \left( \gamma_{x,xz} z + \gamma_{x,x} \right) \right) \left( I_1 + I_3 + I_4 + I_6 \right) + \\
& y \left( \gamma_{y,yz} z + \gamma_{y,y} \right) \left( I_2 + I_5 \right) + \\
& \frac{\sqrt{3} x}{4} \left( \gamma_{x,xz} z + \gamma_{x,x} - \gamma_{y,yz} z - \gamma_{y,y} \right) \left( I_1 - I_3 + I_4 - I_6 \right) + \\
& \frac{1}{2} \left( \gamma_{y,z} z + \gamma_{y,0} \right) \left( I_1 + 2I_2 + I_3 - I_4 - 2I_5 - I_6 \right)
\end{aligned}
\tag{3.10}
$$

To validate the estimated model obtained through geometric transformation and magnetic field summation, an experimental measurement was carried out. Figure 3.8presents the measured magnetic field when two electromagnets (numbers one and two) are equally loaded. Figure 3.7 presents the estimated magnetic field by geometric transformation and magnetic field summation when electromagnets one and two are equally loaded. The contour plots in Fig 3.8 and 3.7 demonstrate that the estimated model can predict the $B_{max}$ position with good accuracy. Figure 3.9 shows that the linear summation modeling and electromag-
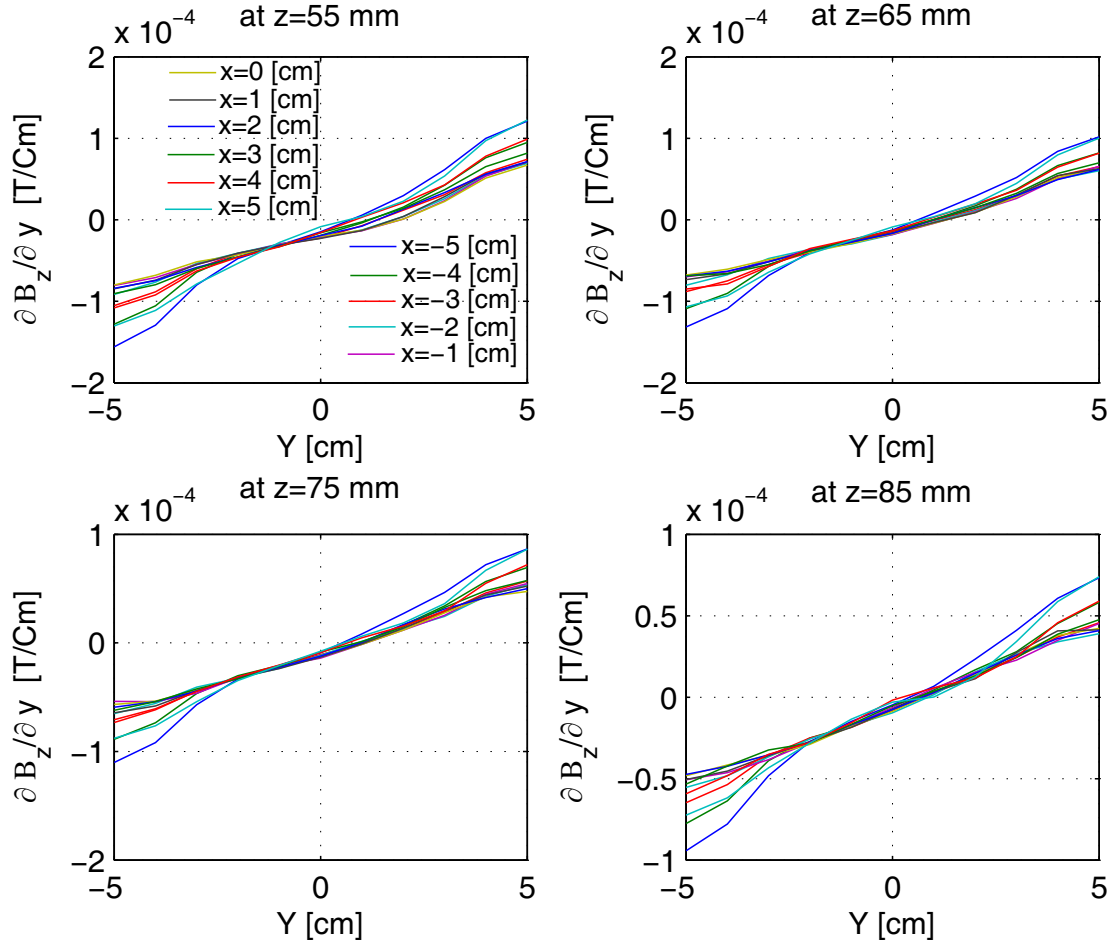
Figure 3.4: variation of horizontal magnetic field gradients $(\partial B_z/\partial y)$ by position
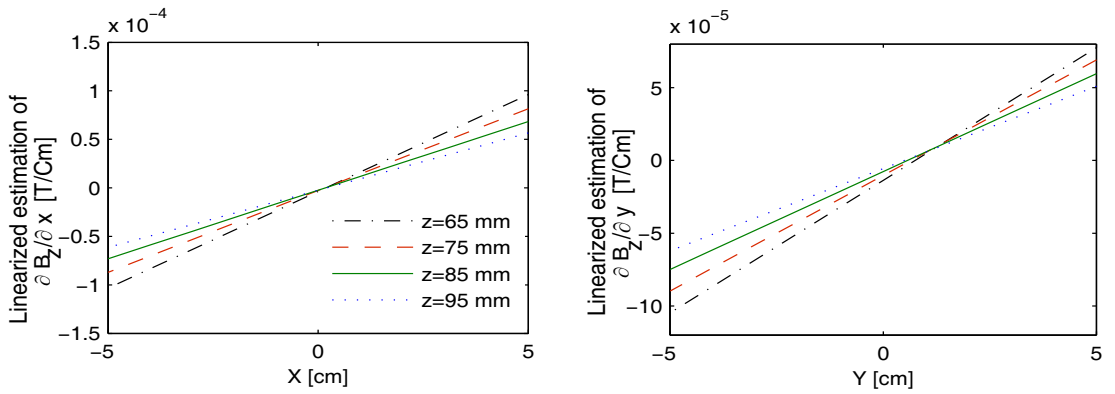


Figure 3.5: Linear trend lines for magnetic gradients in the workspace
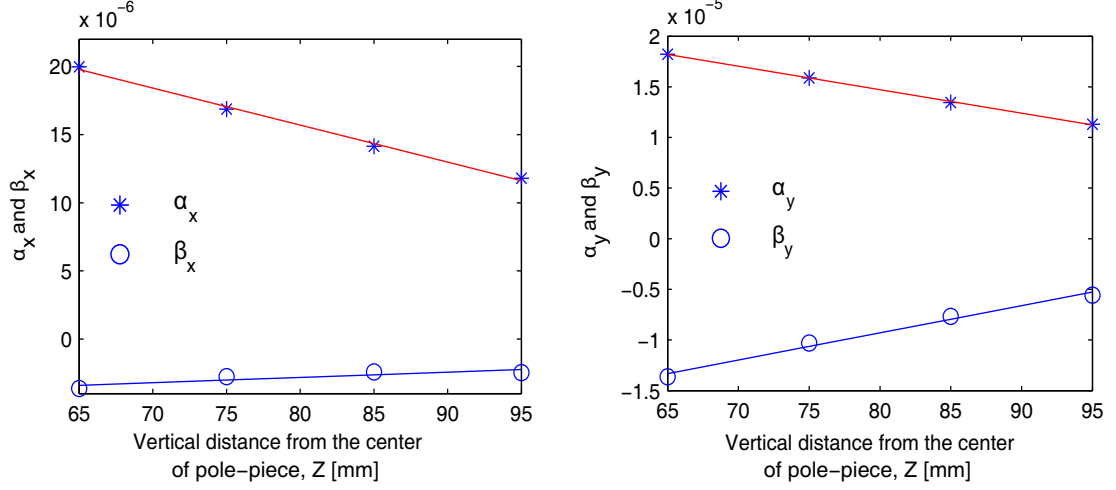
Figure 3.6: Variation of horizontal magnetic gradients by vertical position

nets' magnetic field interaction on each other produce a maximum 15% error in the range of $50 \times 50 \ mm^2$ , in our smaller working envelope this error is less than 12%. Therefore, the magnetic field summation effect presented an acceptable performance by simplifying the process of magnetic field estimation

### 3.2.2 Vertical magnetic gradients

This section presents a mathematical model for the vertical magnetic gradient which producing the vertical magnetic force model. *Shameli* [99] followed an experimental method to derive a mathematical model for the levitation force.His experimental measurements demonstrated that increasing the distance from the pole-piece will drastically decrease the magnetic gradient (see Fig. 3.10). In a small vertical range of our working envelope, $z \in [65, 95] \ mm$, the vertical gradient can be represented as

$$\frac{\partial B_z}{\partial z} = (\alpha_z z + \beta_z) \sum_{i=1}^{6} I_i \tag{3.11}$$

where $\alpha_z$ and $\beta_z$ are fitting constants determined by magnetic field measurement. Experimental analyses demonstrate that Eq. 3.11 provides an accurate
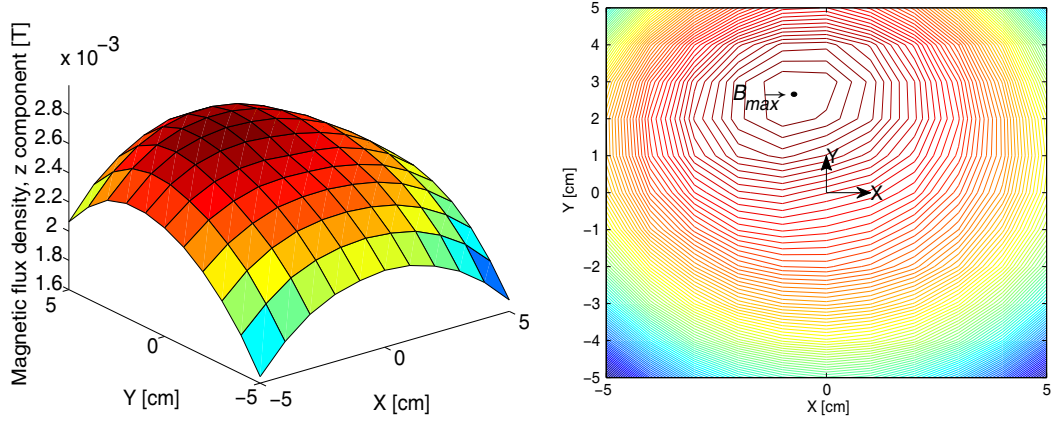
Figure 3.7: Surface and contour plot of magnetic flux density z-component obtained by the geometric transformation and magnetic field summation effect at z=75 mm and electromagnet number one and two are equally loaded with 1A current
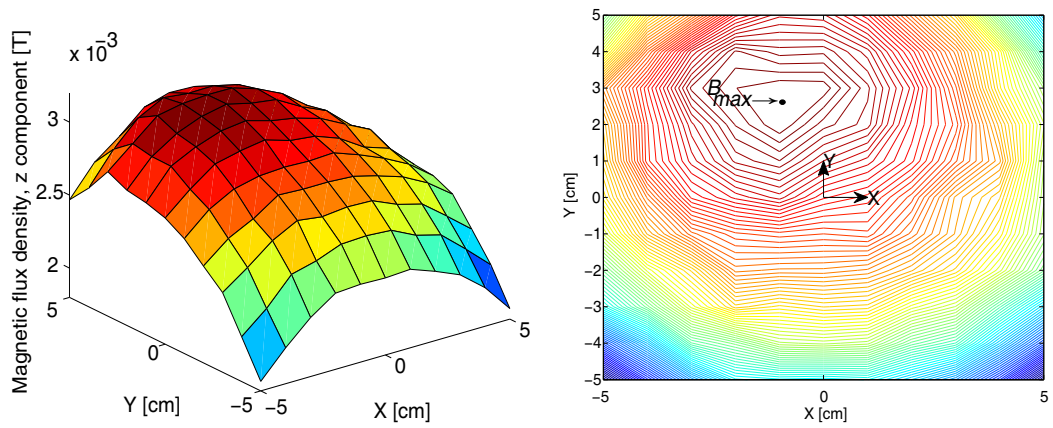


Figure 3.8: Surface and contour plot of magnetic flux density z-component obtained by experimental measurement, at z=7.5 mm and electromagnet number one and two are equally loaded with 1A current
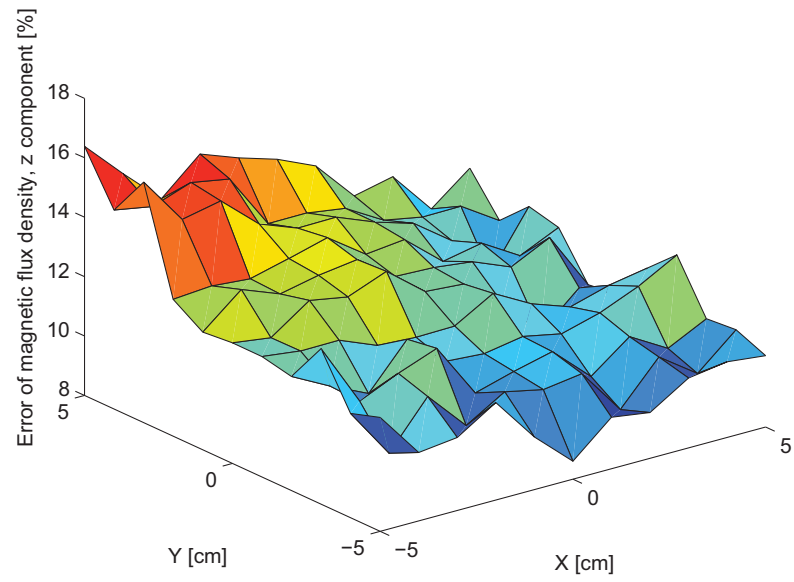
Figure 3.9: Error of estimating magnetic flux density z-component by the geometric transformation and magnetic field summation effect, at z=75 mm and electromagnet number one and two are equally loaded with 1A current
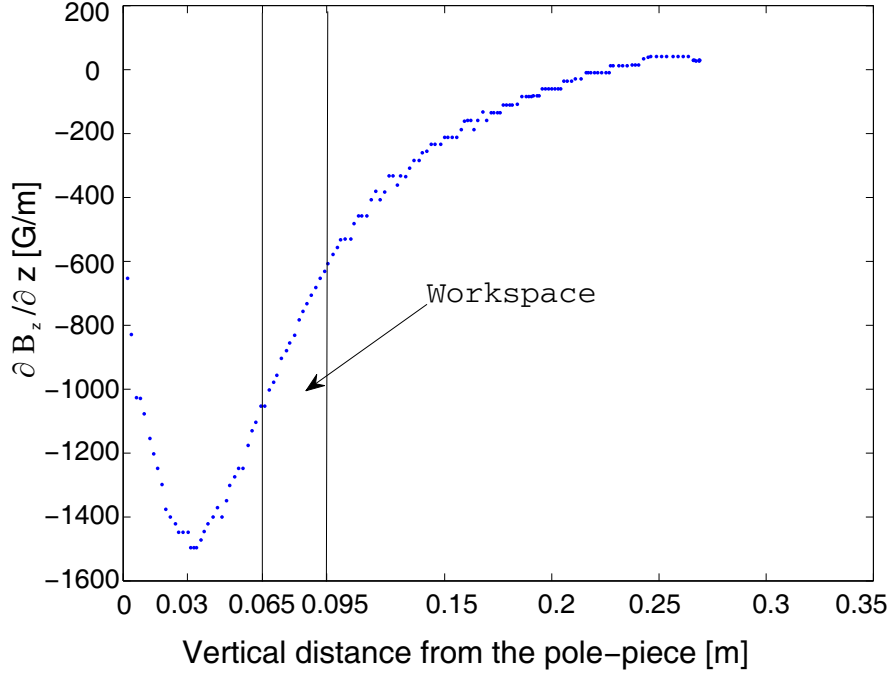
Figure 3.10: Experimental data for vertical gradient of the MDU

model with regards to the small horizontal distance from the center of the pole-piece, $d_{xy} = \sqrt{x^2 + y^2}$. By levitating a small permanent magnet in 30 random positions inside the workspace, the vertical magnetic gradient can be validated, since the vertical magnetic force equals the weight of the permanent magnet. Figure 3.11.(a) presents the accuracy of Eq. 3.11 versus random horizontal positions. The figure demonstrates that for a small $d_{xy}$, Eq. 3.11 shows good accuracy. However, increasing $d_{xy}$ can cause up to 60% error in the model. A novel mathematical vertical gradient has been proposed as

$$\frac{\partial B_z}{\partial z} = \frac{(\alpha_z z + \beta_z)}{1 + \gamma_z d_{xy}} \sum_{i=1}^{6} I_i \qquad (3.12)$$

where $\gamma_z$ is a magnetic field parameter and is determined by experimentation. As shown in Fig. 3.11.(b), for the modified model, the error is less than 9% in the MDU's workspace.

<div style="text-align:center">(a) Using model in Eq. 3.11      (b) Using improved model in Eq. 3.12</div>
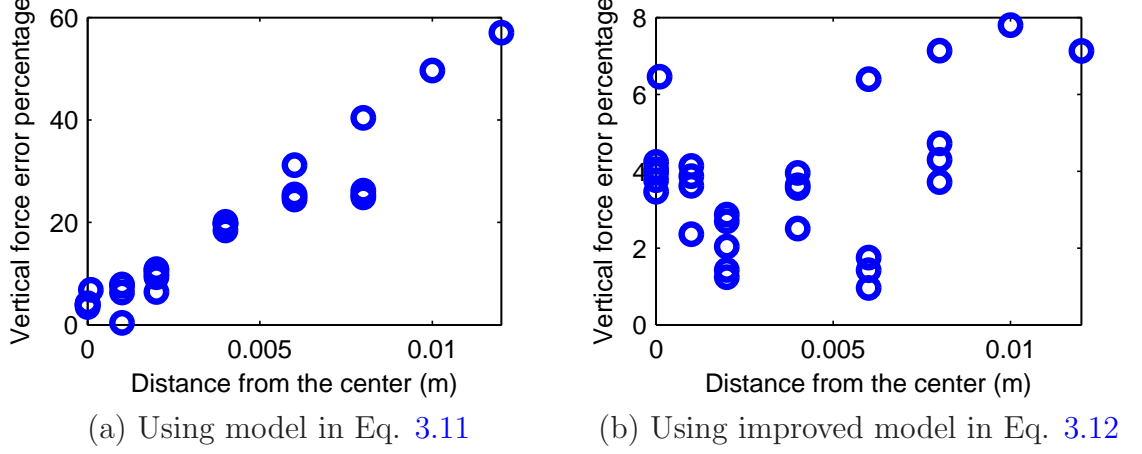
<div style="text-align:center">Figure 3.11: modeling error of vertical magnetic field gradient</div>

### 3.2.3   Reducing the operational energy consumption

The introduced pole-piece can be replaced by a pre-magnetized pole-piece to generate vertical magnetic field gradients with lower energy consumption. The pre-magnetized pole-piece has a vertical magnetization vector that magnifies the magnetic field in the z-direction produced by the MDU's electromagnets. To verify the capability of the pre-magnetized pole-piece, the z-component of magnetic field in the air-gap was measured experimentally. As presented in Fig. 3.12, the vertical gradients of magnetic field induced by the pre-magnetized pole-piece are approximately uniform over the entire MDU's workspace. Inside the working envelop, vertical gradients can be estimated as an average value of $5 \times 10^{-4}$T/cm, as Fig. 3.12 shows, this can lead to a uniform weight compensation. Thus, applied vertical force due to integrating the pre-magnetized pole-piece can be calculated as

$$f_z = M \frac{\partial B_z}{\partial z} = \left( \frac{B_r}{\mu_0} \right) \frac{\partial B_z}{\partial z} \tag{3.13}$$

where $B_r$ is the residual flux density of the permanent magnet. To present the effectiveness of the pre-magnetized pole-piece, a weight compensation factor ($WCF$) is introduced as the ratio of compensated weight to real-physical

weight. Hence, the *WCF* of the MDU is

$$WCF = \frac{\partial f_z}{\partial mg} = \left(\frac{B_r}{\rho g \mu_0}\right)\frac{\partial B_z}{\partial z} = \left(\frac{1.2}{7400 \times 9.8 \times 4\pi \times 10^{-7}}\right) \times 5 \times 10^{-2} = 0.66$$

(3.14)

where $\rho$ is the density of NdFeB. Here, an NdFeB permanent magnet was used as the head of the microrobot. The parameter *WCF* shows that 66% of the microrobot's head (permanent magnet) can be compensated by the pre-magnetized pole-piece magnetic field, meaning that the same amount of operational energy can be saved for levitating the microrobot's head in the workspace. Experimental analysis shows that increasing the magnetization of the pole-piece increases not only the vertical gradient but also the horizontal gradient. The induced horizontal gradient of the pre-magnetized pole-piece tends to move the microrobot to the center of the workspace. In cases where the pole-piece is highly magnetized, the horizontal gradients produced by electromagnets cannot overcome the horizontal gradients of the pole-piece. Hence, there is trade-off to keep the maneuverability of the microrobot on the horizontal plane and to reduce energy consumption. In this study, the pre-magnetized pole-piece produces negligible horizontal gradients, and therefore the pre-magnetized pole-piece does not change the proposed magnetic force model in the horizontal plane. Adding a constant term to the proposed vertical magnetic force model presents the effect of the pre-magnetized pole-piece.

## 3.3 Dynamics and Control

This part firstly presents the linearized dynamical model of the MUMS based on the proposed magnetic force model, and a control allocation method is used to simplify the obtained dynamical model. Various linear strategy control systems are then employed to enhance the performance of the MUMS in motion control and accuracy. To verify the proposed magnetic force model and effectiveness of the control systems, this section also discusses experiments using the MUMS prototype for 3-D motion control. The primary purpose of this prototype is to investigate the MUMS's performance in positioning the microrobot, not the
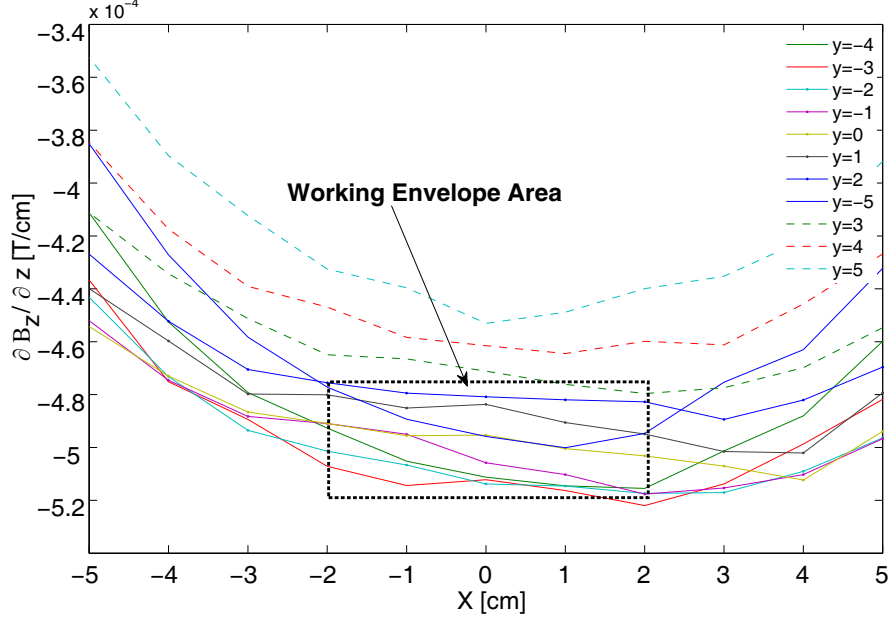
Figure 3.12: Produced constant vertical gradient by the pre-magnetized pole-piece

detailed design of the microrobot. The microrobot prototype is a 10mm×10mm NdFeB cylinder. The residual flux density of the microrobot is 1.2 $T$ and its total mass is 11.2 $g$. To achieve high accuracy, an aluminum disk is placed at the bottom of the workspace to generate eddy-current damping (the eddy-current damping effect will fully be discussed in Chapter 4). Previous findings ([35] and [33]) on the development of the MUMS have noted a lack of inherent dynamical damping, which causes precision and stability problems. To obtain a more precise motion control of the microrobot, a conductive plate is placed below the microrobot. In [35] and [33], an analytical model of eddy-current damping in the vertical motion of the microrobot was presented. In the next chapter, a new model of eddy-current damping in the horizontal motion will be introduced.

### 3.3.1  Linearized Dynamical Model

In general, a dynamical model of the MUMS can be obtained from the application of *Newton*'s second law. In this study, the magnetic and gravity forces are considered as the source of external forces applied to the microrobot, and the

drag effect and eddy current damping are neglected. Thus, the dynamic of the motion can be defined by

$$m\ddot{x} = M\frac{\partial B_z}{\partial x} \tag{3.15}$$

$$m\ddot{y} = M\frac{\partial B_z}{\partial y} \tag{3.16}$$

$$m\ddot{z} = M\frac{\partial B_z}{\partial z} + mg + M\frac{\partial B_z}{\partial z}\bigg|_0 \tag{3.17}$$

where $m$, $g$, $M$, and $\frac{\partial B_z}{\partial z}\big|_0$ are microrobot's mass, gravity effect, magnetization of permanent magnet as the microrobot's head, and the vertical gradient of pre-magnetized pole-piece, respectively. By substituting the magnetic gradients from section 3.2, the dynamical model of the microrobot's motion can be derived. Since the proposed force models for magnetic gradients are all nonlinear, the dynamical model of the MUMS needs to be defined by non-linear relations. To design motion control system for the MUMS, we first consider the linearized model and evaluate the performance of the linear control strategy. Based on the derived non-linear dynamical model, the linearized dynamic of the microrobot at the center point of the workspace, $[x_c\ y_c\ z_c] = [0\ 0\ z_0]$ and $I_1 = I_2 = I_3 = I_4 = I_5 = I_6 = I_0$, can be represented as

$$m\ddot{x} - 3x\left(\left(\gamma_{x,xz} + \gamma_{y,yz}\right)z_0 + \gamma_{x,x} + \gamma_{y,y}\right)I_0 =$$
$$\frac{-\sqrt{3}}{2}\left(\gamma_{y,z}z_0 + \gamma_{y,0}\right)\left(i_1 - i_3 + i_6 - i_4\right) \tag{3.18}$$
$$m\ddot{y} - 3y\left(\left(\gamma_{x,xz} + \gamma_{y,yz}\right)z_0 + \gamma_{x,x} + \gamma_{y,y}\right)I_0 =$$
$$\frac{1}{2}\left(\gamma_{y,z}z_0 + \gamma_{y,0}\right)\left(i_1 + 2i_2 + i_3 - i_4 - 2i_5 - i_6\right) \tag{3.19}$$
$$m\ddot{z} - \alpha_z I_0 z = \left(\alpha_z z_0 + \beta_z\right)\left(i_1 + i_2 + i_3 + i_4 + i_5 + i_6\right) \tag{3.20}$$

where $i_j$ is the perturbed current for the $j^{th}$ electromagnet ($j = 1, \cdots, 6$) and $I_0$ can be determined from the following relation,

$$\textit{Stable levitation condition at center point} \Rightarrow \sum F_z = 0 \Rightarrow$$

$$\frac{(\alpha_z z_c + \beta_z)}{1 + \gamma_z \sqrt{x_c^2 + y_c^2}} \sum_{i=1}^{6} I_i - mg = 0 \Rightarrow I_0 = \frac{mg}{6M(\alpha_z z_0 + \beta_z)} \tag{3.21}$$

To simplify the obtained linearized dynamical model, the next section introduces a "control allocation" method.

### 3.3.2 Control Allocation Method

The control allocation problem concerns distributing a desired total control effort among a redundant set of actuators. In the MUMS' motion control, the total control effort corresponds to the magnetic forces are the available electromagnets' currents. The total control effort is defined as virtual control input, $\nu(t)$, and the electromagnet currents constitute the true control input, $u(t)$. Based on the linearized dynamical model, the virtual and true control inputs can have the following relations:

$$m\ddot{x} - 3x\left((\gamma_{x,xz} + \gamma_{y,yz})z_0 + \gamma_{x,x} + \gamma_{y,y}\right)I_0 =$$
$$\frac{-\sqrt{3}}{2}(\gamma_{y,z}z_0 + \gamma_{y,0})\underbrace{(i_1 - i_3 + i_6 - i_4)}_{\nu_x}$$
$$m\ddot{y} - 3y\left((\gamma_{x,xz} + \gamma_{y,yz})z_0 + \gamma_{x,x} + \gamma_{y,y}\right)I_0 =$$
$$\frac{1}{2}(\gamma_{y,z}z_0 + \gamma_{y,0})\underbrace{(i_1 + 2i_2 + i_3 - i_4 - 2i_5 - i_6)}_{\nu_y}$$
$$m\ddot{z} - \alpha_z I_0 z = (\alpha_z z_0 + \beta_z)\underbrace{(i_1 + i_2 + i_3 + i_4 + i_5 + i_6)}_{\nu_z} \tag{3.22}$$

and,

$$
\underbrace{\begin{bmatrix} \nu_x \\ \nu_y \\ \nu_z \end{bmatrix}}_{\nu} = \underbrace{\begin{bmatrix} 1 & 0 & -1 & -1 & 0 & 1 \\ 1 & 2 & 1 & -1 & -2 & -1 \\ 1 & 1 & 1 & 1 & 1 & 1 \end{bmatrix}}_{\mathbf{B}} \underbrace{\begin{bmatrix} i_1 \\ i_2 \\ i_3 \\ i_4 \\ i_5 \\ i_6 \end{bmatrix}}_{u} \qquad (3.23)
$$

Due to the over-actuation of the control inputs, the **B** matrix is a non-square. Thus, a constrained optimization need to be employed for the inverse of the matrix **B**. The 'pseudo-inverse' method is a constrained optimization technique that defines an inversion of the generally non-square matrix. The 'pseudo inverse' solution is the norm solution for the control allocation problem and can be formulated as

$$
\min J = \min \frac{1}{2} \left( u \right)^T \mathbf{W} \left( u \right) \qquad (3.24)
$$

subject to

$$
\nu = \mathbf{B} u \qquad (3.25)
$$

where **W** is a weighting matrix. In the MUMS, all of the control inputs have similar importance since the horizontal motion capability must be uniform in all the workspace. Thus, the weighting matrix is assumed as a square eye matrix. The control allocation matrix (CAM) is finally calculated by the "pseudo inverse"

method as [79]

$$
\underbrace{\begin{bmatrix} i_1 \\ i_2 \\ i_3 \\ i_4 \\ i_5 \\ i_6 \end{bmatrix}}_{u} = \underbrace{\begin{bmatrix} 0.25 & 0.0833 & 0.1667 \\ 0 & 0.1667 & 0.1667 \\ -0.25 & 0.0833 & 0.1667 \\ -0.25 & -0.0833 & 0.1667 \\ 0 & -0.1667 & 0.1667 \\ 0.25 & -0.0833 & 0.1667 \end{bmatrix}}_{\mathbf{CAM}} \underbrace{\begin{bmatrix} \nu_x \\ \nu_y \\ \nu_z \end{bmatrix}}_{\nu} \qquad (3.26)
$$

Therefore, the CAM modifies the dynamical model to a decoupled three inputs-three outputs dynamics. In the following sections, various linear control strategies will be implemented based on the derived linearized model.

### 3.3.3   Control System Design

In this section, vertical and horizontal controls of the microrobot is discussed. The dynamic of a levitated object is inherently unstable, and the closed-loop control strategies must be employed to stabilize the motion dynamics. Based on the linearized dynamics obtained in the previous section, the dynamic of the microrobot is unstable in vertical motion but stable in horizontal motion. Two control strategies, a linear quadratic Gaussian (LQG) controller and a PID method, are implemented in this study. The PID controller is well-tunned by numerous experimental measurements and will be used for the MHMP in this study. The LQG strategy has also been developed to compensate the low frequency cross-coupling uncertainties in the microrobot dynamics.

A proportional-integral-derivative (PID) controller is an effective control strategy widely used in industrial control systems. The PID controller's performance can be adjusted by tuning its gains. In practice, trial and error adjustment can be very useful in achieving a desired performance. Figure 3.13 presents the schematic diagram of the MUMS with PID controllers. The feed-forward signal has been
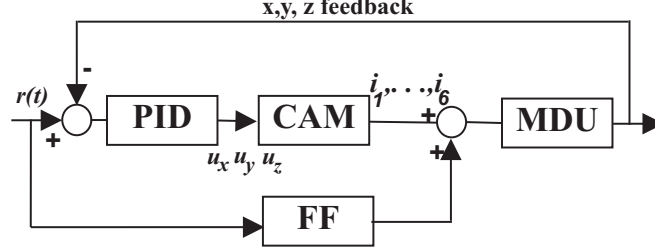
Figure 3.13: The schematic diagram of PID controller for the MUMS

calculated as,

$$u_{FF} = \frac{mg\left(1 + \gamma_z\sqrt{x_r^2 + y_r^2}\right)}{6M\left(\alpha_z z_r + \beta_z\right)} \tag{3.27}$$

The feed-forward controller can produce a major portion of the controller output. The PID controller provides the compensation signal for minimizing the set-point tracking error. Figure 3.14 and table 3.1 illustrate the PID controller performance after several trial and error adjustments. Although this technique does not provide the optimal gains for the PID controller, it nonetheless highlights the importance of each gain in performance analyses. The horizontal motion dynamic is inherently stable based on the $B_{max}$ concept. Thus, increasing the horizontal gain causes faster response in the horizontal motion but produces high cross-coupling error in the vertical motion. The horizontal commands cause vertical displacement of the microrobot, which is not desirable for motion control. Since the pattern of the electromagnet does not have the same distribution for x- and y-axes, the command in the x-axis induces different coupling errors in the z-axis compared with the command in the y-axis. The horizontal commands generate negligible cross-couplings in the horizontal plane. This finding verifies the proposed horizontal magnetic force model, showing that horizontal dynamics have the least effect on each other.

The PID controller presents robustness in handling cross-coupling errors and model uncertainties in the working envelope, Fig. 3.14 demonstrate the cross-coupling error compensation in vertical motion. In addition, the PID's gains can easily be re-tuned to achieve the desired performance. The PID's gains

Table 3.1: Performance criteria for the PID controller

| Parameter | Vertical | Horizontal |
|---|---|---|
| Rise time(s) | 0.08 | 2.5 |
| Settling time(s) | 1.6 | 2.4 |
| Overshoot(P.M.O) % | 35 | 0 |
| Undershoot (P.M.U)% | 0 | 0 |

tunning strategy and performance sensitivities were extensively investigated by Craig [20] for the employed MUMS in this research. In the following section, to accomplish high precision manipulation, a linear quadratic Gaussian (LQG) observer/controller pair is synthesized to cope with model uncertainties due to the dynamic cross-couplings.

### 3.3.4 Cross-coupling Compensation By LQG Design

In the LQG approach, the feedback gain is selected by solving the linear quadratic regulator (LQR) algebraic riccati equation, and compensator dynamics is given in terms of the observer gain designed by using the Kalman filter (KF) strategy [27]. The separation principle reduces the problem to two sub-problems. The first is the state estimation addressed by the Kalman filter theory, and the second is to find the LQR solution. Unfortunately, although the LQG compensator does not guarantee the robustness of both LQR and KF (as demonstrated in [19]), there is a way of designing LQR and KF such that the robustness properties can be recovered [26]. Specifically, as the weight matrices of LQR and KF are design parameters, the loop transfer recovery (LTR) approach for selecting these design matrices guarantees robustness in the closed-loop system. Fig. 3.15 presents the schematic diagram of the LQG controller.

In this section, the recovery of robust loop gain at the output will be implemented as a strategy for an LQG\LTR controller design (the mathematic proof and concept of this method are referenced in [65]). In the LQG\LTR method, the bounds on the loop-gain Bode magnitude plot guarantee robustness of the closed-loop to disturbance, measurement noise and unmodeled high frequency (HF) dynamics. For the high-frequency bound, assuming that the proposed mag-
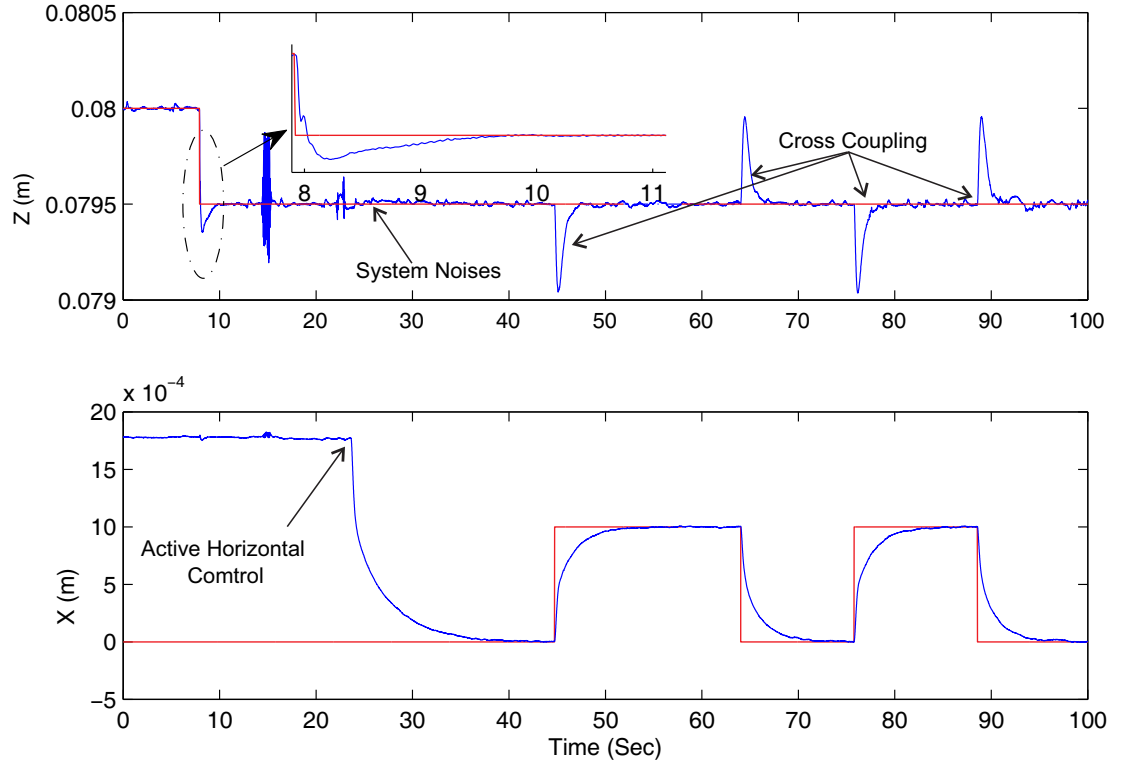
Figure 3.14: Step response of the levitated microrobot in the horizontal and vertical direction with PID controller
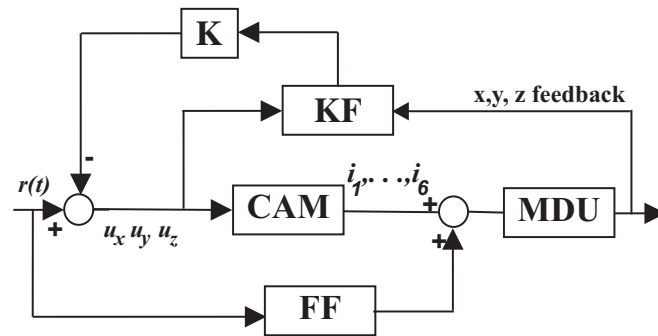


Figure 3.15: Schematic diagram of the LQG regulator using KF observer

netic levitation dynamics is accurate to within 5% up to a frequency of 80 rad/sec. Thereafter, the uncertainty grows without bounds at the rate of 20 dB/decade.

In order to make the steady-state error equal zero for the LF performance, there is an integrator in each axis, as shown in Fig. 3.16. To recover loop-gain at the output, the KF firstly is designed based on HF and LF bounds. Figure 3.17 represents the LQG\LTR's step response. Experimental tests demonstrate that the LQG\LTR controller provides outstanding capabilities to overcome the cross coupling of axes more effectively than the PID controller, Tables 3.3 and 3.2 presents the LQG\LTR's performance. In general, the vertical motion is faster than the horizontal motion, since the vertical forces acting on the microrobot are greater than the horizontal forces.

Comparing the two performance's vertical motion, the transient response of the MUMS is significantly improved by the LQG\LTR controller. The settling times for LQG\LTR and PID controllers in vertical motion are 0.22 and 1.6 seconds, respectively. In addition, the RMS cross-coupling error of the LQG\LTR strategy is nine times smaller in the vertical motion. Moreover in the vertical motion, the RMS cross coupling error is 18 $\mu m$ with LQG\LTR, while the PID provides 170 $\mu m$. The RMS error and the overshoot of the vertical motion are in a similar range for both types of controllers. The RMS error in steady state for the LQG\LTR is 10.1 $\mu m$ and 9.2 $\mu m$ for the PID controller for motion in the vertical plane.

Several experiments show that while the vertical motion RMS error is in the order of 10 $\mu m$ for both controllers, the LQG\LTR provides more robustness against system noise. Table 3.1 and Table 3.3 demonstrate that the two types of controllers provide similar performance for the MUMS in the horizontal motion, achieving an RMS error in the order of 2 $\mu m$. The rise time for LQG\LTR and PID controllers in horizontal motion is 2.2 and 2.5 seconds, respectively.

## 3.4 Summary

This chapter presents numerous advantages in using large gap magnetic suspension systems (the MUMS) in microrobotic applications. The system has the potential to generate and control magnetic fields for propelling a microrobot in
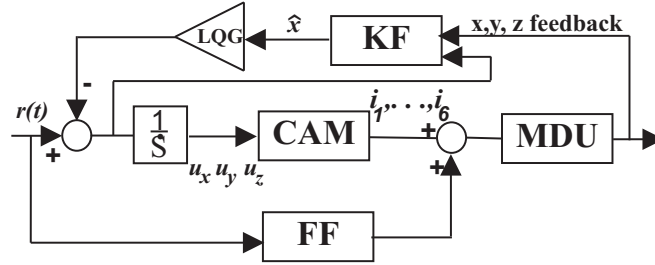
Figure 3.16: The schematic diagram of LQG\LTR controller for the MUMS
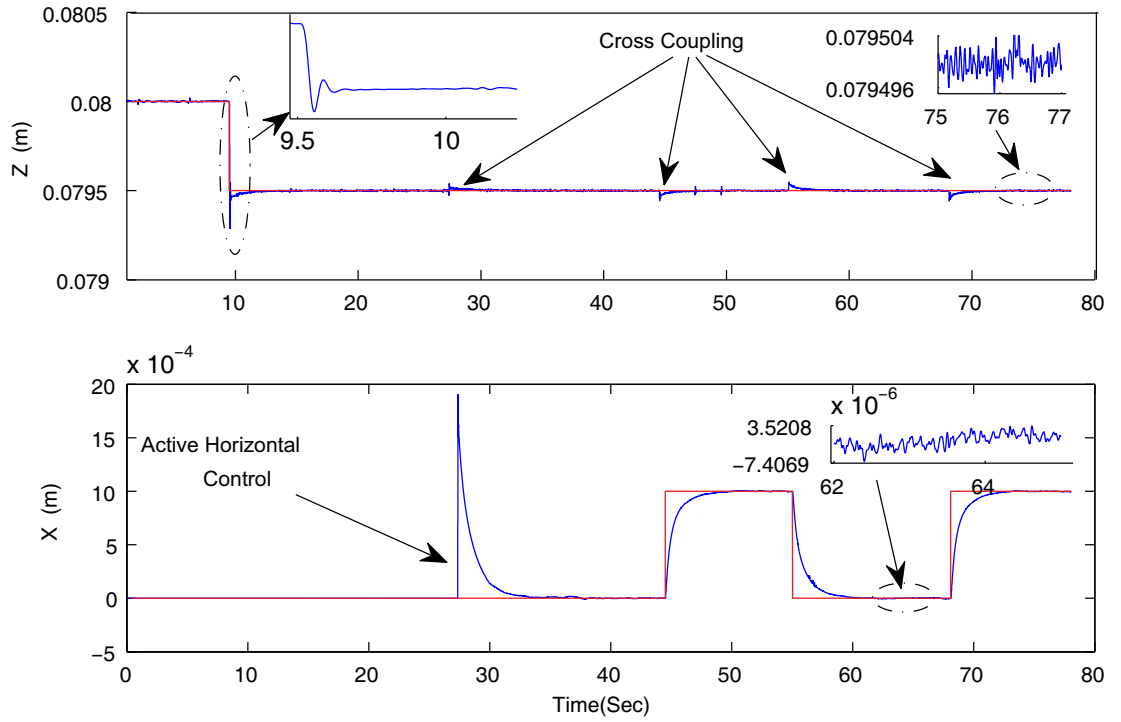


Figure 3.17: Step response of the levitated microrobot in the horizontal and vertical direction with PID controller

Table 3.2: LQG\LTR vertical performance evaluation

| Parameter | LQG\LTR |
| --- | --- |
| Peak time(s) | 0.06 |
| Rise time(s) | 0.05 |
| Settling time(s) | 0.22 |
| Overshoot % OS | 42 |
| RMS error at steady state($\mu$m) | 10.1 |
| RMS cross coupling error($\mu$m) | 18 |

Table 3.3: LQG\LTR horizontal performance evaluation

| Parameter | LQG\LTR |
| --- | --- |
| Rise time(s) | 2.2 |
| Overshoot % OS | 42 |
| RMS error at steady state($\mu$m) | 2.1 |

strictly enclosed environments within a workspace of $30 \times 32 \times 32$ $mm^3$. Based on the experimental measurements and numerical analysis, a magnetic force model was proposed for the MUMS. In experimental investigation, the 3-D motion of an 11.2 g microrobot prototype was demonstrated with a PID control system strategy. This investigation shows that the RMS error at a steady-state position is in the order of 9.2 $\mu$m in a vertical direction and 1.9 $\mu$m in a horizontal direction. The second major finding presented here concerns the axes' cross-coupling errors. Horizontal motion produces an RMS error cross-coupling in the order of 170 $\mu$m in the vertical direction, while vertical motion causes insignificant cross-coupling in the horizontal direction. These findings enhanced our understanding of system dynamics and prompted the development of the LQG\LTR-based control system. The LQG\LTR controller reduces to 18 $\mu$m the RMS error cross-coupling from the previous best of 170 $\mu$m with the PID controller. The LQG\LTR control system also provides high resolution position control, and the RMS errors of steady state in horizontal and vertical motion are 10.1 $\mu$m and 2.1 $\mu$m, respectively. Such an achievement allows for greater potential to manipulate micro-objects and perform complex micro-domain tasks.

Our investigation of a proposed pre-magnetized pole-piece has led to a "proof-of-concept" system that is capable of 66% enrgey consumption reduction. This pole-piece generates uniform vertical magnetic gradients inside the system workspace to compensate for a portion of the microrobot weight.

# Chapter 4

# Modeling and Analysis of Eddy-Current Damping Effect[1]

## 4.1 Introduction

The previous findings [33; 35] on the development of the MUMS have noted a lack of inherent dynamical damping, which causes precision and stability problems. To obtain a more precise motion control of the microrobot by the MUMS, a conductive plate is placed below the microrobot to produce an eddy-current damping [33; 35], shown schematically in Fig. 4.1. In [35] and [33], an analytical model of eddy-current damping in the vertical motion of the microrobot was presented. Building on that research, here, the experimental measurements reveal that the eddy-current damping produced by the conductive plate in the horizontal motion of the microrobot plays a key role in the performance of the microrobot's horizontal motions, the focus of this chapter. In this study, we investigate the eddy-current damping force in the horizontal motion and then an analytical relation for this damping force is introduced. Since the only source of dynamical damping in magnetic-based mechanisms is eddy-current damping, the proposed analytical model for this damping force can be used in the design cycle for developing magnetic-based mechanisms. The eddy-current phenomena have

---

[1]Portions of this section are published by Moein Mehrtash and Mir Behrad Khamesee, Modeling and Analysis of Eddy Current Damping for High Precision Magnetic Microrobotic Platform, Magnetics, IEEE Transactions on, 10.1109/TMAG.2013.2245675
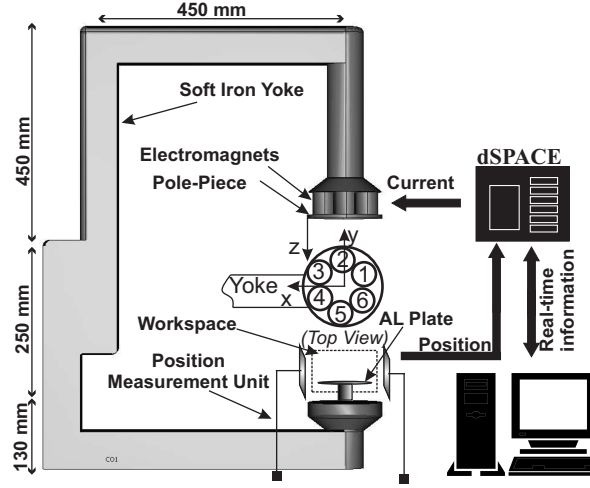
Figure 4.1: Schematic view of the magnetic drive unit (MDU) and the conductive plate location [74]

theoretically been understood since the late 1800s [115]. However, our interest in the understanding of the eddy-current damping is the result of the MUMS's magnetic modeling and experimental validations. Towards the goal of increasing the damping force using the eddy-current technique, Plissi et al [87] investigated the use of eddy-current damping for a multi-stage pendulum suspension. A particular approach was addressed that uses eddy-current damping as a replacement or supplement to an active damping for modes of the pendulums, which results in a practical alternative to the development of very low noise sensors for active damping of a trio of pendulums. Sodano and Bae [107] extensively reviewed the use of eddy-current damping for suppression of vibrations and magnetic braking in many areas, such as vibration control of bearings and rotors [15; 112; 119], high accuracy motion control for microfabrication devices [33; 35; 45], eddy-current brakes [16; 43; 110], and magnetic shock absorbers [31].

This chapter is organized to firstly demonstrate the analytical relations for the distribution of eddy-current density inside the conductive plate and eddy-current damping force. Finally, the validity of the analytical eddy-current damping force in the horizontal plane are discussed by experimental investigations.

## 4.2  Eddy-Current Modeling

Previous studies [33; 35] at the MagLev Microbotic Lab, University of Waterloo have demonstrated that placing a circular aluminum plate below the working space of the microrobot increases the dynamical damping for vertical motions of the microrobot. The eddy-currents induced in the aluminum plate generate considerable eddy-current damping, which suppresses the microrobot's motion vibrations and results in higher stability and precision for vertical motions. Moreover, experimental investigations indicate that the aluminum plate enhances the horizontal motion accuracy, which allows the horizontal eddy-current damping to be generated by this plate.

In the reference frame of the aluminum plate, the magnetic field changes cause the microrobot's motion; this changing of the magnetic field induces eddy-currents in the above mentioned plate. The direction of these currents opposes the change in the magnetic field itself. A Lorentz force acts on the eddy-currents, which causes a damping effect. In the MUMS, the time-varying magnetic field of the MDU and the magnetic field of the microrobot's head cause the total change of magnetic field passed through the plate. Figure 4.2 demonstrates the performance comparison of controlling the microrobot's horizontal position with/without of the eddy-current damping produced by placing an Aluminum plate under the workspace. As shown in this figure, the eddy-current damping increases the dynamical damping of the systems and results in overcoming the vibration and improving the motion precision. This section introduces our proposed mathematical model for the calculating the horizontal eddy-current damping that occurs when a circular aluminum plate is placed below the working space of the microrobot.

### 4.2.1  Eddy-current distribution

This section presents the analytical solution for the eddy-current distribution inside the conductive plate placed below the working space of the microrobot. The changing magnetic field is taken to be generated by alternating the current of the carrying wire loop. The wire is placed horizontally, with its center at the origin point (Fig. 4.3) with horizontal velocity ($v$). Two loops of current are used to model the magnetic field produced by the MDU (loop no. 2 with the
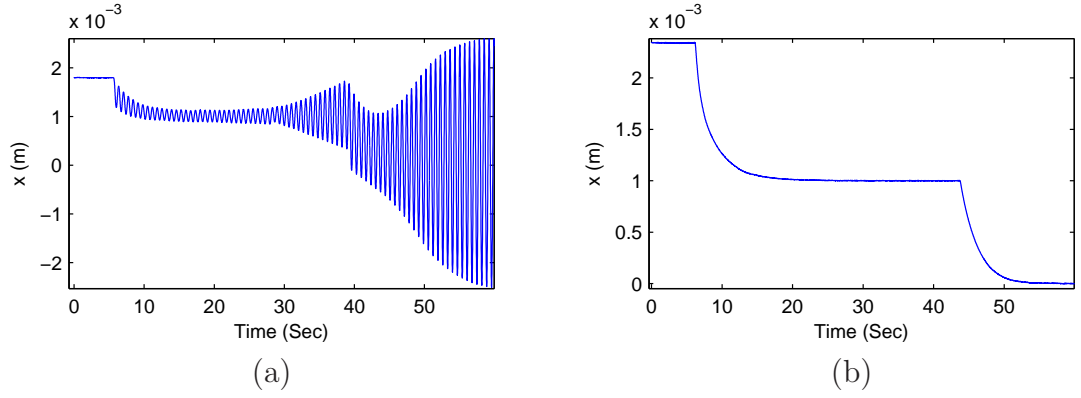
Figure 4.2: The microrobot's motion performance comparison: a) no eddy-current damping effect b) using an Aluminum plate under the workspace to generate the eddy-current.
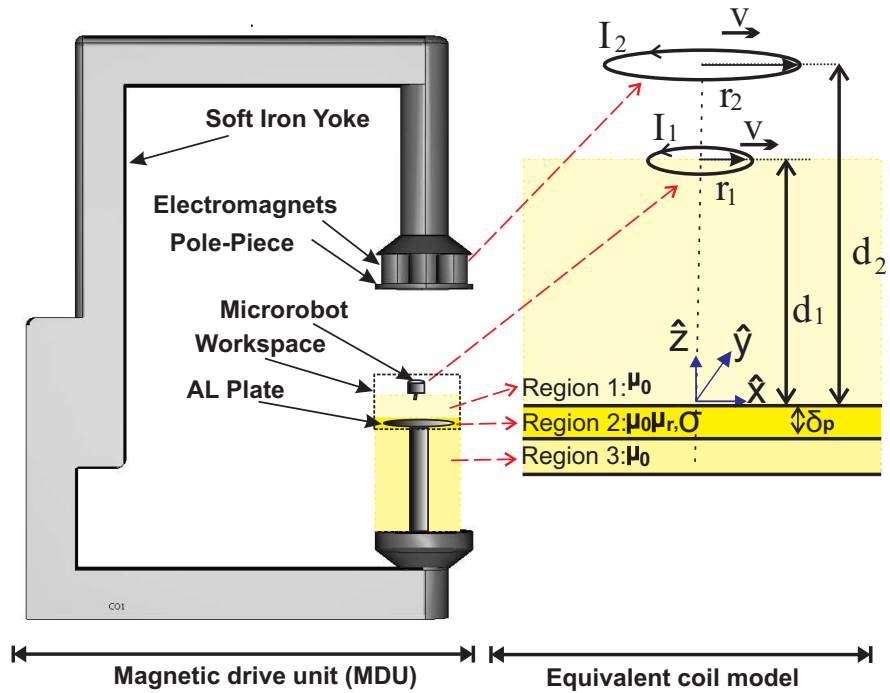


Figure 4.3: Modeling representation of the MDU and the microrobot with loops of current

current $I_2$ and radius $r_2$) and the PM of the microrobot's head (loop no. 1 with the current $I_1$ and radius $r_1$), shown in Fig. 4.3. There is a conductive plate at a distance of $d_2$ from loop number two. The plate is assumed to be of infinite extent in the horizontal plane. It has a thickness of $\delta_p$, relative permeability of $\mu_r$, and conductivity of $\sigma$. Three regions have been used for the modeling as the Region 1: the air gap between the microrobot and the Aluminum plate, Region 2: the Aluminum plate, and Region3: the air gap between the Aluminum plate and the MDU's yoke.

The time-varying currents passing through loops of wire produce changing magnetic field ($\mathbf{B}$). This changing generates the electric field ($\mathbf{E}$) that can be defined by a fundamental equation

$$\nabla \times \mathbf{E} = \frac{\partial \mathbf{B}}{\partial t} \tag{4.1}$$

the generated electric field results in induced eddy-currents in the aluminum plate (region 2). The current density ($\mathbf{J}$) of formed eddy-currents can be represented by the following basic mathematical relation

$$\mathbf{J} = \sigma \mathbf{E} \tag{4.2}$$

where the curl of current density is defined as

$$\nabla \times \mathbf{J} = -\sigma \frac{\partial \mathbf{B}}{\partial t} \tag{4.3}$$

where $\mathbf{E}$ [V/m] is the electric field, $\mathbf{J}$ [A/m ] is the current density, and $\mathbf{B}$ [T] is the magnetic field. Expressing magnetic field as the curl of vector magnetic potential, $\mathbf{B} = \nabla \times \mathbf{A}$, the current density is represented as

$$\mathbf{J} = -\sigma \frac{\partial \mathbf{A}}{\partial t} \tag{4.4}$$

In our modeling, the magnetic field generated by two loops of current can be represented by vector potentials $\mathbf{A}_{Loop1}$ and $\mathbf{A}_{Loop2}$, and the resulted excited field in the aluminum plate can be demonstrated by a vector potential $\mathbf{A}_{Plate}$. The magnetic vector potential for a current of loop with radius $r$ and current $I$ (assumed

clockwise current) is calculated by the real part in [80]

$$\mathbf{A}\left(x', y', z', t\right) = \frac{\mu_0 I r}{4\pi} [\hat{x} \int_{-\infty}^{+\infty} \int_{-\infty}^{+\infty} \frac{\beta}{k^2} J_1[kr] e^{i\alpha x'} \sin\left(\beta y'\right)$$
$$e^{-k|z'-d|} d\alpha d\beta + i\hat{y} \int_{-\infty}^{+\infty} \int_{-\infty}^{+\infty} \frac{\alpha}{k^2} J_1[kr] e^{i\alpha x'} \cos\left(\beta y'\right)$$
$$e^{-k|z'-d|} d\alpha d\beta] \tag{4.5}$$

where $k = \sqrt{\alpha^2 + \beta^2}$, $\alpha$ is the attenuation constant, $\beta$ is the phase constant, $J_1$ is the Bessel function of the first order, and $\epsilon_0$ is the vacuum permittivity. In this relation, the center of the loop is located at a height of $\acute{z} = d$ and at the origin in the $(\acute{x}, \acute{y})$ plane. If the loop has motion in x-direction, in the reference frame of the plate, we can replace $\acute{x} = x - vt$, $\acute{y} = y$, and $\acute{z} = z$, where $v$ is the velocity of loop in x-direction. In our modeling strategy, two loops of current with equal velocity are used and have a similar role in forming the eddy-current induced in the conducting plane. Thus, we can find the current density induced by one loop of current and then combine that density with another loop's effect.

The conducting plate's magnetic vector potential, occurring in response to changes in the position of the loop of current, can be derived by a mathematical approach that originally developed by Maxwell [72] and Reitz [91] and more recently applied by Palmer [80]. In this approach, the continuous motion of loop is discretized to infinite instantaneous steps, and then the effect of continuous motion of the loop can be obtained by using the limit of summation over the infinite steps. Palmer [80] has shown that the instantaneous magnetic vector potential of plate $\mathbf{A}_{plate}$ in the plane of plate $(z = 0)$ at $t = 0$ equal to the magnetic vector potential of the loop at $x = \delta t$ minus at $x = -\delta t$

$$\mathbf{A}_{Plate}\left(x, y\right) = \frac{\mu_0 I r}{4\pi} [\hat{x} \int_{-\infty}^{+\infty} \int_{-\infty}^{+\infty} \frac{\beta}{k^2} J_1[kr] e^{i\alpha x} (e^{i\alpha v \delta t} -$$
$$e^{-i\alpha v \delta t}) \sin\left(\beta y\right) e^{-kd} d\alpha d\beta + i\hat{y} \int_{-\infty}^{+\infty} \int_{-\infty}^{+\infty} \frac{\alpha}{k^2} J_1[kr]$$
$$e^{i\alpha x} \left(e^{i\alpha v \delta t} - e^{-i\alpha v \delta t}\right) \cos\left(\beta y\right) e^{-kd} d\alpha d\beta] \tag{4.6}$$

The vector potential relation of moving a loop of current above a conducting

plate with the thickness $\delta_p$ satisfies the following boundary equation [80; 106]

$$\frac{\partial \left(\mathbf{A}_{Loop} + \mathbf{A}_{Plate}\right)}{\partial t}\Big|_{z=0} = w\frac{\partial \mathbf{A}_{Loop}}{\partial z}\Big|_{z=-\epsilon}^{\epsilon} \tag{4.7}$$

where $w = 2/\sigma\mu_0\delta_p$ has the dimension of the velocity. Based on the initial condition defined by Eq. 4.6 and the boundary condition described by Eq. 4.7, the exact instantaneous solution of $\mathbf{A}_{Plate}$ can be derived for $t > 0$ as [80]

$$\mathbf{A}_{Plate}\left(x, y, z, t\right) = \frac{\mu_0 Ir}{4\pi}[\hat{x}\int_{-\infty}^{+\infty}\int_{-\infty}^{+\infty}\frac{\beta}{k^2}J_1[kr]2i\sin(\alpha v$$
$$\delta t)\sin\left(\beta y\right)e^{i\alpha x}e^{-kwt}e^{-k|w|-b}d\alpha d\beta + i\hat{y}\int_{-\infty}^{+\infty}\int_{-\infty}^{+\infty}$$
$$\frac{\alpha}{k^2}J_1[kr]2i\sin\left(\alpha v\delta t\right)\cos\left(\beta y\right)e^{i\alpha x}e^{-kwt}e^{-k|w|-b}$$
$$d\alpha d\beta] \tag{4.8}$$

This equation defines only one discrete step in the exciting magnetic field. To calculate the eddy-current distribution in the plate, the summation of the discrete steps is calculated followed by the limit over the summation [80]. Therefore, $\mathbf{A}_{Plate}$ can be derived as

$$\mathbf{A}_{Plate}\left(x, y, z, t\right) \stackrel{t=0}{\equiv} \frac{\mu_0 Ir}{4\pi}[\hat{x}\int_{-\infty}^{+\infty}\int_{-\infty}^{+\infty}\frac{\beta}{k^2}J_1[kr]i\alpha v\sin($$
$$\beta y)e^{i\alpha x}e^{-k|z|-b}\frac{kw + i\alpha v}{(\alpha v)^2 + (kw)^2}d\alpha d\beta + i\hat{y}\int_{-\infty}^{+\infty}\int_{-\infty}^{+\infty}$$
$$\frac{\alpha}{k^2}J_1[kr]i\alpha v\cos\left(\beta y\right)e^{i\alpha x}e^{-k|z|-b}\frac{kw + i\alpha v}{(\alpha v)^2 + (kw)^2}d\alpha d\beta] \tag{4.9}$$

In this equation, for $t > 0$, $x$ is replaced by $x - vt$. In the quasi-static condition

$v \ll w$, Eq. 4.9 becomes

$$\mathbf{A}_{Plate}\left(x, y, z, t\right) = \frac{\mu_0 I r}{4\pi}[i\hat{x} \int_{-\infty}^{+\infty} \int_{-\infty}^{+\infty} \frac{\beta}{k^2} J_1[kr] \sin\left(\beta y\right)$$
$$e^{i\alpha(x-vt)} e^{-k|z|-b} \frac{\alpha v}{kw} d\alpha d\beta - \hat{y} \int_{-\infty}^{+\infty} \int_{-\infty}^{+\infty} \frac{\alpha}{k^2} J_1[kr]$$
$$\cos\left(\beta y\right) e^{i\alpha(x-vt)} e^{-k|z|-b} \frac{\alpha v}{kw} d\alpha d\beta] \tag{4.10}$$

In quasi-static condition, $\mathbf{A}_{Plate}$ is $v/w$ smaller than $\mathbf{A}_{Loop}$; therefore, $\mathbf{A}_{Total} = \mathbf{A}_{Plate} + \mathbf{A}_{Loop} \approx \mathbf{A}_{Loop}$. The total current density in the plate is given by Eq. 4.4 at $z = 0$ is

$$\mathbf{J}(x, y) \stackrel{t=0}{=} \frac{\mu_0 I r \sigma \delta_p}{4\pi} v[-\hat{x} \int_{-\infty}^{+\infty} \int_{-\infty}^{+\infty} \frac{\alpha\beta}{k^2} J_1[kr] \sin\left(\alpha x\right)$$
$$\sin\left(\beta y\right) e^{-kd} d\alpha d\beta - \hat{y} \int_{-\infty}^{+\infty} \int_{-\infty}^{+\infty} \frac{\alpha^2}{k^2} J_1[kr] \cos\left(\alpha x\right)$$
$$\cos\left(\beta y\right) e^{-kd} d\alpha d\beta] \tag{4.11}$$

The dimensionality of this integral can be reduced by switching the $\alpha$ and $\beta$ integrals to polar components [80]. Finally, the mathematical current density in plate becomes

$$\mathbf{J}(x, y) \stackrel{t=0}{=} \frac{\mu_0 I r \sigma \delta_p}{4\pi} v[-\hat{x} \frac{2\pi xy}{\rho} \int_0^\infty k J_1[kr] J_2[k\rho] e^{-kd} dk$$
$$-\hat{y} \int_0^\infty k J_1[kr] \left( J_0[k\rho] + \frac{y^2 - x^2}{\rho^2} J_2[k\rho] \right) e^{-kd} dk] \tag{4.12}$$

where $\rho = \sqrt{x^2 + y^2}$. Equation 4.12 represents the current density induced in the plate in response to the horizontal motion of the loop of current (For $t \neq 0$ and motion in x-direction with the velocity of $v$, $x$ is replaced by $x - vt$).

## 4.2.2 Eddy-current Horizontal Damping Force

The eddy-current force on the loop of current will be the result of the magnetic field due to the distribution of the eddy-current in the plate. Based on New-

ton's third law, stating that every action is accompanied by a reaction of equal magnitude but opposite direction, we can calculate the eddy-current force acting on the conductive plate which is equal but opposite in direction to the force applied to the loop of current. The differential force at a point $\mathbf{r}$ on the plate is given by $d\mathbf{F} = \mathbf{J}(\mathbf{r}) \times \mathbf{B}_{Loop}(\mathbf{r})ds$. Thus, the horizontal eddy-current force in x-direction can be calculate by $dF_x = (J_y B_z - J_z B_y)\, ds$. Because the conductive plate is thin, we can assume that $J_z \approx 0$; therefore, the differential horizontal force becomes $dF_x = J_y B_z ds$. Based on our modeling approach, the motion of two loops of current generates the two eddy-currents on the conductive plate where $J_y = J_{yLoop1} + J_{yLoop2}$. Using Eq. 4.12, the y-component of the eddy-current in response to the motion of each loop of current is

$$
J_{yLoop1}(x,y) \overset{t=0}{=} \frac{\mu_0 I_1 r_1 \sigma \delta_p}{4\pi} v \int_0^{+\infty} k J_1[kr_1] e^{-kd_1}
$$
$$
\left( J_0[k\rho] + \frac{y^2 - x^2}{\rho^2} J_2[k\rho] \right) dk \tag{4.13}
$$

$$
J_{yLoop2}(x,y) \overset{t=0}{=} \frac{\mu_0 I_2 r_2 \sigma \delta_p}{4\pi} v \int_0^{+\infty} k J_1[kr_2] e^{-kd_2}
$$
$$
\left( J_0[k\rho] + \frac{y^2 - x^2}{\rho^2} J_2[k\rho] \right) dk \tag{4.14}
$$

To calculate the eddy-current force applied to the conductive plate from the *Loop*1, the z-component of magnetic field of this loop is also required. This z-component in the plane of plate $z = 0$ can be obtained as

$$
B_{zLoop1} \overset{t=0}{=} 0.5 I_1 r_1 \mu_0 \int_0^{+\infty} k J_1[kr_1] J_0[k\rho] e^{-kd_1} dk \tag{4.15}
$$

Using Eqs. 4.13, 4.14, and 4.15, the eddy-current force can now be calculated by $dF_x = J_y B_z ds$. The mathematical relation of current-density in y-direction ($J_y$) for each loop has two components; the first term has polar symmetry, whereas the second term depends on $x$ and $y$. In the process of calculating the total force, the second term becomes zero because the z-component of the magnetic field has

a polar symmetry. Thus, the eddy-current damping force acting on the plate can be derived as

$$
\begin{aligned}
F_x &= \int_0^\infty 2\pi \left( J_{yLoop1} + J_{yLoop2} \right) B_{zLoop1} \rho d\rho = \\
&\quad \frac{\mu_0 v}{2w} \left( I_1 r_1 \right) \left[ I_1 r_1 \int_0^{+\infty} k J_1^2[kr_1] e^{-2kd_1} dk + \right. \\
&\quad \left. I_2 r_2 \int_0^{+\infty} k J_1[kr_1] J_1[kr_2] e^{-k(d_1+d_2)} dk \right]
\end{aligned}
\tag{4.16}
$$

Equation (4.16) enables the numerical calculation of the eddy-current damping force acting on moving $Loop1$. To calculate the eddy-current force applied to the $Loop1$ (Eq. 4.16), we start with $dF_x = J_y B_z ds$ and then use Eqs. 4.13, 4.14, and 4.15 as

$$
\begin{aligned}
F_x &= \int_0^\infty 2\pi \left[ J_{yLoop1} + J_{yLoop2} \right] B_{zLoop1} \rho d\rho = \int_0^\infty 2\pi v \, [ \\
&\quad \frac{\mu_0 I_1 r_1 \sigma \delta_p}{4\pi} \int_0^\infty k J_1[kr_1] \left( J_0[k\rho] + \frac{y^2 - x^2}{\rho^2} J_2[k\rho] \right) e^{-kd_1} \\
&\quad dk + \frac{\mu_0 I_1 r_1 \sigma \delta_p}{4\pi} \int_0^\infty k J_1[kr_2] \left( J_0[k\rho] + J_2[k\rho] \frac{y^2 - x^2}{\rho^2} \right) \\
&\quad e^{-kd_2} dk \, ] \frac{I_1 r_1 \mu_0}{2} \int_0^\infty k J_1[kr_1] J_0[k\rho] e^{-kd_1} dk \rho d\rho
\end{aligned}
\tag{4.17}
$$

expanding this equation and interchanging the integrals results as

$$
F_x = \frac{I_1 r_1 \mu_0^2 \sigma \delta_p v}{4} \left[ I_1 r_1 \left( C_1 + C_2 \right) + I_2 r_2 \left( C_3 + C_4 \right) \right]
\tag{4.18}
$$

where,

$$
\begin{aligned}
C_1 &= \int_0^\infty \int_0^\infty \int_0^\infty k k' J_1[kr_1] J_1[k'r_1] J_0[k\rho] J_0[k'\rho] \\
&\quad e^{-(k+k')d_1} dk dk' \rho d\rho
\end{aligned}
\tag{4.19}
$$

$$C_2 = \int_0^\infty \int_0^\infty \int_0^\infty kk' J_1[kr_1] J_1[k'r_1] J_2[k\rho] J_0[k'\rho] \frac{y^2 - x^2}{\rho^2}$$
$$e^{-(k+k')d_1} dk dk' \rho d\rho \tag{4.20}$$

$$C_3 = \int_0^\infty \int_0^\infty \int_0^\infty kk' J_1[kr_2] J_1[k'r_1] J_0[k\rho] J_0[k'\rho]$$
$$e^{-(kd_2+k'd_1)} dk dk' \rho d\rho \tag{4.21}$$

$$C_4 = \int_0^\infty \int_0^\infty \int_0^\infty kk' J_1[kr_2] J_1[k'r_1] J_2[k\rho] J_0[k'\rho] \frac{y^2 - x^2}{\rho^2}$$
$$e^{-(kd_2+k'd_1)} dk dk' \rho d\rho \tag{4.22}$$

In Eq. 4.17, the term $C_2$ and $C_4$ depend equally on $x$ and $y$, represented by Eqs. 4.20 and 4.22. Thus, when integrating over the entire surface of the aluminum plate, these terms go to zero. Hence, the force model can be represented as

$$F_x = \frac{I_1 r_1 \mu_0^2 \sigma \delta_p \upsilon}{4} [I_1 r_1 C_1 + I_2 r_2 C_3] \tag{4.23}$$

using closure relation for the Bessel function ($\int_0^\infty \rho J_0[k'\rho] J_0[k\rho] d\rho = \frac{1}{k'}\delta(k'-k)$) in Eq. 4.19 and 4.21, the force equation can be represented as

$$F_x = \frac{I_1 r_1 \mu_0^2 \sigma \delta_p \upsilon}{4} \left[ I_1 r_1 \int_0^\infty \int_0^\infty k\delta(k'-k) J_1[kr_1] J_1[k'r_1] \right.$$
$$e^{-(k+k')d_1} dk dk' + I_2 r_2 \int_0^\infty \int_0^\infty k\delta(k'-k) J_1[kr_2]$$
$$\left. J_1[k'r_1] e^{-(kd_2+k'd_1)} dk dk' \right] \tag{4.24}$$

using the property of Dirac delta function $\int f(t)\delta(t-T) = f(T)$, the force equation can be defined by

$$F_x = \frac{I_1 r_1 \mu_0^2 \sigma \delta_p \upsilon}{4} \left[ I_1 r_1 \int_0^\infty k J_1^2[kr_1] e^{-2kd_1} dk + I_2 r_2 \int_0^\infty k \right.$$
$$\left. J_1[kr_1] J_1[kr_2] e^{-k(d_2+d_1)} dk \right] \tag{4.25}$$

replacing $w = 2/\sigma\mu_0\delta_p$ in this equation results in the force equation as

$$F_x = \frac{\mu_0 v}{2w}(I_1 r_1)\left[I_1 r_1 \int_0^\infty kJ_1^2[kr_1]e^{-2kd_1}dk + I_2 r_2 \int_0^\infty k \right.$$
$$\left. J_1[kr_1]J_1[kr_2]e^{-k(d_1+d_2)}dk \right] \tag{4.26}$$

Although the integral upper limit is infinity, the force equation converges by the Bessel function, $J_1$. The eddy-current damping coefficient in x-direction can then be defined as

$$c_{e,x} = \frac{F_x}{v} = \frac{\mu_0}{2w}(I_1 r_1)[I_1 r_1 \int_0^{+\infty} kJ_1^2[kr_1]e^{-2kd_1}dk +$$
$$I_2 r_2 \int_0^{+\infty} kJ_1[kr_1]J_1[kr_2]e^{-k(d_1+d_2)}dk] \tag{4.27}$$

## 4.3   The Analogy of Eddy-current Force

Eddy-currents are formed by a changing magnetic field. There are two sources of the changes: 1) the magnetic field of the microrobot's head, which is a permanent magnet. 2) the magnetic field of electromagnets. This section introduces an analogy between the sources of magnetic field changes in the MUMS and coil model described in the previous section. Thus, the change of the flux penetrating into the conductive plate can provide an analogical approach to determine the parameters of the coil model based on the MUMS structure [35]. The magnetic field of the permanent magnet can be written as

$$\mathbf{B} = \frac{\mu_0}{4\pi}p_0\left(\widehat{r}\frac{2\cos\theta}{r^3} + \widehat{\theta}\frac{\sin\theta}{r^3}\right) \tag{4.28}$$

where $p_0$ is the dipole moment of the magnet and $\theta$ is the angle from the central axis (Fig. 4.4). The magnetic flux going through the plate is equal to the flux going through the outer surface of the semi-sphere as shown in Fig. 4.4. Then
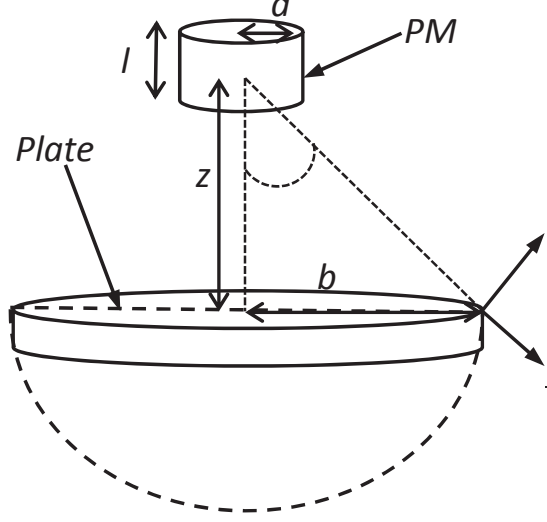
Figure 4.4: Permanent magnet (PM) above a circular plate [35].

passing flux can be derived as

$$\phi_{pm} = \int \mathbf{B} \cdot d\mathbf{s} = \int_{sphere} \mathbf{B} \cdot \hat{r} ds = \int_0^{\cos^{-1}\frac{z}{\sqrt{z^2+b^2}}} \int_0^{2\pi}$$
$$B_r r^2 \sin\theta d\phi d\theta = \frac{\mu_0}{2} p_0 \frac{b^2}{(b^2+z^2)^{3/2}} \tag{4.29}$$

where the subscript $pm$ denotes that the flux belongs to the permanent magnet as the head of the microrobot. In an analogy between the coil (loop of current) and the permanent magnet, the coil ($Loop1$) is placed above the circular plate. The flux passing through the plate can be found in a similar way

$$\phi_{coil} = \frac{\mu_0}{2} I_1 \pi r_1^2 \frac{b^2}{(b^2+d_1^2)^{3/2}} \tag{4.30}$$

In the previous section, the eddy force is derived for a loop of current with three parameters $I_1$, $r_1$, and $d_1$. Equating the magnetic flux of the coil and permanent magnet, the equivalent loop of current can then be found. The magnetic flux of electromagnets is considerably influenced by the pole-piece and the soft iron yoke, shown in Fig. 4.1. Therefore, the magnetic field formed by the electromagnets

cannot be determined analytically. Alternatively, an experimental method has been followed. The magnetic flux of the MDU is measured by a gaussmeter probe. The probe was moved inside the workspace by a high precision robot while the z-component of the magnetic field was recorded. Measurements demonstrated that the magnetic field [Tesla] in that area can be approximated as [74]

$$B_{z,em} = \frac{c_0}{|z|}I \tag{4.31}$$

where $c_0$ is a magnetic field parameter for the MDU, determined by experimental measurements, and the $em$ subscript denotes the electromagnets. The parameters $z$ and $I$ are the vertical distance from the pole-piece, and the summation of currents in electromagnets, respectively. Thus, the flux passing through the plate can be calculated as

$$\phi_{em} = \int_0^b 2\pi B_{z,em} \rho d\rho = \frac{\pi c_0 b^2}{|z|}I \tag{4.32}$$

Equating Eqs. 4.30 and 4.32, equivalent coils for the electromagnets can be found. The parameters of two equivalent coils that generate the same flux change are determined, so the induced eddy-current damping can be calculated numerically using Eq. 4.16.

Implementing this method, the eddy-current damping force formed by the electromagnets and the microrobot's head was calculated as a function of the microrobot's position, as shown in Fig. 4.5. This figure presents the horizontal eddy-current damping coefficient that results from placing a 50 mm radius, 5 mm thick aluminum circular plate at a 100 mm distance from the pole-piece [at the working frequency of 1000 Hz, the skin depth can be calculated as 2.95 mm, therefore, a 5 mm thickness Aluminum plate has been used in the experiment. Thicker plate has no further improvement on the damping.]. The velocity $w$ equals 9 m/s; the microrobot velocity is much smaller than this velocity. Thus, the assumption of motion in quasi-static condition is very reasonable for this application. As shown in Fig. 4.5, the total eddy force was the summation of these two parameters: 1) the eddy-current induced in the plate in response to the electromagnets' change of current, and 2) the eddy-current induced in the
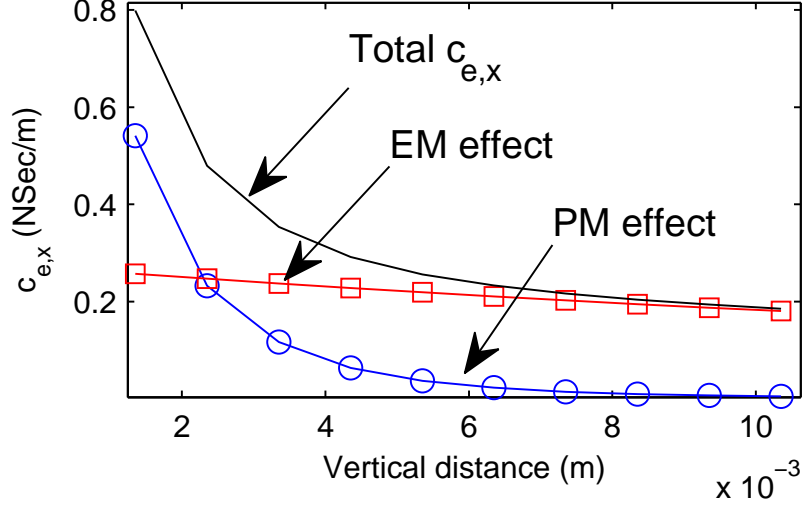
Figure 4.5: Eddy-current damping coefficient formed by the microrobot's head and electromagnets. The plate is located at $d_2 = 0.1$ m from the pole-piece

plate in response to the motion of the microrobot. As expected, the eddy force increases significantly when the microrobot moves close to the plate.

## 4.4 Experimental Verification of Eddy-current Damping Force Model

In order to validate the eddy force found by Eq. 4.16, we have investigated the horizontal motion of the microrobot. The dynamical model of the microrobot can be defined by the application of Newton's second law as

$$m\ddot{x} = P\frac{\partial B_z}{\partial x} + c_{e,x}\dot{x} + f_{env,x} \qquad (4.33)$$

$$m\ddot{y} = P\frac{\partial B_z}{\partial y} + c_{e,y}\dot{y} + f_{env,y} \qquad (4.34)$$

$$m\ddot{z} = P\frac{\partial B_z}{\partial z} + c_{e,z}\dot{z} - mg + f_{env,z} \qquad (4.35)$$

where $g$ is the acceleration of gravity, $m$ is the mass of the microrobot, $P$ is the magnetic dipole moment of the microrobot's head, $c_e$ is the eddy-current damping factor, and $f_{env}$ is environmental forces. The environmental forces are negligible; meanwhile the microrobot motion takes place in free motion and a low viscous environment ($f_{env} \approx 0$). Hence, the magnetic gradient in z-direction is a significant factor in the microrobot's motion control. We previously reported the non-linear mathematical relations for magnetic gradients in [73; 74], which were obtained by extensive numerical analysis coupled with the experimental measurements.

Since the eddy-current damping force is not a static force, the dynamical system identification is required. For dynamical response analyses in the horizontal plane, the nonlinear model represented by Eqs. 4.33 and 4.34 is linearized at the center of the working space of the microrobot as

$$m\ddot{x} + c_{e,x}\dot{x} - 3x\left(\alpha_x + \alpha_y\right)I_0 = \frac{-\sqrt{3}}{2}\beta_y \underbrace{\left(i_1 - i_3 + i_6 - i_4\right)}_{v_x} \qquad (4.36)$$

$$m\ddot{y} + c_{e,y}\dot{y} - 3y\left(\alpha_x + \alpha_y\right)I_0 = \frac{1}{2}\beta_y \underbrace{\left(i_1 + 2i_2 + i_3 - i_4 - 2i_5 - i_6\right)}_{v_y} \quad (4.37)$$

where $i_j$ is the perturbed current for the $j^{th}$ electromagnet ($j = 1, \cdots, 6$). The virtual commands for motion in the x-direction and y-direction are defined as $v_x$ and $v_y$, respectively [74]. The current $I_0$ is the uniform current of electromagnets while the microrobot is levitated at the center of the working space. Therefore, the input-output transfer function in the Laplace domain for horizontal motion, Eq. 4.36 and 4.37, can then be presented as

$$\frac{X\left(s\right)}{V_x\left(s\right)} = \frac{-\sqrt{3}/2\beta_y}{ms^2 + c_{e,x}s - 3\left(\alpha_x + \alpha_y\right)I_0} \qquad (4.38)$$

$$\frac{Y\left(s\right)}{V_y\left(s\right)} = \frac{1/2\beta_y}{ms^2 + c_{e,y}s - 3\left(\alpha_x + \alpha_y\right)I_0} \qquad (4.39)$$

Thus, the horizontal eddy-current damping parameters ($c_e$) can then be estimated

by an experimental step response in the x-direction or y-direction. Based on the characteristic of the second order system, the eddy-current damping coefficients $c_{e,x}$ and $c_{e,y}$ can be determined by using input-output system identification of the experimental measurements.

To identify the effect of the eddy-current damping formed by the aluminum plate, we have conducted experiments capturing the microrobot motions at various distances from the aluminum plate. The circular aluminum plate, with radius 50 mm and thickness of 5 mm, was located 100 mm below the MDU's pole-piece. Figure 4.6 demonstrates the horizontal response of the microrobot at several vertical distances from the aluminum plate. As shown in this figure, increasing the vertical distance of the microrobot from the aluminum plate raises the horizontal vibration of the microrobot inside the working space. It was observed that the produced eddy-current damping suppresses the horizontal vibration caused by the inherent underdamped nature of the system. Moreover, this damping effect guarantees stable stepwise motions.

To verify quantitatively the effect of the eddy-current damping, our experimental measurements were coupled with the linear system identification. Since the linear structure of the system model is known from Eqs. 4.38 and 4.39, we employed process model of *Matlab*'s system identification toolbox [69] to determine the eddy-current damping coefficient based on the off-line identification analyses. (The process model system identification is an iterative process that uses nonlinear least-squares algorithm that minimizes the weighted sum of the squares of the errors of the estimated data.) For comparing the identified model performance with real dynamics, Figure 4.7 illustrates the performance of both the identified process model and the experimental measurements for two different case studies. As shown in this figure, the identified model can predict the system dynamics with high accuracy. In this case study, the eddy-current damping coefficient, $c_{e,x}$, has been identified as 0.575 NSec/m or 0.171 NSec/m, depending on whether the vertical distances of the microrobot from the aluminum plate is 4.3 mm or 9.3 mm, respectively. Figure 4.8 demonstrates how eddy-current damping coefficients vary in response to changes in the vertical distance of the microrobot from the aluminum plate. As shown in this figure, the damping coefficient is intensely proportional to the inverse of the microrobot's distance from the aluminum plate.
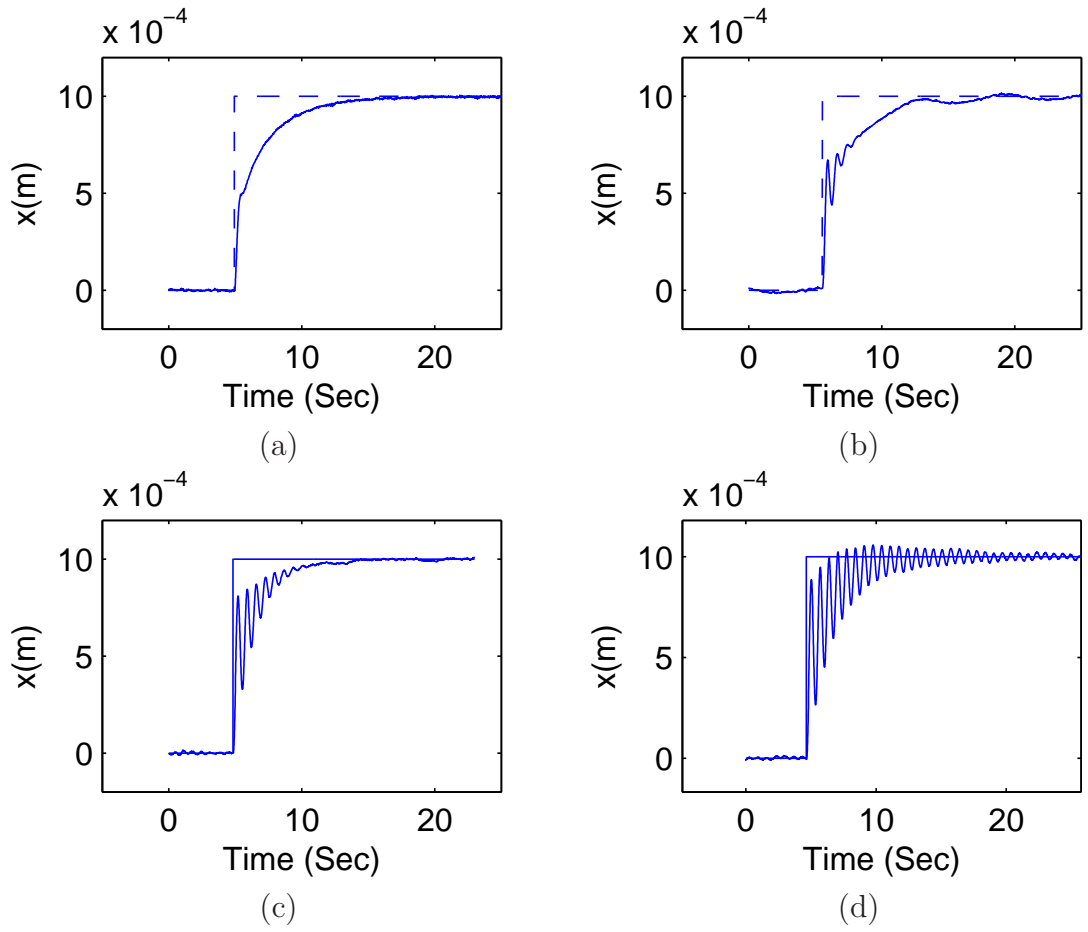
Figure 4.6: Dynamical responses in horizontal motion (x-direction) vs. the vertical distance ($d_1$) of the microrobot from the the aluminum plate, (a) $d_1 = 4.3mm$, (b) $d_1 = 7.3mm$, (c) $d_1 = 9.3mm$, and (d) $d_1 = 10.3mm$

Thus, the inverse of the damping coefficient versus the distance of the microrobot from the aluminum plate has been used to obtain a linear mathematical relation, shown in Fig. 4.9. The linearly fitted mathematical relation is defined by

$$\frac{1}{c_{e,x}} = 567.73d_1 + 0.62826 \Rightarrow c_{e,x} = \frac{1}{567.73d_1 + 0.62826} \tag{4.40}$$

Figure 4.10 demonstrates the comparison of the eddy-current damping coefficient obtained by the theoretical method (using Eq. 4.27) and experimental measurements (using Eq. 4.40). This figure shows the high consistency between the proposed theoretical relation and the experimental measurements in determining the horizontal eddy-current damping coefficient.

## 4.5   Eddy-Current Damping Torque

In the horizontal motion, the eddy-current damping force is larger at the bottom of the levitated permanent magnet that can generates a torque for the permanent magnet; however, the magnetic torque applied to the permanent magnet to make it parallel to magnetic field direction is considerably larger than the Eddy-current torque. The following steps demonstrate the order-of-magnitude of magnetic torque applied to the permanent magnet in comparison with the Eddy-current damping torque.

The applied magnetic torque $\tau$ can be calculated as $\tau = \mathbf{P} \times \mathbf{B}$, where $\mathbf{P}$ and $\mathbf{B}$ are magnetic dipole moment and magnetic field vector produced by the MDU, respectively. In this study, the magnetic dipole moment vector has z-component, $\mathbf{P} = [0\ 0\ P]$. The magnitude of magnetic dipole moment equals to $B_r v / \mu_0$, where $B_r$ is the residual flux density of permanent magnet, 0 is the vacuum permeability,and $v$ is the volume of the permanent magnet. The magnetic field in the working space of our system is mainly in the z-direction. Thus, we can realistically assume $B = B_z$. Measurements demonstrated that the magnetic field [Tesla] in that area can be approximated as [33]

$$B_{z,em} = \frac{c_0}{|z|}I \tag{4.41}$$

x(m) vs Time (Sec)

(a)

(b)
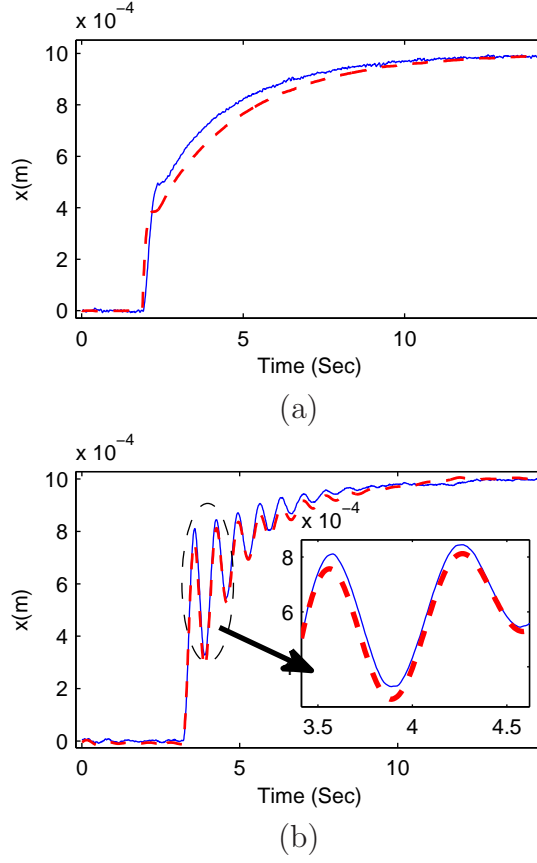
Figure 4.7: The performance of identified model (−−) Vs. the experimental measurements (−) in the horizontal motion (x-direction); the vertical distance ($d_1$) of the microrobot from the the aluminum plate is : (a) $d_1 = 4.3mm$ and (b) $d_1 = 9.3mm$
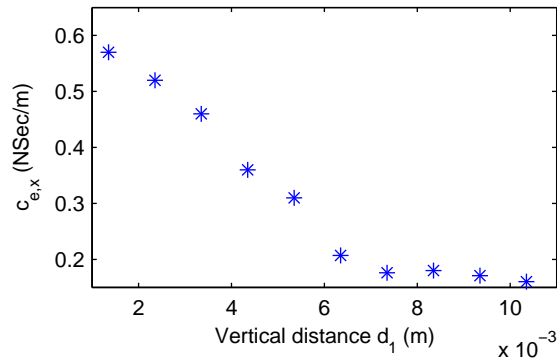


Figure 4.8: Change of eddy-current damping coefficient in x-direction $c_{e,x}$ versus the vertical distance of the microrobot form the aluminum plate
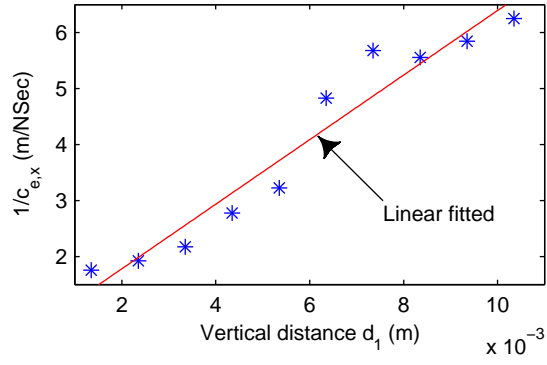
Figure 4.9: Linear curve fitting of the inverse damping coefficient versus the vertical distance of the microrobot form the aluminum plate
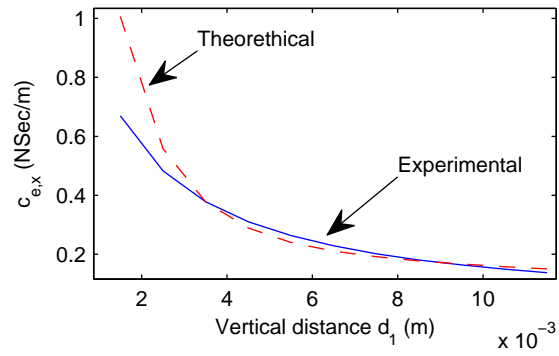


Figure 4.10: Comparing the analytical horizontal eddy-current damping coefficient with the experimental measurements

where $c_0$ is a magnetic field parameter for the MDU, determined by experimental measurements, and the em subscript denotes the electromagnets. The parameters $z$ and $I$ are the vertical distance from the pole-piece, and the summation of currents in electromagnets, respectively. The permanent magnet is levitate at the distance $z_0$ form the pole-piece, so the magnetic force in z-direction can be calculated as

$$F_z = P\frac{\partial B_z}{\partial z} = \frac{c_0 P}{|z|^2}I \tag{4.42}$$

In the vertical position of the $z_0$ , the magnetic force in z-direction equals to the weight of the permanent magnet, so the current summation $I_{lev}$ for the levitation can be calculated as

$$F_z = mg \Rightarrow \frac{c_0 P}{|z|^2}I_{lev} = mg \Rightarrow I_{lev} = \frac{mg\,|z|^2}{c_0 P} \tag{4.43}$$

Thus, the magnetic torque applied to the levitated permanent magnet can be estimated as

$$\tau = \mathbf{P} \times \mathbf{B} = P\frac{c_0}{|z|}I_{lev} = P\frac{c_0}{|z|}\frac{mg\,|z|^2}{c_0 P} = mg\,|z| \tag{4.44}$$

Thus, the magnetic torque is linearly proportion to the weight of the microrobot and the distance from the pole-piece. In our experimental measurement the permanent magnet has the mass of the 10 gr and the maximum distance from the pole-piece is 10 cm. Therefore the estimate magnetic torque can be calculated as $\tau = 0.01$ N.m. However, the maximum eddy-current torque can be calculated, if we assume that all the applied eddy-current damping force applied to the bottom of the permanent magnet as

$$\tau_{eddy} = c_{e,x}\dot{x}\frac{l}{2} \tag{4.45}$$

where $\dot{x}$ and $l$ are the velocity and length of permanent magnet, respectively. Assuming the maximum velocity of 1 mm/sec, the damping coefficient in the range of $0.1 \leq c_{e,x} \leq 0.6$, and the length of 10 mm for the permanent magnet, the maximum eddy-current damping torque can be calculated as $0.5 \times 10^6 \leq$

$\tau_{eddy} \le 3 \times 10^6$. This maximum damping torque range is considerably smaller, roughly 3000 times, than the torque applied by the magnetic field which is in the order of 0.01 N.m. Therefore, the eddy torque effect is negligible and the levitated magnet stays vertically due to existence of large magnetic torque of 0.01 N.m; the magnetic field produced by the MDU passively controls the orientation of the microrobot.

## 4.6   Summary

In this chapter, a horizontal eddy-current damping mechanism and its mathematical modeling have been developed to improve the precision and stability of a magnetic untethered microrobotic system (MUMS). In this method, a circular aluminum plate was placed below the working space of the MUMS's microrobot. In order to calculate eddy-current force, a method based on a coil (loop of current) representation model was employed. In this simplified model, the magnetic vector potential of the model was derived for any point in space. Eddy-current density due to the change of magnetic field in the circular plate was calculated. For the described MUMS, representing the change in magnetic field with equivalent coils, the eddy-current force applied to the aluminum plate was obtained. Since the aluminum plate's position is fixed, equal but opposite in direction force is applied to the microrobot. The experimental measurements coupled with process model system identification validated the proposed analytical relation for the horizontal eddy-current damping. The experiments also verified that placing a conductive plate underneath the the microrobot, effectively dissipated the excessive portion of levitation force that caused vibrations.

# Chapter 5

# Position determination and Force Sensing Using Flux Measurement[1]

This Chapter is organized to firstly present a novel technique for the microrobot's position determination in non-transparent environments and then introduce an innovative approach for sensing the environmental micro-domain force for haptic application of the platform. Chapter two has already reported that the MUMS should be equipped with high accuracy laser sensors for the position determination of the microrobot in the workspace. However, the laser positioning techniques can be used only in highly transparent environments. The first part of this chapter seeks to address microrobot position estimation in non-transparent environments. A novel technique based on real-time magnetic flux measurement has been proposed for position estimation of the microrobot in the case of the laser beam blockage. A combination of Hall-effect sensors is employed in the structure of the magnetic drive unit to find the microrobot's position using the produced magnetic flux.

---

To preserve a high feeling of a micro-domain environment for a human operator, the applied force/torque from the environment to the microrobot are required to be directly measured by specific sensors. Many methods for measuring force from the micro-Newton to milli-Newton range have been developed, such as atomic force microscopes [10], micro-scales, piezoresistive cantilevers [25; 30; 82; 83; 84; 122] and capacitive force sensors [48]. These force measurement systems have been employed in the research field of microsystem and microassembely, as well as biomedical/biological research. However, attaching such measurement systems to the MHMP's microrobot is impracticable due to: 1) micro-scaled sensors is needed to be integrated with the microrobot for measuring forces; thus, the overall size and weight of the microrobot is largely increased, 2) to maintain free levitation, the microrobot needs to be equipped with an onboard wireless communication device to transfer the sensors' measurements, 3) the micro-sized force sensors are expensive and very sensitive to the physical parameters of an environment. The second part of this chapter has introduced a novel micro-domain force estimation method eliminating the need of mounting a force sensor to the microrobot. The non-contact force estimation is carried out based on the measured magnetic flux and real-position of the microrobot, those are determined by Hall-effect sensors and laser sensors, respectively.

## 5.1 Horizontal Position Estimation and Control By Measuring Magnetic Flux

### 5.1.1 Principle of Microrobot Position Estimation

*Nakamura* [76] has used numerical analyses coupled with experiments to investigate the $B_{max}$ position control in a 2-D case. Figure 5.1 demonstrates schematically the magnetic field produced by two electromagnets connected with a polepiece. As shown in this figure, the combination of pole-piece and electromagnets configures the vertical magnetic field in such a way that only one $B_{max}$ appears in the horizontal plane below the pole-piece. In a 2-D demonstration, the position of $B_{max}$ can be controlled by tunning the electromagnets' produced magnetic fluxes
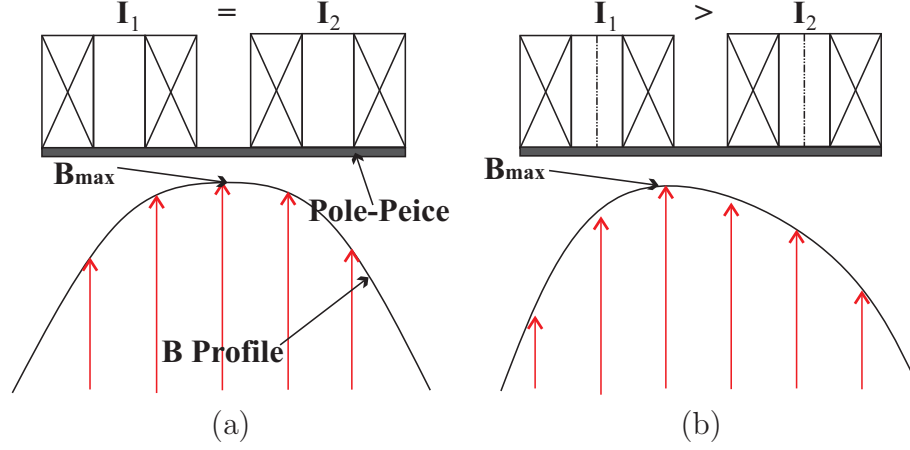
Figure 5.1: Demonstration of the qualitative $B_{max}$ position produced by two electromagnets connected by a pole-piece,(a) equally loaded,(b)unequally loaded

[changing the electromagnets' coil current ($I$) alters its produced magnetic flux]. If the relation is reversed, the $B_{max}$ horizontal position can be estimated by measuring the flux difference generated by two electromagnets. This reverse concept will be used in this study as the backbone of determining the microrobot position without laser sensors measurements. A combination of Hall-effect sensors can be installed on the MDU's structure to estimate the $B_{max}$ position.

The installation position of Hall-effect sensors is key aspect to accomplish a high accuracy $B_{max}$ position determination. Since the generated magnetic flux of electromagnets penetrates to the MMS's workspace through the pole-piece, Hall-sensor can be attached to the pole-piece to measure the produced magnetic flux. In this study, one-axis $B_{max}$ position determination has been carried out as a "proof-of-concept" for our contribution.

### 5.1.2 Installation Position of Hall-effect Sensors

In this section, an effective arrangement of Hall-effect sensors is investigated for a single-axis $B_{max}$ position determination. In order to estimate the $B_{max}$ position in one axis, it was thought that at least two hall sensors should be installed on the specified axis on the pole-piece. The difference of magnetic flux measured by these two sensors can be mapped to the $B_{max}$ position. Figure 5.2 demonstrates the installation position of two Hall-effect sensors on the y-axis.

The installation positions of Hall-effect sensors relative to the center of the pole-piece play an important factor in the accuracy of $B_{max}$ position estimation. Thus, these sensors are attached to an aluminum measuring stick to find effective arrangement of Hall-effect sensors by experimental sensitivity analyses. An experimental measurement setup has been developed to investigate the effective mathematical relation between Hall-effect sensor's voltage output and $B_{max}$ position; Fig. 5.4 presents the measurement setup schematically. In this setup, the MMS has been used to manipulate the microrobot along the y-axis; meanwhile the magnetic flux is measured by the Hall-effect sensors and is recorded on the dSPACE controller.

To determine the effective position of Hall-effect sensors, three configurations-"inner", "mid", and "outer"-have been experimentally investigated, Fig. 5.3 shows these configurations schematically. The distance between the two Hall-effect sensors on the y-axis in the "inner", "mid", and "outer" configurations is 40 mm, 88 mm, and 120 mm, respectively. Figure 5.5 presents the measured flux differential versus the microrobot's position on the y-direction. Since determining the instantaneous position of the $B_{max}$ location requires a real-time magnetic field scanning, the steady-state position of the microrobot is assumed as a reasonable approximation of the $B_{max}$ location. The steady-state condition of the microrobot is used, because in non-steady condition, there is a discrepancy between the $B_{max}$ location and the microrobot position. The relation between flux differential and the $B_{max}$ location can be used for instantaneous conditions, since the dynamic magnetic field is faster than the microrobot.

Figure 5.5 also shows the best fitted curves to experimental measurements for determining the optimal configuration of the Hall-effect sensors. In "inner" and "outer" arrangement of the Hall-effect sensors, a linear function can be fitted; however, a third-order polynomial defines a good approximation for "mid" configuration. The fitted mathematical equations can be defined as,

- Inner Configuration:

$$v_d = 23.97y - 0.1370 \tag{5.1}$$

- Mid Configuration:

Table 5.1: The comparison of estimation error factor (EEF) for three arrangements

| Configuration of Hall-effect Sensors | EEF [m] |
| --- | --- |
| Inner | 0.002003 |
| Mid | 0.002147 |
| Outer | 0.002700 |

$$v_d = -498495.78y^3 + 1975.53y^2 + 129.38y - 0.38 \qquad (5.2)$$

- Outer Configuration:

$$v_d = 34.46y - 0.06 \qquad (5.3)$$

where $v_d$ is the flux differential in voltage measured by the Hall-effect sensors (Two hall sensors' outputs have been amplified via operational amplifier). The y-position of the microrobot measured by laser sensor is denoted by $y$ in SI units. To select the arrangement of Hall-effect sensors for high accuracy position estimation, the norm of the residual (the difference between the experimental value and the value predicted by the correlation equation) has been calculated as an estimation error factor (EEF); this factor is presented in Table 5.1 for each arrangement. The accuracy of position estimation is proportional to the inverse of the EEF. Based on the calculated EEF in Table 5.1, the "inner" configuration provides higher position accuracy. Thus, $B_{max}$ position estimation with "inner" configuration, using Eq. 5.1, can finally be determined by

$$y = 0.004492v_d + 0.0056843 \qquad (5.4)$$

In this study, the "Inner" configuration has been implemented on the real-time controller to provide position feedback for the control system.
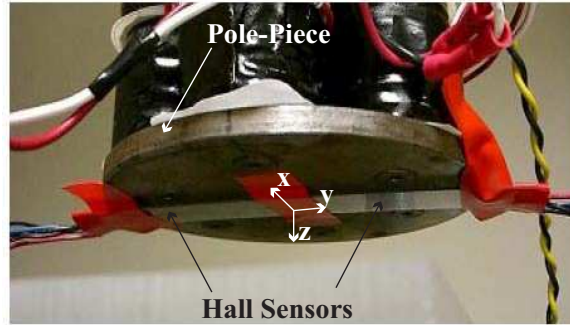
Figure 5.2: The Hall-effect sensors are attached to a measurement stick and installed on the bottom of pole-piece
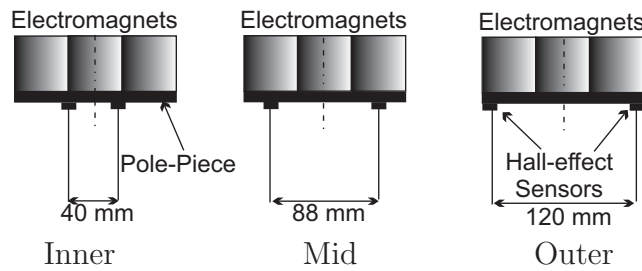


Figure 5.3: Three arrangements of Hall-effect sensors used in experimental measurements
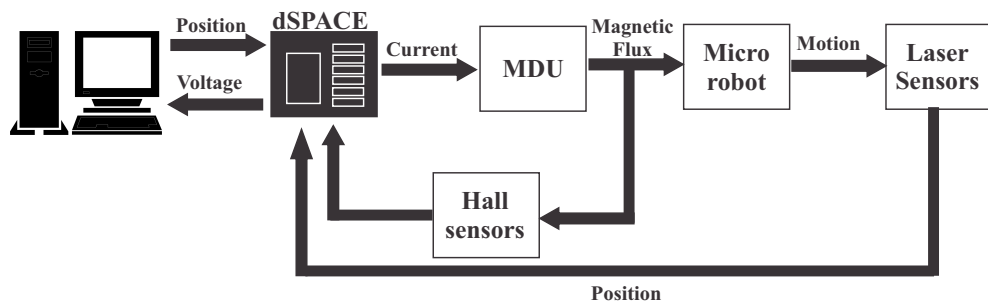


Figure 5.4: Schematic diagram of experimental setup to investigate Hall-effect sensors position estimation method
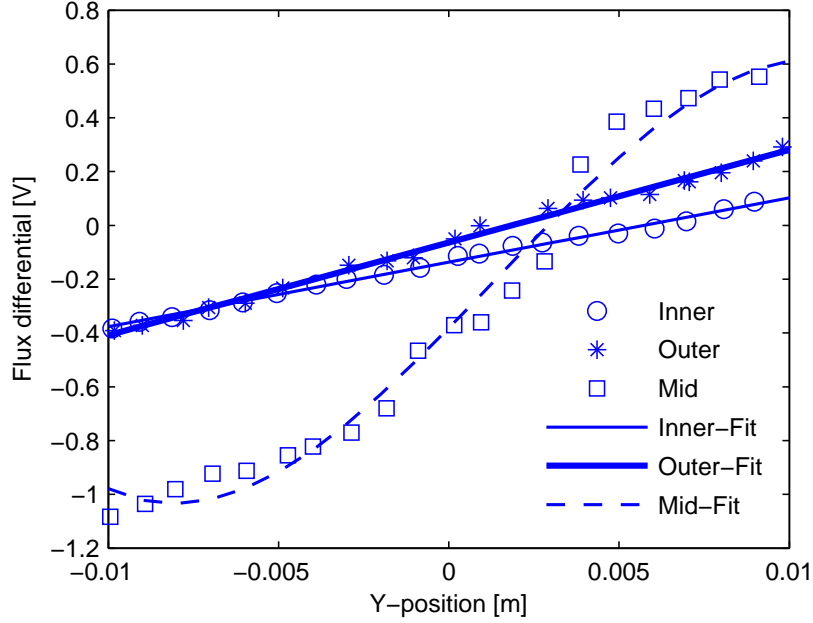
Figure 5.5: Hall sensor arrangement investigation, position-voltage relation

### 5.1.3 Position Control Using Hall-effect Sensors

The proposed method for the position estimation has been validated by the experimental measurements. The laser sensor in the y-direction has been replaced with the Hall-effect sensors in the "Inner" configuration. The filtered differential voltage of the Hall-effect sensors are fedback to the real-time controller. The controller computes the $B_{max}$ position using Eq. 5.4. Figure 5.6 demonstrates the schematic diagram of the proposed control system. The control system design is not the main contribution of this study; thus, we have used the previously developed control system with our new position estimation method.

The performance of the proposed estimation method in y-axis controller has been presented in Fig. 5.7. As shown in this figure, the Hall-effect sensors provide accurate position estimation when the microrobot is close to the center of the working envelope. Increasing the horizontal distance from the center of the workspace reduces the accuracy of both position estimation and position tracking; Fig. 5.8 demonstrates the root-mean-square (RMS) of estimated position error at a steady-state condition in y-axis motions. This figure demonstrates that

96
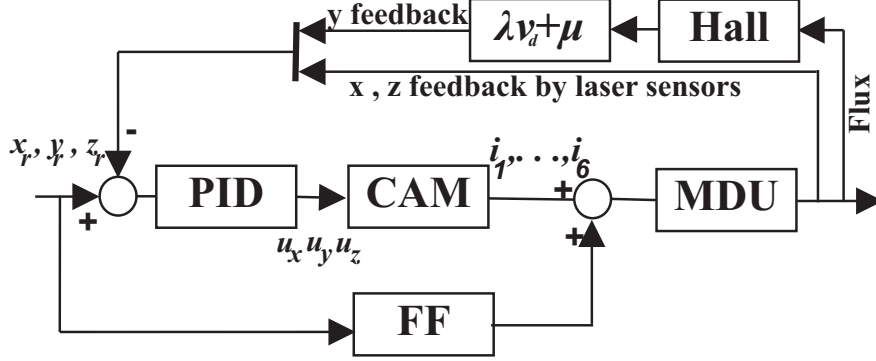
Figure 5.6: Schematic diagram of the MUMS using Hall-effect sensor for position estimation in y-axis. The $\lambda$ and $\mu$ are coefficients of Eq. 5.4

for the horizontal distance less than 7 mm the RMS of position error is smaller than 0.3 mm. However, by selecting a more accurate mathematical function for the position estimation relation, Eq. 5.4, more accurate position control can be achieved. This type of position control can be operated in a coupled way with high precision laser sensor while there is a laser beam blockage.

## 5.2 Environmental Force Sensing

### 5.2.1 Principle of Force Measurement

Chapter 3 discussed the principle of microrobot's free levitation and the mathematical force model experienced by the microrobot inside the magnetic field produced by the MDU. In a condition that the microrobot is in contact with an environment that applies force ($f_e$) to the microrobot, the microrobot is not stabilized at the $B_{max}$ location. The magnetic field produced by the MDU exerts force to the microrobot to move it toward the $B_{max}$ location, meanwhile the environment applies equal and opposite direction force ($f_e$) to the microrobot. Thus, the microrobot becomes stable at a location that the magnetic field gradient is not equal to zero in the horizontal motion plane, shown schematically in Fig. 5.9 [This study focuses on the investigation of environmental force measurement in y-direction; however, the motion study in x- and z-direction can be performed in the similar way, the reference axis is shown in Fig. 2.3]. In the steady state con-

97
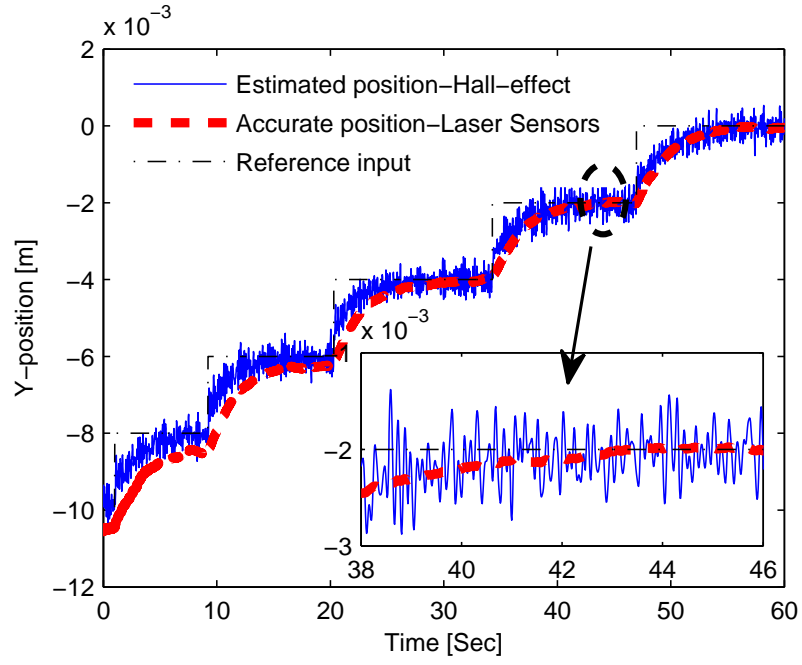
Figure 5.7: y-axis motion control performance using hall sensor position estimation
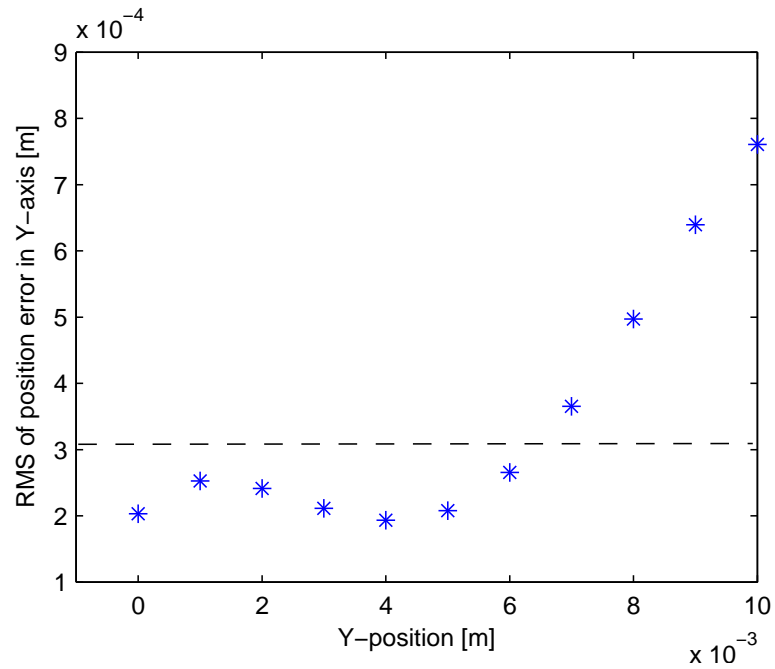


Figure 5.8: Variation of position accuracy Vs horizontal distance from the center of the workspace
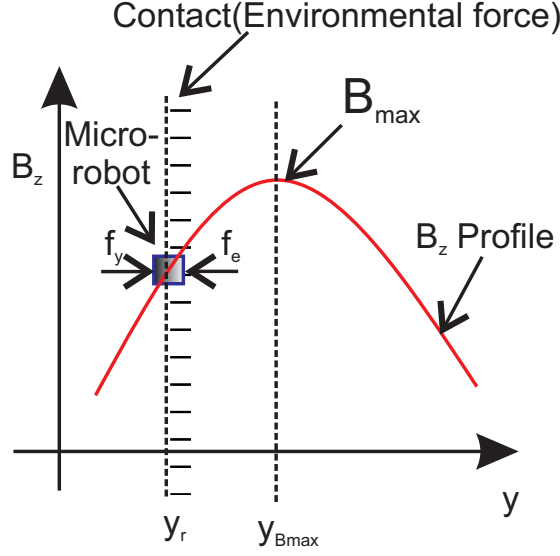
Figure 5.9: The schematic representation of the force estimation concept

dition, the magnetic force applies to the microrobot equals to the environmental force that can be estimated by using Eq. 3.10 as

$$f_y = y_r/4 \left(3\alpha_x + \alpha_y\right)\left(I_1 + I_3 + I_4 + I_6\right) + y_r\alpha_y \left(I_2 + I_5\right) - \sqrt{3}/4x_r \left(\alpha_x - \alpha_y\right)$$
$$\left(I_1 - I_3 + I_4 - I_6\right) - 1/2\beta_y \left(I_1 + 2I_2 + I_3 - I_4 - 2I_5 - I_6\right) = f_e \quad (5.5)$$

where $x_r$ and $y_r$ determine the position of the microrobot in the horizontal plane relative to the reference coordinate defined in Fig. 2.3. The coefficients $[\alpha_x \ \alpha_y \ \beta_y]$ are determine by multiplication of microrobot's head magnetization, $M$, and the average magnetic field coefficients $\left[\overline{\alpha_x} \ \overline{\alpha_y} \ \overline{\beta_y}\right]$ introduced in Section 3.2.1. Since, it is a single-axis force estimation, y-direction, we assumed the $x_r = 0$ and keep the vertical position of the microrobot $z_r$ equals to $z_0$. The microrobot real position can be represents as $y_r = y_{Bmax} + \Delta y$, Fig. 5.9. This relation can then be replaced in Eq. 5.5 as

$$f_y = (y_{Bmax} + \Delta y)/4 \left(3\alpha_x + \alpha_y\right)\left(I_1 + I_3 + I_4 + I_6\right) + (y_{Bmax} + \Delta y)\alpha_y \left(I_2 + I_5\right)$$
$$-1/2\beta_y \left(I_1 + 2I_2 + I_3 - I_4 - 2I_5 - I_6\right) = f_e \quad (5.6)$$

re-arranging this equation as

$$f_y{=}f_e = \overbrace{[\Delta y/4\left(3\alpha_x + \alpha_y\right)\left(I_1 + I_3 + I_4 + I_6\right) + \Delta y\alpha_y\left(I_2 + I_5\right)]}^{A_1 \neq 0} +$$
$$[y_{Bmax}/4\left(3\alpha_x + \alpha_y\right)\left(I_1 + I_3 + I_4 + I_6\right) + y_{Bmax}\alpha_y\left(I_2 + I_5\right) -$$
$$1/2\beta_y\left(I_1 + 2I_2 + I_3 - I_4 - 2I_5 - I_6\right)] \quad (5.7)$$

the term $A_1$ is the non-zero part of this force equation, since the magnetic force at the $B_{max}$ location is zero. Therefore, the force equation can then be derived as

$$f_y = f_e = \Delta y/4\left(3\alpha_x + \alpha_y\right)\left(I_1 + I_3 + I_4 + I_6\right) + \Delta y\alpha_y\left(I_2 + I_5\right) \quad (5.8)$$

We assume that the environmental forces apply to the microrobot in y-direction and keep $x_r = 0, z_r = z_0$ [environmental force in the x-direction is zero, $f_x = 0$, and the microrobot's weight is the only force in the z-direction]. Therefore, using Eq. 3 and 5 results in

$$I_1 + I_2 + I_3 + I_4 + I_5 + I_6 = C_1 \quad (5.9)$$
$$I_1 + I_4 - I_3 - I_6 = 0 \implies I_1 + I_4 = I_3 + I_6 = C_2 \quad (5.10)$$

where $C_1$ and $C_2$ are constants for motions in the y-direction; replacing these two relation in Eq. 5.8 re-presents the force model as

$$f_y = f_e = \Delta y \underbrace{\left[\frac{3}{2}\alpha_x C_2 + \frac{1}{2}\alpha_y\left(2C_1 - 3C_2\right)\right]}_{C} = C\Delta y \quad (5.11)$$

This equation demonstrates that the magnetic force applies to the microrobot is linearly proportional to the distance of the microrobot from the $B_{max}$ location. Thus, by determining the $B_{max}$ location and the constant $C$ in Eq. 5.11, the environmental force in the steady-state condition can be estimated. Using magnetic flux measurement technique introduced in Section 5.1, the $B_{max}$ location can be determined.

## 5.2.2 Experimental Validation And Force Calibration

Section 5.2.1 discussed the environmental force model -equals to the magnetic force in the steady-state condition-, which is linearly the function of the distance of the microrobot from the $B_{max}$ location, Eq. 5.11. Section 5.1.1 discussed the technique for estimating the $B_{max}$ location in the y-direction, Eq. 5.1. Replacing the $B_{max}$ location, Eq. 5.1, in the force model relation, Eq. 5.11, results in the following derivation of the force

$$f_y = f_e = C\Delta y = C\left(y_r - y_{B_m ax}\right) = C\left(y_r - 0.044v_d - 0.0069\right) = \\ C_r y_r + C_v v_d + C_0 \tag{5.12}$$

where $C_r$, $C_v$, and $C_0$ are constant coefficients that can be determined by a series of experimental measurements. Since Eq. 5.12 has three coefficients, these coefficients can be determined by defining at least three equations. Depending on the number of calibration points, the coefficients of the Eq. 5.12 can then be determined as

$$\begin{bmatrix} C_r \\ C_v \\ C_0 \end{bmatrix} = \begin{bmatrix} y_{r_1} & v_{d_1} & 1 \\ y_{r_2} & v_{d_2} & 1 \\ \vdots & \vdots & 1 \\ y_{r_{n-1}} & v_{d_{n-1}} & 1 \\ y_{r_n} & v_{d_n} & 1 \end{bmatrix}^{\dagger} \begin{bmatrix} f_{y_1} \\ f_{y_2} \\ \vdots \\ f_{y_{n-1}} \\ f_{y_n} \end{bmatrix} \tag{5.13}$$

where the subscript $i$ denotes the number of the calibration point, and $\dagger$ is the generalized inverse or pseudo-inverse operation of a matrix. To obtain calibration points, a high precision force measurement setup has been designed based on the tip deflection of a cantilever, Fig. 5.10 shows this setup. The microrobot used for this study includes a cylindrical permanent magnet, the radius of 5 mm and the height of 10 mm, as the head of the microrobot with a needle-base end-effector. The weight of this microrobot is 11 gr. The aluminum cantilever is 50×5×0.05 $mm^3$ and made by Aluminum alloy 1100. The laser sensor measures the tip deflection of the cantilever with the accuracy. The force applied to the tip of the
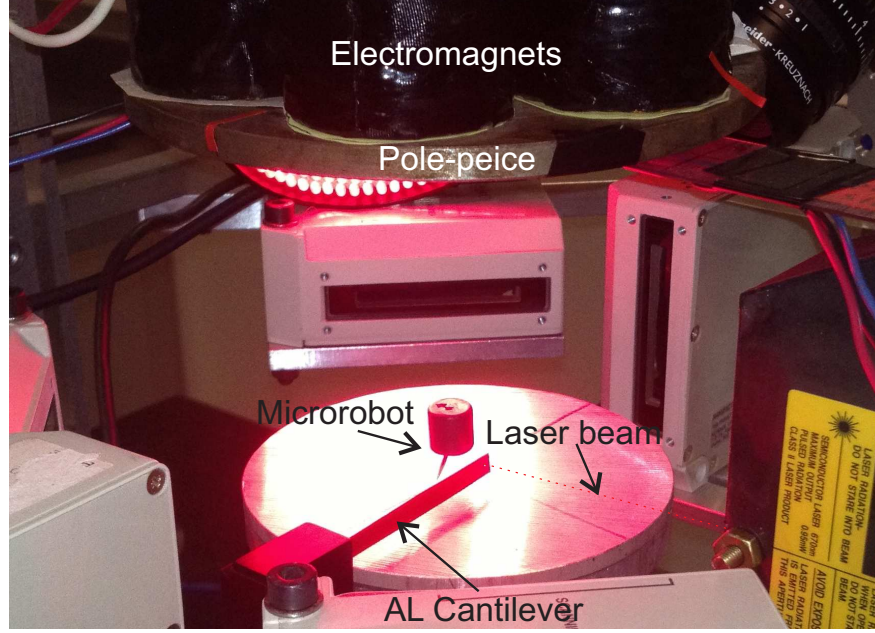
Figure 5.10: Force measurement setup-using cantilever tip deflection

cantilever can be obtained by

$$P = \frac{3EI\delta}{l^3} \qquad (5.14)$$

where $E$, $I$, $l$, and $\delta$ are modulus of elasticity, area moment of inertia, length, and elastic deflection, respectively. The accuracy analyses demonstrated that the cantilever-based force measurement method provides the error of less than 0.64 $\mu$N in measuring the applied force to the cantilever's tip, in Appendix B the accuracy analysis is presented. However, this error can be reduced by increasing the accuracy of deflection measurement and physical properties of the cantilever. In the experimental measurement, the cantilever is placed with zero distance from the microrobot, and the microrobot is then commanded toward the cantilever's tip in several steps and then moved backward to detach from the cantilever's tip. As shown in Fig. 5.11, the microrobot starts pushing moderately the cantilever's tip at the time of 32.3 second by increasing the magnetic flux differential [the flux differential changes in voltage ($v_d$) versus the real position of the microrobot ($y_r$) is presented in Fig. 5.11.b], and the deflection measurement records first
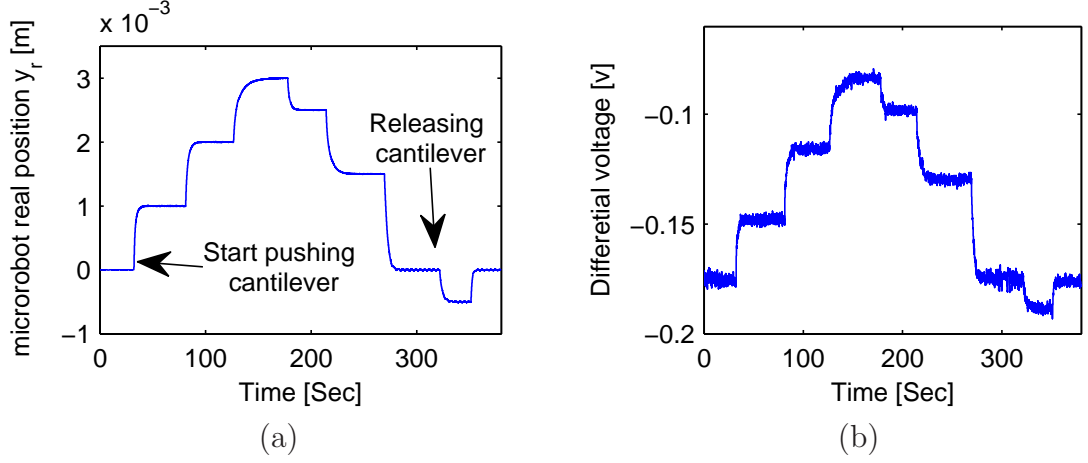
Figure 5.11: The microrobot is commanded toward the cantilever's tip: a) real position of the microrobot b) flux differential in voltage

displacement of the cantilever's tip at time of the 32.7 second. The microrobot is detached form the cantilever's tip at the time 321 second, since the microrobot is commanded to move to the position -0.5 mm. Although the releasing process has softly taken place, a small vibration occurs in the cantilever as seen in Fig. 5.12 which presents the deflection of the cantilever's tip and the measured force by Eq. 5.14.

To calculate the force by using Eq. 5.12, the flux differential in voltage and the real position of the microrobot are instantaneously recorded during the experimental measurements, previously demonstrated by Fig. 5.11.b. Using Eq. 5.13 and the obtained calibration points, the unknown coefficients of Eq. 5.12 can then be determined as $C_r = -5.47 \times 10^{-3}$, $C_v = 2.42 \times 10^{-5}$, and $C_0 = 4.09 \times 10^{-6}$. The force applied to the cantilever's tip can be calculated by the Hall-effect sensors method by replacing the derived coefficients in Eq. 5.12, shown in Fig. 5.13 the comparison of the two force measurement methods: measuring the deflection of the cantilever and the Hall-effect-based measurement. As shown in this figure, the Hall-effect-based method can accurately estimate the deflection force. To validate the performance of Hall-effect-based method corresponding to the cantilever-based technique, the root-mean-square (RMS) of the force error, calculated force obtained by Hall-effect-based method minus the measure force obtained by the cantilever-based technique, has been calculated as 0.63 $\mu$N.
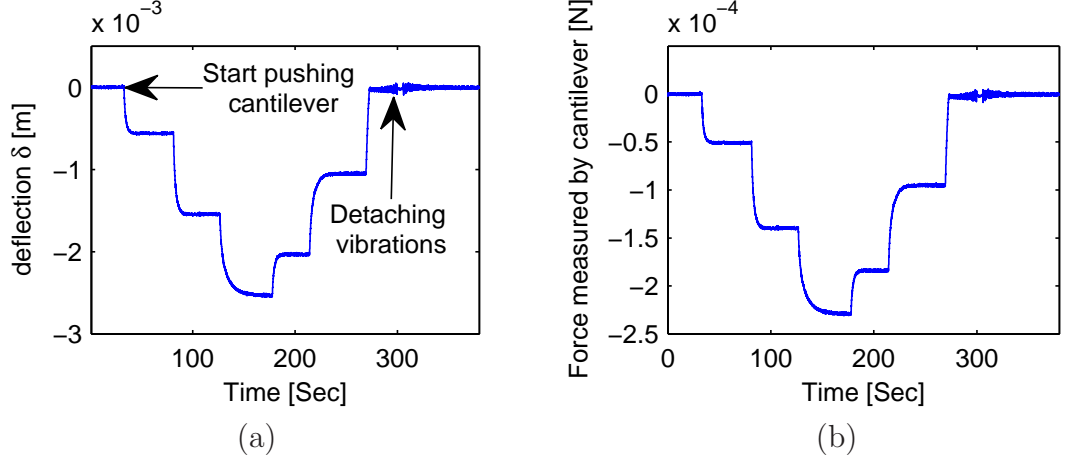
Figure 5.12: The microrobot is commanded toward the cantilever's tip: a) cantilever's tip deflection b) force estimated based on the measured deflection

Thus, the non-contact force estimation technique, Hall-effect-based method, provides high accuracy relative to the measured force by the cantilever-based routine. Since the cantilever-based technique has the accuracy of 0.64 $\mu$N, the accuracy of Hall-effect-based method can be calculated as 1.27 $\mu$N.

The concept of Hall-effect-based force measurement, in Section 5.2.1, is based on the distance of real position of the microrobot and the estimated $B_{max}$ location, Fig. 5.14 demonstrates the change of $B_{max}$ location versus the microrobot's real position, when the microrobot pushes the cantilever. As expected, by increasing the cantilever's deflection, the distance of the microrobot's position from the $B_{max}$ location becomes larger. As shown, when the microrobot is in contact with cantilever, there is discrepancy between the microrobot's position and the estimated $B_{max}$ location, and whenever the microrobot is detached from the cantilever, the microrobot's position and the estimated $B_{max}$ are very closed to each other, Fig. 5.15 presents the linear relation of applied force to the microrobot by measuring the distance of the microrobot from the estimated $B_{max}$.
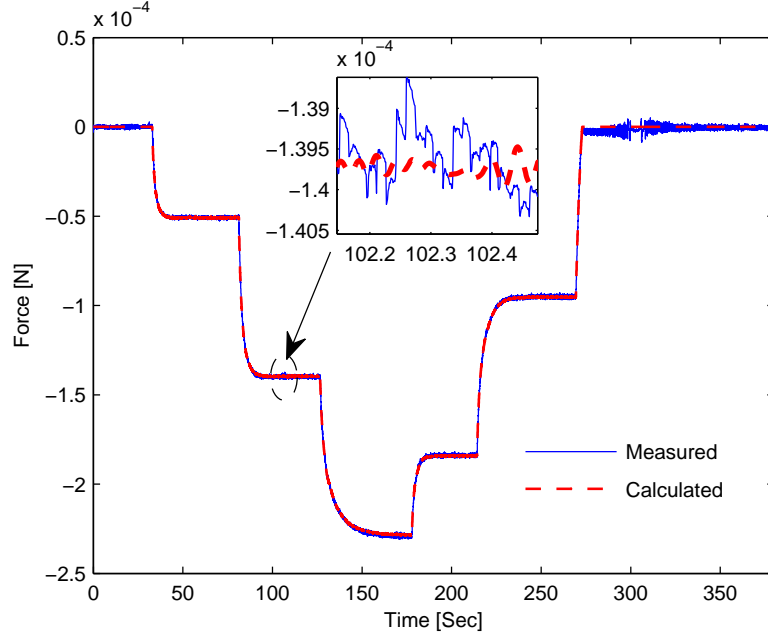
Figure 5.13: The comparison of the two force measurement methods: measured by the deflection of the cantilever and calculated by the Hall-effect-based method
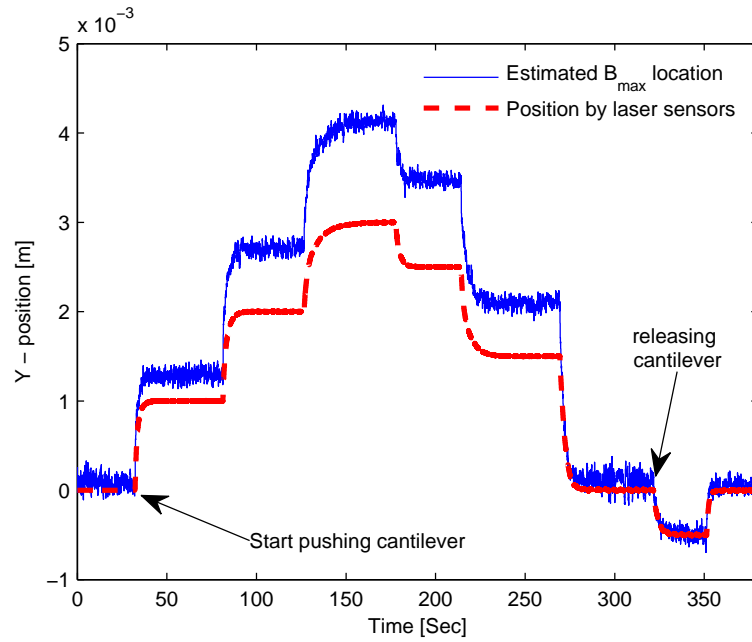


Figure 5.14: The microrobot's position versus estimated $B_{max}$ location- the cantilever is placed with zero distance distance from the microrobot
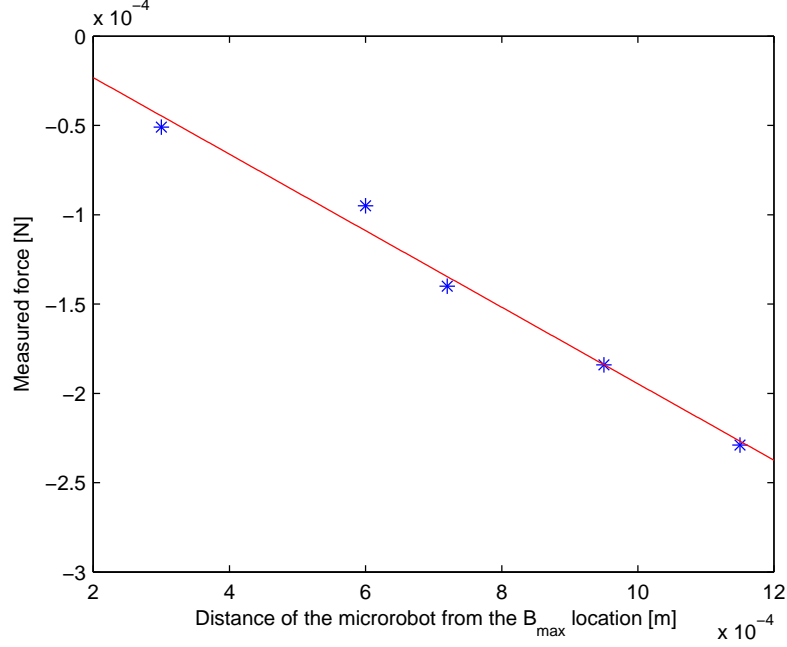
Figure 5.15: Changes of force in respect to the distance of the microrobot from the $B_{max}$ location

## 5.3 Summary

This chapter introduced a new position estimation technique for a magnetic un-tethered microrobotic system (MUMS). In our previous studies, a combination of laser sensors was used to determine the microrobot's position in the MUMS's structure. However, laser sensors cannot be used in an opaque/blocked environment. A Hall-effect-based position estimation technique is originated to estimate the microrobot's position in free levitation status when the laser signal is un-available. We defined a relation between the position of the microrobot and the produced magnetic flux. The magnetic flux was measured by an arrangement of Hall-effect sensors. Various arrangements of Hall-effect sensors were investigated to find an effective configuration for high accuracy position estimation. Based on the selection of the most effective configuration, the microrobot's motion performance was evaluated through experiment. The experimental investigations led to the "proof-of-concept" of substituting the laser sensors with Hall-effect sensors. The proposed position estimation technique provided 0.3 mm accuracy in most

of MUMS's working envelope. Future works need to establish a more effective arrangement of Hall-effect sensors to achieve higher position estimation. Furthermore, a three dimension (3-D) position estimation with Hall-effect sensors can be developed for full operation of the microrobot inside a non-transparent environment.

Furthermore, a novel micro-domain force measurement methodology is proposed in this chapter for a magnetic-haptic micromanipulation platform (MHMP). The MHMP enables a human operator to control the micro slave robot by manoeuvring the macro-master haptic robot. To allow the human operator the feeling of a micro-domain task, the micro-domain force estimation method is developed to measure the environmental force in a single-axis direction. This method uses magnetic flux measurement and the microrobot's position information to calculate the environmental force. No force sensor is attached to the microrobot to measure the force, that keeps the microrobot's size restriction and makes the microrobot inexpensive and disposable for widespread biological applications.

# Chapter 6

# Bilateral Teleoperation and Graphical Interface[1]

## 6.1   Introduction

To overcome the current lack of knowledge within the micro-domain environment, bilateral teleoperation technology is employed to allow a human operator to "feel" the micro-domain environment and intervene in tasks such as cell manipulation/injection, palpation, and controlled micro-assembly.  The extent of preserving the "feel" of an environment is characterized by the "transparency" of the system.  To achieve high transparency, most of the bilateral teleoperation strategies assume that the applied force/torque from the environment can be directly measured by sensors. However, attaching force/torque sensors to our microrobot is impracticable because:

- micro-scaled sensors must be attached to the microrobot for measuring forces/torques; hence, the size and weight of the floating microrobot is largely increased.

- an on-board wireless communication device is required to access the sensors' measurements, since the microrobot is controlled without contact by the magnetic field.

- micro-scaled force/torque sensors are expensive and highly sensitive to the physical parameters of an environment.

An alternative approach is position-error-based (PEB) bilateral teleoperation, in which both the master and slave are controlled by using position measurements. The microrobot position can be measured by external laser micrometer beams with no need for contact. Lawrence [63] showed that PEB with linear time-invariant controllers provides poor transparency. A gain-switching control scheme was proposed by Ni [77] to improve the PEB architecture's transparency. It succeeded in providing good transparency for two extreme cases: 1) the slave in free motion, to improve the transparency of PEB architecture, and 2) the slave in hard contact. In our study, the gain-switching PEB control scheme is employed as one of the strategies of the scaled-bilateral teleoperation system (SBTS) for the MHMP.

Furthermore, compared to this PEB method, the fidelity and reliability of the SBTS can be enhanced if the SBTS is fed with the measurements of master and/or slave-side forces. Therefore, by using the previously developed force measurement technique, the SBTS is fed with the slave's (the microrobot's) environmental force. In the experiment, which is performed using a haptic-enabled MUMS test bed, two-channel bilateral control architecture known as Direct-force-reflection (DFR) is implemented for the MHMP.

In addition, this chapter deals with the development of a virtual reality interface (VRI) for the MHMP. We report a VRI that enables human operators to improve their skills in using the MHMP before carrying out an actual task. The VRI also provides promising capability in the creation of multiple viewports of a real scene, resulting in increased task reliability and comfort for the human operator.
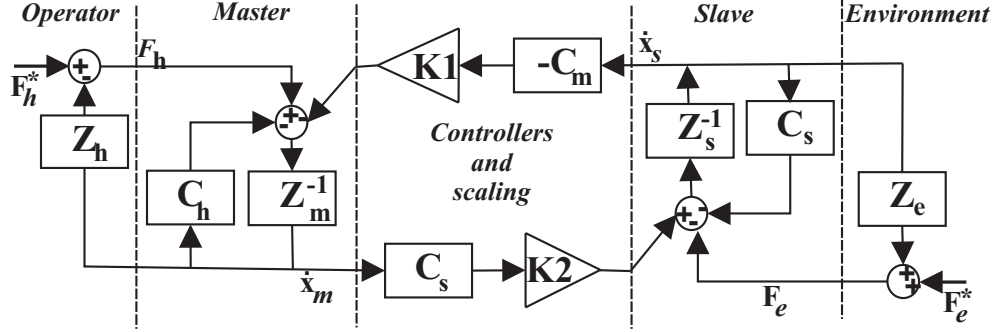
Figure 6.1: Schematic of symmetric PEB teleoperation

## 6.2 Gain-Switching Control Strategy (PEB-based Teleoperation

In this section, the concept of transparency analysis is firstly presented for a symmetric bilateral PEB system. The concept of the gain-switching scheme for transparency improvement is then reviewed based on the proposed method by Ni [77], the stability of the gain-switching scheme in contact, free motion, and transition conditions is briefly discussed. In this part of our study, we implemented a previously proposed PEB method, hence, the proof of theorems and lemmas are not mentioned directly in this report, but can be followed in the original reference by Ni [77].

### 6.2.1 Transparency Analysis

A bilateral teleoperation interface provides the human operator with information about the task environments. To obtain such a system, combinations of force and position measurements from the slave side can be utilized. In particular, in the PEB scheme, the reflected force to the human operator is proportional to the position error. Figure 6.1 presents such a symmetric PEB system. In this figure, $F_h$ and $F_e$ denote hand/master and slave/environment interaction respectively. $F_h^*$ and $F_e^*$ are respectively the operator's and environment's exogenous input forces, and both are independent of teleoperation system behavior. Generally, it is assumed that the environment and operator are passive ($F_h^* = F_e^*$). The
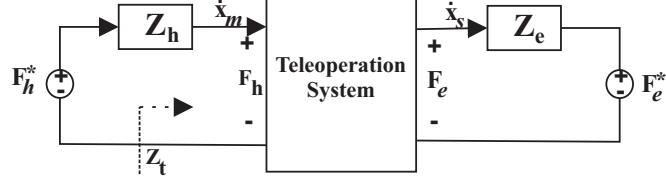
Figure 6.2: Two-port model of a bilateral teleoperation

velocity of the master and slave are respectively defined by $\dot{x}_m$ and $\dot{x}_s$. The impedances $Z_m$ and $Z_s$ represent the dynamic characteristic of master and slave respectively; both impedances include inner-loop controllers. Additionally, $C_m$ and $C_s$ are the impedance form of PD controllers for master and slave sides as

$$C_m(s) = K_{dm} + \frac{K_{pm}}{s} \tag{6.1}$$

$$C_s(s) = K_{ds} + \frac{K_{ps}}{s} \tag{6.2}$$

The master and slave may have different workspaces; hence, $K_1$ and $K_2$ are the scaling factors for the mapping of workspaces. To make two workspaces overlap each other virtually, $K_1$ and $K_2$ must satisfy $K_1 \times K_2 = 1$.

To evaluate the transparency of PEB teleoperation, the two-port network model of teleoperation, shown in Fig. 6.2, can be represented by a hybrid impedance matrix as

$$\begin{bmatrix} F_h \\ F_e \end{bmatrix} = Z \begin{bmatrix} \dot{x}_m \\ -\dot{x}_s \end{bmatrix} \tag{6.3}$$

where the hybrid impedance matrix for the symmetric PEB teleoperation can be derived as

$$Z(s) = \begin{bmatrix} Z_m(s) + C_m(s) & K_2 C_m(s) \\ K_1 C_s(s) & Z_s(s) + C_s(s) \end{bmatrix} \tag{6.4}$$

Perfect transparency [63] is achieved with and only with a perfect match of the environment impedance $Z_e = F_e/\dot{x}_s$ to the impedance transmitted to the operator's hand $Z_h = F_h/\dot{x}_m$. In practice, a perfectly transparent teleoperation

111

will not be possible with PEB architecture, so it makes sense to investigate the transparency in specific cases: a slave in free motion ($Z_e \longrightarrow 0$) and a slave in hard contact ($Z_e \longrightarrow \infty$). For the PEB architecture, the transmitted impedance to the operator's hand can be obtained from the hybrid impedance matrix as

$$Z_h = Z_m + C_m - \frac{C_m Z_s}{Z_e + Z_s + C_s} \tag{6.5}$$

when the slave in free motion, $Z_e \longrightarrow 0$; $Z_h$ becomes

$$Z_h = Z_m + C_m - \frac{C_m Z_s}{Z_s + C_s} \tag{6.6}$$

Achieving complete transparency in free motion requires $Z_h \longrightarrow 0$ . Since all the impedances have positive values, the transmitted impedance cannot be zero ($Z_h \succ Z_m$). If the master PD controller has very low gains and the slave PD controller has very high gains, the impedance of the master is transmitted to the operator's hand. Furthermore, the high gain of the slave PD controller causes good position tracking in free motion. When the slave in hard contact, $Z_e \longrightarrow \infty$; $Z_h$ becomes

$$Z_h \longrightarrow Z_m + C_m \tag{6.7}$$

This equation represents that the dynamic of the master and its controller is transmitted to the operator's hand. However, if the master controller has very high gain and the slave controller has very low gain, the feel of hard contact can be transmitted to the operator's hand by high impedance. In addition, the low gain of slave PD controller avoids hard collision with the hard contact. Therefore a gain-switching control scheme will enhance transparency of the PEB teleoperation in free motion and hard contact cases.

### 6.2.2  Stability of PEB teleoperation

The stability of a teleoperation system depends on the human operator knowledge and environment dynamics. Human operator dynamics is highly adaptive, and the environment impedance is also usually unknown. Therefore, it is nec-

112

essary to find stability conditions, absolute stability, which depends only on the teleoperator. Based on Llewellyn's criteria, the PEB teleoperation system is absolutely stable if all the gains of master and slave PD controllers are positive and $K_{pm}/K_{ps} = K_{dm}/K_{ds}$, Theorem I in [77]. Therefore, the absolute stability only depends on the controller gains. It does not require any parameters of the master or slave dynamics, which usually contain modeling uncertainty. However, the condition given by Llewellyn's criteria guarantee absolute stability only of a liner time-invariant (LTI) system. In our case, this dynamic applies when the teleoperation system is well inside either the free motion or hard contact. However, the dynamic of the system is time-varying in the contact transition.

During the contact transition, the system dynamic is switching between unconstrained space and constrained space. Physically, the slave manipulator is kicked back by the contact surface for a few times, a situation called transition mode. Absolute stability is necessary, but not a sufficient condition for teleoperation stability. Ni [77] investigated the asymptotic stability of the PEB teleoperation system in a constrained space, unconstrained space and transition mode. The gain-switching to achieve better transparency makes the contact transition stability more complicated.

To investigate the absolute stability of gain-switching, two sets of controllers are presented. The PD controller gains for free motion are defined as $[K_{pm}^l,$ $K_{dm}^l, K_{ps}^h, K_{ds}^h]$ and for hard contact as $[K_{pm}^h, K_{dm}^h, K_{ps}^l, K_{ds}^l]$. Ni [77] showed the asymptotic stability of asynchronous gain-switching in the following cases: unconstrained motion with unconstrained gains, constrained motion with unconstrained gains, unconstrained motion with constrained gains, and constrained motion with constrained gains [77].

### 6.2.3 Design of Gain-Switching rules

Achieving transparency requires the gain-switching between high and low for master and slave controllers. Since two extreme cases, free motion and hard contact, are considered in this study, the gain-switching can be triggered by

filtered position error, $\delta$, of the system as

$$\delta = \left\| k_p + k_i \int e dt \right\| \tag{6.8}$$

where $e$ is the position error, the difference between the scaled position of the master and the real position of the slave. Two parameters $k_p$ and $k_i$ were determined by experiments. The parameter $\delta$ was measured in both free motion and contact cases, and then two parameters $\delta_{free}$ and $\delta_{contact}$ were tuned for the following gain-switching rules

- If the master PD controller is low and the slave PD controller is high and $\delta \succ \delta_{contact}$ then the master should be switched to high and the slave to low.

- If the master PD controller is high and the slave PD controller is low and $\delta \prec \delta_{free}$, then the master should be switched to low and the slave to high.

- Otherwise the controller gains are not switched.

Figure 6.3 presents the block diagram of the gain-switching teleoperation system. All the switching parameters, $\gamma = [k_p \; k_i \; \delta_{free} \; \delta_{contact}]$, were tuned experimentally and change any of them can change the sensitivity of switching.

## 6.2.4 Tuning the gain-switching parameters

Finding proper gain-switching parameters, $\gamma$, influences the MHMP performance. Hence a considerable experimental analysis is required to tune these parameters. The position errors are first recorded for a series of random motions inside the workspace, with no presence of hard contact. Therefore, a bound of the filtered position errors can be determined for the free motion tasks. The parameter $\delta_{free}$ can then be selected as the upper range of the filtered position errors. Choosing the parameter $\delta_{contact}$ significantly depends on the sensitivity of task. Generally, this parameter is larger than $\delta_{free}$. For slow and very sensitive tasks, $\delta_{contact}$ is selected close to the $\delta_{free}$ to reduce the risk of damage for the manipulated object,
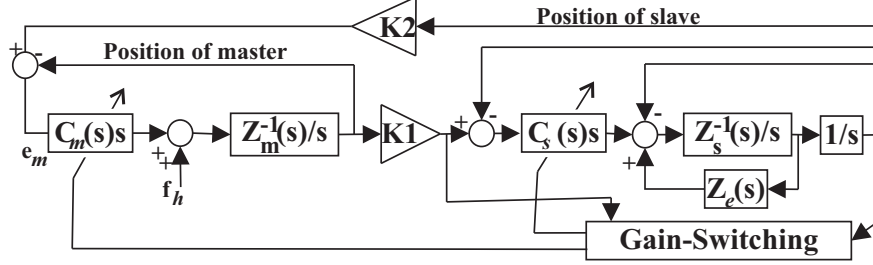
Figure 6.3: Block diagram of gain-switching control scheme

but if these two parameters are selected very close to each other, that possibly causes undesirable high frequency switching in contact transition mode. To avoid switching, a relatively larger value is selected for $\delta_{contact}$, so the sensitivity in encountering hard contact is reduced.

Choosing suitable $k_p$ and $k_i$ can compensate for the sensitivity of contact detection if a large $\delta_{contact}$.is used. If the integral part of the filtered error has a larger value relative to the proportional part, by increasing the gain $k_i$, the gain-switching provides an acceptable switching time in contact detection. Therefore, based on the tasks, there is trade-off for selecting the gain-switching parameters. In our study, several sets of gain-switching parameters of different sensitivities were considered. The following section discusses experimental analysis of MHMP.

### 6.2.5  Experimental investigation of the MHMP

The proposed MHMP has been tested on the experimental setup described in Chapter 2. The microrobot II has been used in this experiment, Fig. 6.4 shows the levitated microrobot II. To have stiff environment (hard contact) in the experiment, a sheet of plexiglass was used. The lasers detect microrobot through plexiglass.

The switching parameters $\gamma = [k_p\ k_i\ \delta_{free}\ \delta_{contact}]$ are selected by trial-and-error as $\gamma = [0.9\ 0.1\ 0.0007\ .001]$. The $\delta_{free}$ and $\delta_{contact}$ should be selected to make asynchronous switching [77]. The gain-switching is defined as, when the gain switch to 1 the PD controllers gains are $[K_{pm}^h = 200,\ K_{dm}^h = 2,\ K_{ps}^l = 0.2,\ K_{ds}^l = 0.002]$ and when the gain switch to 0 the PD controller gains

Figure 6.4: The levitated microrobot II

are $[K_{pm}^l = 0.1,\ K_{dm}^l = 0.001,\ K_{ps}^h = 1,\ K_{ds}^h = 0.01]$. The superscript $l$ and $h$ denote low and high, respectively. The gains are tuned by trial and error, subject to the stability conditions $K_{pm}^h/K_{ps}^l = K_{dm}^h/K_{ds}^l$, $K_{pm}^l/K_{ps}^h = K_{dm}^l/K_{ds}^h$.

The experimental results were shown in Fig. 6.5. This figure shows the vertical motion of the microrobot relative to the center of the workspace. The phantom motion is in the range $[-40\ 40]$ $mm$ and mapped to $[-65\ 95]$ $mm$ as the microrobot motion range. A hard contact was placed in z-direction at 4.72 $mm$ from the center of workspace. The switching occurred with 150 $msec$ delay, which is acceptable for this application. Figure 6.6 presents the teleoperation position tracking error; it shows the $RMS$ of tracking error in free motion is 40 $\mu m$ . In a small range of motion, the laser sensor can provide ultra high accuracy position feedbacks. Hence, several experiments have been investigated in a small range to enhance the motion resolutions. Figure 6.7 presents the teleoperation performance in controlling the microrobot performance in free motions. In the motion range of 2 $mm$ at center of laser workspace, the $RMS$ of the position tracking error is 20 $\mu m$.

In another set of experiment, the microrobot is moved in unknown viscous liquid. Since the dynamic of environment is not considered in the design process, the $RMS$ of position tracking error becomes as large as 30 $\mu m$, shown in Fig. 6.8. This experiment shows a promising capability of the MHMP in maintaining
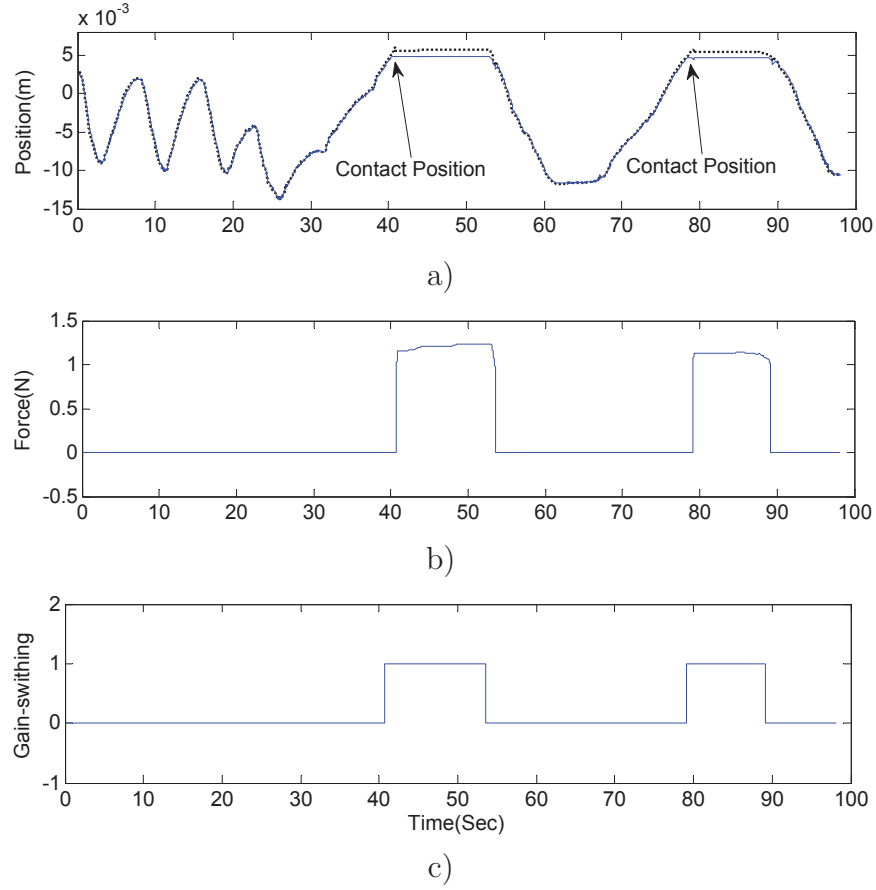
Figure 6.5: Experimental results of gain-switching control in z-direction motions: (a) scaled master position (. . .) and slave position (−) b) Haptic force C) gain-switching

the system's accuracy in various environments. Human operator cannot enhance the MHMP's accuracy by adapting to environment. However, the human operator can plan a micro-manipulation task in a way that a degraded manipulation can be accomplished. For example, the human operator can feel roughly the environment's physical properties by comparing the slave and master positions. The human operator can modify the trajectory of slave-microrobot for a micro-manipulation task based on observations in various accomplished experiments. Hence, this investigation presents performance robustness and the importance of haptic application, where the human operator wants to manipulate object with no knowledge of environment physical properties.
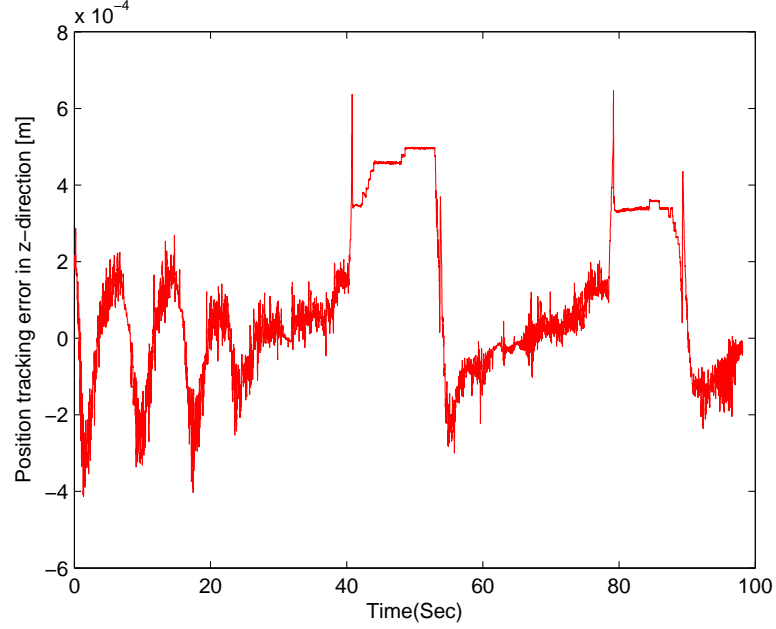
Figure 6.6: Position tracking error in z-direction motion with wide range of operation

## 6.3 Direct-force-reflection Teleoperation

In this section, the transparency and stability of DFR teleoperation is first presented. Next, the concept of a viable DFR control system is reviewed based on conventional impedance control [116] and the transparency and control rules of this method are then briefly discussed. Finally, we implement a previously proposed DFR method. Although the proof of the theorems and lemmas are not mentioned directly in this report, they can be followed in the references [116].

### 6.3.1 Transparency of DFR teleoperation

The overall architecture of Direct-force-reflection (DFR) bilateral teleoperation system is presented in Fig. 6.9. As mentioned in the introduction of this chapter, the DFR requires a force sensor to measure the interaction force between the

118
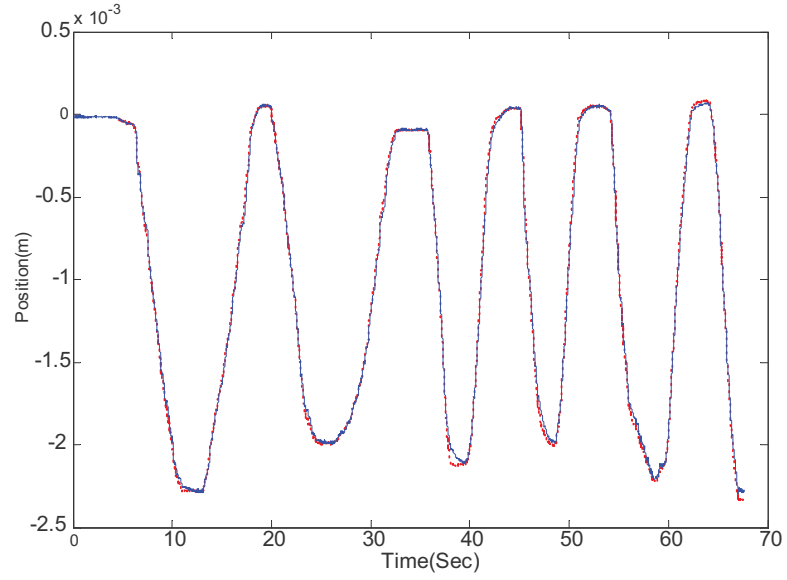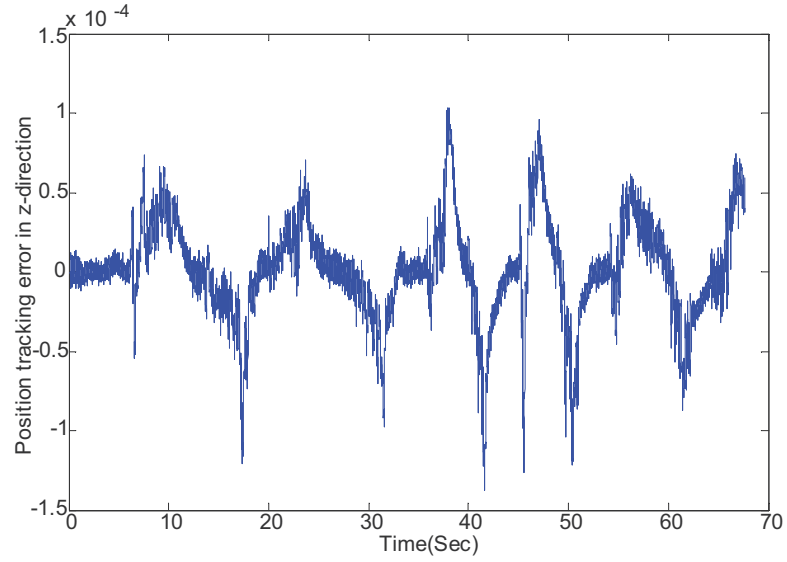
Figure 6.7: Free motion of a microrobot in small range task, a) scaled master position (. . .) and slave position (−) b) tracking error in z-direction
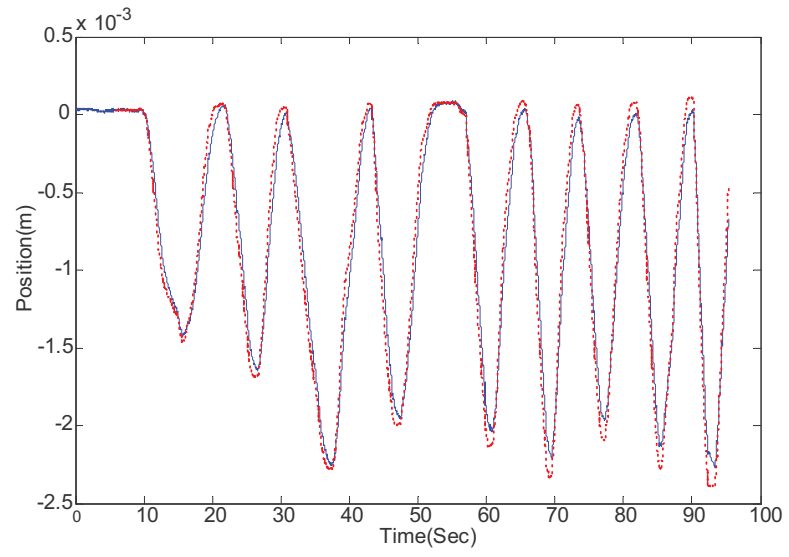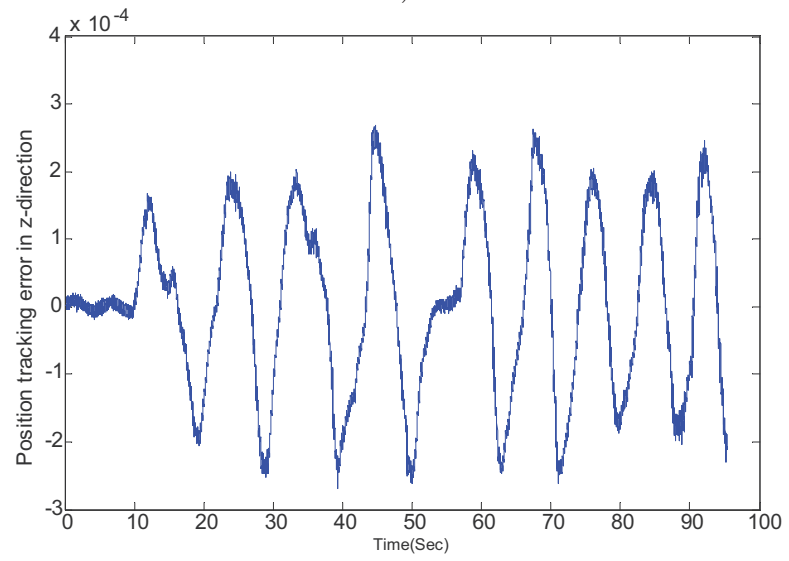
Figure 6.8: Free motion of a microrobot in small range task in a viscous fluid, a) scaled master position (...) and slave position (−) b) tracking error in z-direction

slave (the microrobot) and the environment. The hybrid parameters for the DFR architecture are defined as,

$$\begin{bmatrix} F_h \\ -\dot{x}_s \end{bmatrix} = \underbrace{\begin{bmatrix} Z_m & 1 \\ -\frac{C_s}{Z_{ts}} & \frac{1}{Z_{ts}} \end{bmatrix}}_{\mathbf{H}} \begin{bmatrix} \dot{x}_m \\ F_e \end{bmatrix} \tag{6.9}$$

Accordingly, the perception of free-motion is less than the ideal case, since the $h_{11} = Z_m \neq 1$; however, the perfect force transferring can be realized due to the $h_{12} = 1$. The DFR teleoperation system introduced in Fig. 6.9 is absolutely stable if $k_{ds}, k_{ps} > 0$ and $|C_s| >> |Z_s|$, based on Llewellyn's criteria [116]. To simplify the discussion about the impedance control, and pointing out its dexterity, a one-DOF model is described as

$$M_m s^2 x_m + D_m s x_m = \tau_m + F_h \tag{6.10}$$

$$M_s s^2 x_m + D_m s x_m = \tau_s - F_e \tag{6.11}$$

where $\tau_m$ and $\tau_s$ are master driving force and slave driving force, respectively. The force $F_e$ can be presented by the environment impedance $(Z_e)$ and environment position $(x_e)$ as $F_s = Z_e (x_s - x_e)$. In this study, we consider force and position scaling in the teleoperation. Therefore, an ideal response in teleoperation between a differently-scaled world can be defined by $F_h = K_1 F_e$ and $x_s = K_2 x_m$. The bilateral control can be realized as

$$\tau_m = -K_1 F_e \tag{6.12}$$

$$\tau_s = k_p (K_2 x_m - x_s) - k_v s x_s \tag{6.13}$$

In this study, we are not focusing on the force controller design for the master side, since the haptic device has no force sensors on it [an observer-based method can be used to estimate the force for force control]. Substituting the control equation, Eq. 6.13 to the model relation, Eq. 6.11, and re-arranging them with the assumption of the environment position $x_e = 0$, the dynamics from the master
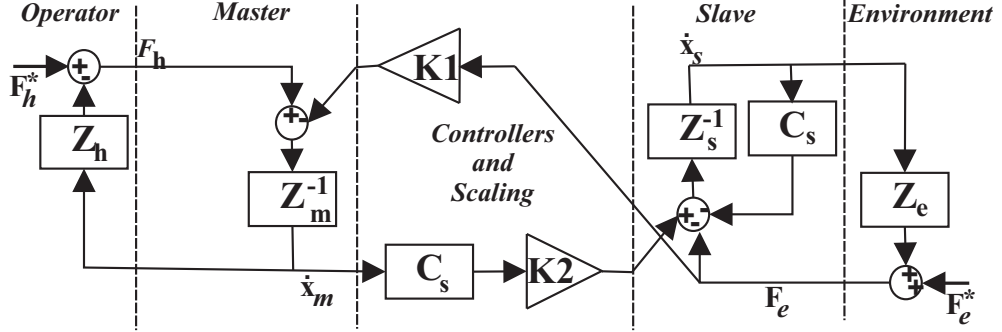
Figure 6.9: Schematic of Direct-force-reflection (DFR) teleoperation

force to the master position can be written as

$$\frac{x_m}{F_h} = \frac{M_s s^2 + (D_s + k_v) s + k_p + Z_e}{M_m s^2 + D_m s \left(M_s s^2 + (D_s + k_v) s + k_p + Z_e\right) + K_1 K_2 k_p Z_e} \quad (6.14)$$

To improve the dexterity of the system, the gains of the position controller ($k_p$ and $k_v$) are usually designed to be as high as possible while retaining stability. Thus, if the the cut-off frequency of the position controller is selected as being higher than the dynamic range of the human operator, Eq. 6.14 can be approximated by

$$\frac{x_m}{F_h} = \frac{1}{M_m s^2 + D_m s + K_1 K_2 k_p Z_e}, k_p >> 0, k_v >> 0 \quad (6.15)$$

According to this relation, the human operator feels the virtual environment impedance $K_1 K_2 Z_e$, through the suppressed master dynamics, $M_m s^2 + D_m s$ .

## 6.3.2   Tuning the DFR and measurements

The proposed MHMP, equipped with DFR-scaled bilateral teleoperation, has been tested on the experimental setup described in Chapter 2, with Microrobot II being used in this experiment. To create a micro-domain environment with stiffness in the y-direction, an Aluminum cantilever measuring $50 \times 5 \times 0.05 \ mm^3$ and made from Aluminum alloy 1100 is placed in the working space (see Fig. 6.10). As the figure shows, a laser sensor is used to measure the deflection of the cantilever's tip.
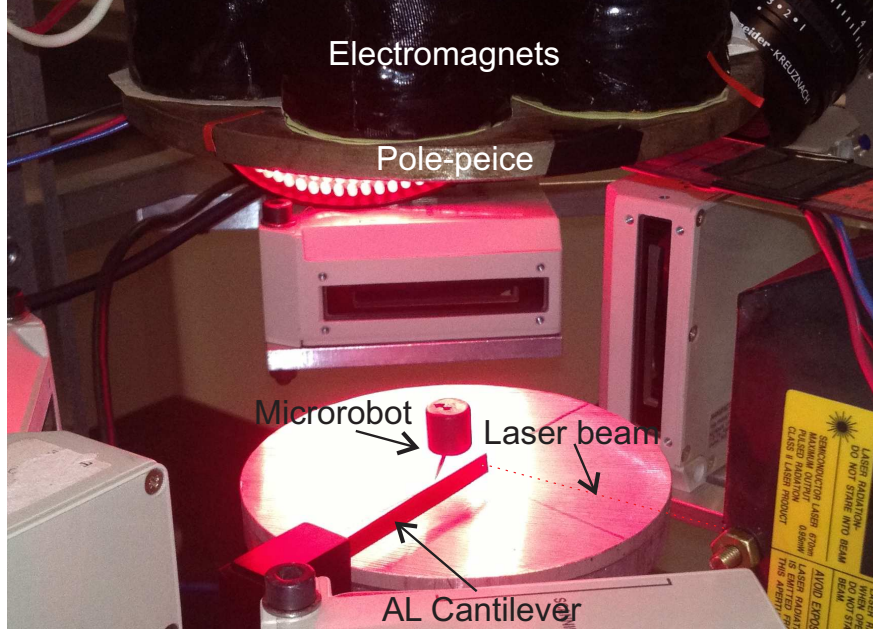
Figure 6.10: Force measurement setup-using cantilever tip deflection

The previous section demonstrated that the DFR teleoperation requires the design of a PD controller for the slave site. To place the slave closed-loop poles for a quick response, $(k_p\ k_v) = (1600\ 80)$ were chosen. This results in the position error characteristic equation $(\ddot{e}_x + 80\dot{x} + 1600e_x = 0)$, where $e_x = x_m - x_s$ for the slave side, thus moving the closed-loop poles of the slave to $(-40\ -40)$.

Figure 6.11 demonstrates the experimental horizontal motion of the microrobot with respect to the phantom stylus position in free and contact conditions. Fig. 6.12 shows free and contact conditions (the PhanTom stylus motion is in the range $[-35\ 35]\ mm$ and mapped to $[-3.5\ 3.5]\ mm$ for the microrobot motion range). It can be seen from the position tracking in Fig. 6.11 that the microrobot follows the master commands with the RMS of tracking error 0.2 mm. However, this position tracking error can be improved by designing a fast-response DFR controller. Figure 6.12 shows the microrobot's initial contact with the cantilever (at the 5.8 sec mark), where it starts pushing the cantilever and then releasing it at 23.8 sec. The results obtained from the force-sensing analysis of the Hall-effect method and the cantilever-based measurements are shown in Fig. 6.13 for the demonstrated task in Fig 6.11.
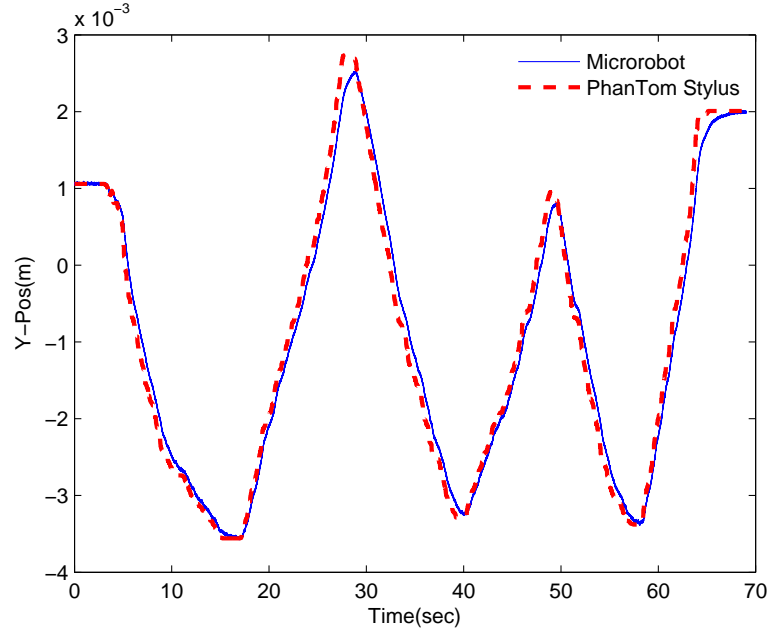
Figure 6.11: Experimental measurement of DFR teleoperation in y-direction motions, scaled master position $(--)$ and slave position $(-)$
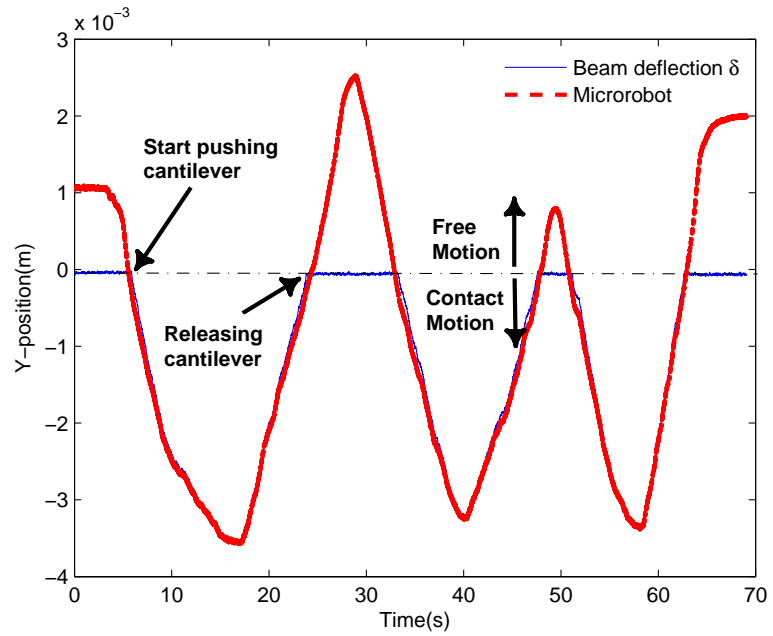


Figure 6.12: Pushing an releasing the cantilever's tip in DFR teleoperation
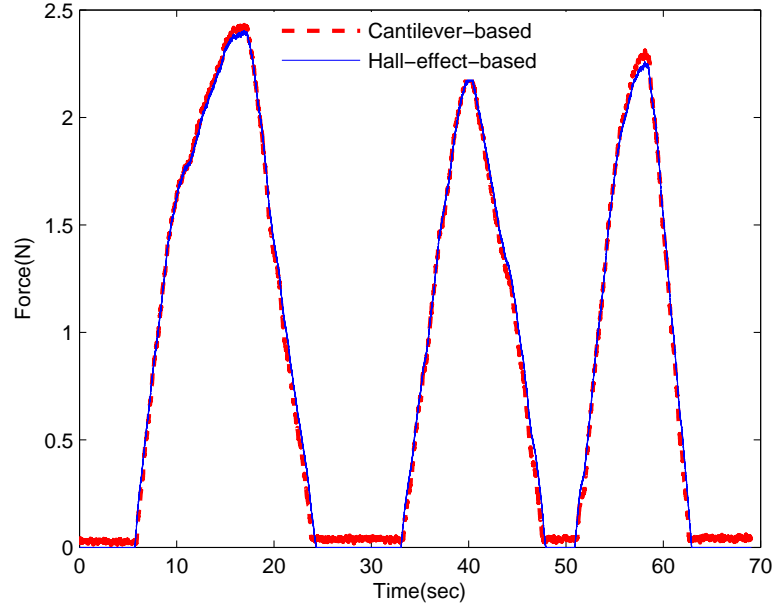
Figure 6.13: Force sensing comparison [forces are multiplied by $1 \times 10^4$], cantilever-based force sensing $(- -)$ and using Hall-effect method $(-)$

## 6.4 Human-assisted Virtual Reality

This section deals with the development of a virtual reality interface (VRI) for the MHMP. The VRI enables human operators to improve their skills in using the MHMP, before carrying out an actual dexterous task. A large number of VR-assisted micromanipulation platforms for various applications have been developed over the past few years [2; 9; 47; 89; 131]. Such a platform is described in [39], in which the proposed VR can help in overcoming problems related to poor visual feedback as well as allowing the operator to learn using the simulations of planned tasks. In [47], the authors have developed the concept of a physically behaved microrobotic workcell in virtual environments for microassembly teaching. It is reported that the workcell provides significant understanding for microassembly task teaching. As well, its effectiveness can be greatly enhanced with supporting from the microphysic-based models of the contact and elastic robotic interactions. In [2], it has also been demonstrated that the visualization of path planning in a virtual environment can effectively decrease the number of

collisions and failures; thus, enhancing the human operators' skill with higher-order task reliability in a micro-domain.

The developed VRI is made up of three main components: a haptic station, a simulation engine, and a display unit. The haptic station provides the operator with the force/torque information from virtual or remote environments, and is also used to recognize the operator's hand motion command. Dynamical computation and control system modeling have been carried out on the simulation engine. Based on the real-time computation, this engine, as the heart of the system, provides force applied to the operator's hand and the microrobot's position for the haptic station and the display unit, respectively. The display unit employs 3D computer graphics to demonstrate the micromanipulation tasks and environments. The VRI is also developed in such a way that it can be separately used in parallel with the MHMP for the 3D visualization of a real task by providing multiple virtual viewports. This section introduces the configuration of the proposed VRI, and reports the result of a preliminary experiment using micro-manipulation investigation for validation.

## 6.4.1 The description of the VRI

This interface has been developed for two principle purposes: the 3D virtual visualization of a real task and micro-manipulation task training in virtual micro-domain environments. Figure 6.4.a schematically demonstrates the MHMP and the VRI in "3D visualization mode". The VRI's simulation engine communicates with the magnetic microrobotic station (MMS) via the Ethernet. The display unit produces a 3D computer graphic visualization based on the information received from the simulation engine. This interface provides the 3D virtual visualization for the MHMP that comprehensively enhances an operator's vision of the micro-world. Figure 6.4.b provides a schematic digram of the VRI in the "simulation mode" that can be used for human operators skill improvement. As shown in this figure, the numerical model of the MMS has been realized on the simulation engine. The simulation engine is enabled to communicate with the haptic station via the Ethernet.

**Magneti-Hptic Micromanipulation Platform (MHMP)**   **Virtual Reality Interface**

**Haptic Station**   **Magnetic Microrobotic Station**

**Phantom Omni**

MDU   Current   **dSPACE**

Position

Force   Position   Force   Position

Ethernet   **Display Unit**   Ethernet

**Haptic-Master Site**   **Slave Site**   **Simulation Engine**

a) 3D visualization mode

**Haptic Station**   **Virtual Reality Interface**

**Phantom Omni**

Position   Force   **Display Unit**

Ethernet

**Haptic-Master**   **Simulation Engine**

b) Simulation mode

Figure 6.14: The schematic digram of the developed virtual reality interface (VRI)

**Simulation engine**

This section introduces the dynamic model of the MHMP and real-time simulation. The dynamical model of the MUMS can be presented based on the developed magnetic gradients presented in Chapter 3. The dynamical model is merely obtained from the application of Newton's second law as

$$m\ddot{x} = M\frac{\partial B_z}{\partial x} + c_{e,x}\dot{x} + f_{env,x} \tag{6.16}$$

$$m\ddot{y} = M\frac{\partial B_z}{\partial y} + c_{e,y}\dot{y} + f_{env,y} \tag{6.17}$$

$$m\ddot{z} = M\frac{\partial B_z}{\partial z} + c_{e,z}\dot{z} - mg + f_{env,z} \tag{6.18}$$

where $g$ is the acceleration of gravity, $m$ is the mass of the MUMS's microrobot, $M$ is the magnetization of the microrobot's head, $c_e$ is the eddy current damping factor, and $f_{env}$ is environmental force. The environmental forces are negligible; meanwhile the microrobot motion takes place in free motion and in a low viscous environment ($f_{env} \approx 0$). Hence, the magnetic force is a significant factor in the microrobot's motion control. Developing an accurate model of magnetic force results in valid system dynamics simulation. Chapter 3 has already introduced the mathematical model of magnetic force produced by the MDU. The presented model includes some important parameters such as $\alpha_x$, $\alpha_y$, $\alpha_z$, $\beta_y$, and $\beta_z$ that need to be precisely determined. Furthermore, the magnetization of microrobot's head which is hard to measure is required for the magnetic force calculation. Since the magnetization has a linear direction relation with the magnetic force, the effect of this parameter can be considered in experimental parameters (for example $\alpha_z = M\alpha_z$).

To determine the precise values for coefficients $\alpha_z$ and $\beta_z$, a PID feedback controller was implemented for the MUMS and the microrobot was levitated at two vertical positions($z_1$ and $z_2$). Given the fact that at steady state, the magnetic force is equal to the weight of the microrobot, different sets of equations were formed and the vertical experimental measurements were determined. The

a) Vertical motion           b)Horizontal motion
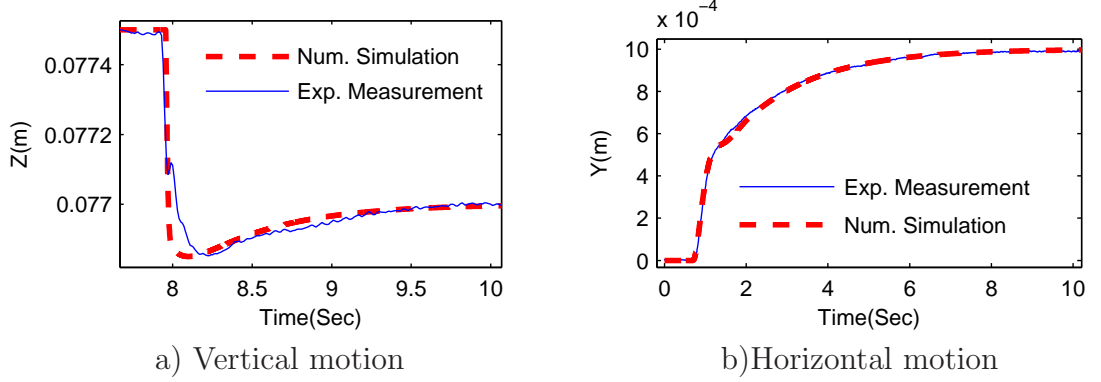
Figure 6.15: Step response in vertical and horizontal motions, Comparing numerical simulation and experimental measurement

coefficients are then calculated by

$$\alpha_z = \frac{mg\left(I_2^* - I_1^*\right)}{I_1^* I_2^* \left(z_1 - z_2\right)} \tag{6.19}$$

$$\beta_z = \frac{mg\left(I_1^* z_1 - I_2^* z_2\right)}{I_1^* I_2^* \left(z_1 - z_2\right)} \tag{6.20}$$

where $I_1^*$ is the summation of current, $I_1^* = \sum_{i=1}^{6} I_i$ , at distance $z_1$, and $I_2^*$ is the summation of currents at distance $z_2$. The variation of these coefficients with respect to the working envelope is less than 5% (Chapter 3); hence, the mean values of $\alpha_z$ and $\beta_z$ were used as the force coefficients over the entire operation range of the system ($\alpha_z = -2.90986$ and $\beta_z = 0.34864$). The experimental measurements showed that the eddy current damping factor $c_{e,z}$ has insignificant value in z-direction; therfore, we assumed $c_{e,z}$ equals zero in vertical motion. Figure 6.15.a compares the simulated dynamic in vertical motion with experimental measurements in a step response, using a 11.2 gr microrobot.

In contrast to the vertical magnetic force model, the dynamical response analyses of horizontal motion are needed to determine the horizontal magnetic force's parameters. There is no specified static force in the horizontal plane while the levitated microrobot has been move in a free motion. Thus, we have to investigate dynamical motions to determine the horizontal magnetic force parameters.

For dynamical response analyses, we linearize the nonlinear model as defined by Eq. 6.16 and Eq. 6.17. The linearized dynamic of the microrobot at the center point of the workspace, $[x_c \; y_c \; z_c] = [0 \; 0 \; z_0]$ and $I_1 = I_2 = I_3 = I_4 = I_5 = I_6 = I_0$, can be represented as,

$$m\ddot{x} + c_{e,x}\dot{x} - 3x\left(\alpha_x + \alpha_y\right)I_0 = \frac{-\sqrt{3}}{2}\beta_y \underbrace{\left(i_1 - i_3 + i_6 - i_4\right)}_{v_x} \qquad (6.21)$$

$$m\ddot{y} + c_{e,y}\dot{y} - 3y\left(\alpha_x + \alpha_y\right)I_0 = \frac{1}{2}\beta_y \underbrace{\left(i_1 + 2i_2 + i_3 - i_4 - 2i_5 - i_6\right)}_{v_y} \qquad (6.22)$$

where $i_j$ is the perturbed current for the $j^{th}$ electromagnet ($j = 1, \cdots, 6$). The virtual command for motion in x- and y-directions are defined as $v_x$ and $v_y$, respectively. The current $I_0$ can be determined from the following relation,

$$\sum F_z = 0 \Rightarrow$$

$$\left(\alpha_z z_0 + \beta_z\right) \sum_{i=1}^{6} I_i - mg = 0 \Rightarrow I_0 = \frac{mg}{6\left(\alpha_z z_0 + \beta_z\right)} \qquad (6.23)$$

Therefore, the input-output transfer function in the Laplace domain for the horizontal motion, Eq. 6.21 and 6.22, can then be re-presented as,

$$\frac{X\left(s\right)}{V_x\left(s\right)} = \frac{-\sqrt{3}/2\beta_y}{ms^2 + c_{e,x}s - 3\left(\alpha_x + \alpha_y\right)I_0} \qquad (6.24)$$

$$\frac{Y\left(s\right)}{V_y\left(s\right)} = \frac{1/2\beta_y}{ms^2 + c_{e,y}s - 3\left(\alpha_x + \alpha_y\right)I_0} \qquad (6.25)$$

Experimental magnetic field measurements and geometrical analyses of electromagnets' arrangements show that we can approximate $\alpha_y \approx \sqrt{3}/2\alpha_x$. Hence, the horizontal magnetic force's parameters can then be determine by a simple experimental step response in x- or y-directions. Based on the characteristic of the second order system (steady-state gain, damping ratio, and natural frequency),

the parameters $\alpha_x$, $\beta_y$, and $c_e$ can then be defined.

Using the step response analysis in y-direction with a 11.2 gr microrobot results in $\alpha_x = -8.7 \times 10^{-2}$, $\alpha_y = -7.6 \times 10^{-2}$, $\beta_y = 2.3 \times 10^{-3}$, and $c_{e,y} = 0.098$. Figure 6.15.b demonstrates the comparison of the simulated dynamic in vertical motion with the experimental measurements in a unit step response, in the y-direction motion at $x =_0= 0$ m and $z_0 = 0.0775$ m. As clearly shown, the obtained dynamic model of the MUMS's system provides highly accurate predictions of the real system performance.

Based on the derived dynamical model, a motion simulator of the MHMP has been constructed. The elements of the motion simulator are build on Linux OS as the simulation engine. The software for dynamical calculation of the MHMP is constructed using C++ programming language. To write the code simply, the promising C++ framework "odeint [19]" for solving ordinary differential equations (Eq. 6.16, 6.17, and 6.18) is used. The fourth Runge-Kutta method is used to update the state-variable $X = [x, \dot{x}, y, \dot{y}, z, \dot{z}]$ in the stepper process. Similar state variables have been defined for the control system's numerical modelings and calculations. Figure 6.16 presents schematically the block diagram of the simulation engine, the PEB teleoperation is re-presented, however the DFR can also be easily implemented. As shown, this engine consists of the following blocks:

- MDU: This block simulates equations of motion (Eq. 6.16, 6.17, and 6.18) and applies an environment's constrains to the motion dynamics.

- CAM: A control allocation matrix (CAM) that maps three virtual inputs $(u_x, u_y, u_z)$ to six real inputs $(i_1, i_2, i_3, i_4, i_5, i_6)$.

- PID: This block simulates the PID controller in the structure of the MUMS.

- FF: This block simulates the feedforward controller in the structure of the MUMS.

- $K_1$ and $K_2$: These are constant parameter blocks for macro-micro scaling $(K_1 \times K_2 = 1)$.

- $C_s$: This block simulates the slave PD controllers in two modes-free motion and hard contact.
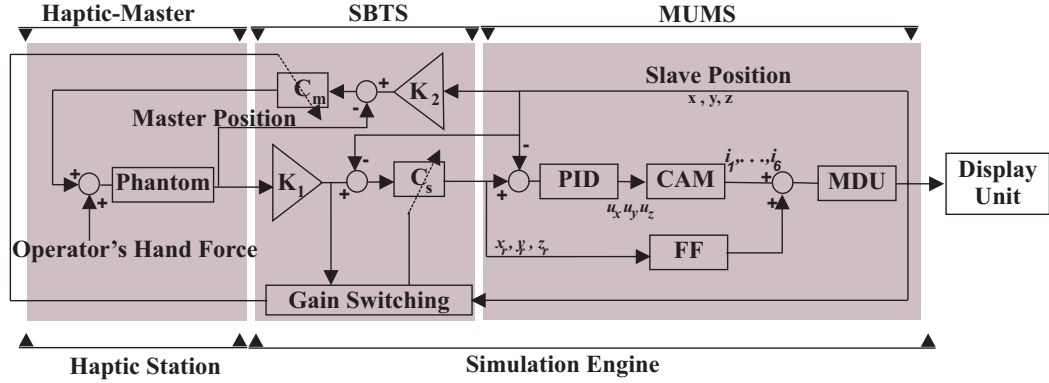
Figure 6.16: Schematic re-presentation of simulation engine's blocks, PEB is realized for the teleoperation

- $C_m$: This block simulates the master PD controllers in two modes-free motion and hard contact.

- Gain Switching: This block determines switching from the free motion to the hard contact and vise versa. The output of this block is sent to the $C_s$ and $C_m$ blocks for switching action.

- Phantom: This block represents the the Phantom Omni haptic device.

In the "simulation mode" of the VRI, the simulation engine sends the position of the microrobot and the geometry of environment to the display unit for demonstration. Furthermore, the simulation engine receives the microrobot's position from the dSPACE real-time controller in the "3D visualization mode", and sends the microrobot's position with the environments's geometry information to the display unit. In both modes of the VRI, the information of the environment is implemented on the the simulation engine.

## 6.4.2  Visualization using 3D computer graphics

The motion simulation corresponding to the above mentioned dynamic calculations is visualized through 3D computer graphics. The useful C++ graphics library "Open Inventor [121]" is used to create 3D visualization; the appearance of the MUMS system visualized through the 3D computer graphics is shown in

Fig. 6.17. In order to show the motion of the levitated object in an easy-to-understand way, the z axis of the coordinate system is depicted as a red line, and an initial stable region for the microrobot is colored in light pink. Additionally, an appearance of the initial state and the appearances of typical 3D motions (x-axis motion, y-axis motion and z-axis motion) are shown in Fig. 6.18. The display unit is equipped with a 3D scene menu bar that affects the way the user can interact with the scene, as shown in Fig. 9. At the bottom and the right edge of the display scene, three thumb wheels and eight buttons:

- Rotx and Roty: these thumb wheels allow the user to rotate the scene about the X and Y axes.

- Dolly: this thumb wheel moves the virtual camera closer to or further from the scene.

- Pointer: this button changes the cursor to a pointer that allows blocks in the scene to be selected.

- Hand: This button changes the cursor to a hand that can be used to rotate, translate, and examine the scene via Dolly, using a combination of mouse buttons and movement.

- Question mark: This button displays help for the viewer.

- Home: this button changes the scene back to its original position.

- Home pointer: this button sets the new home position of the scene to be the scene currently in view.

- Eye: this button resizes the scene that it fully fits into the 3D viewing area.

- Cross-hairs: this button moves the scene so that the object under the cursor is in the center of the viewing area.

- Perspective box: this button switches between perspective and orthogonal views.

Multiple viewports can be generated from the same scenes by the display unit to create more the visual feedbacks for the human operators.

a) overall view

b) zoomed-in view
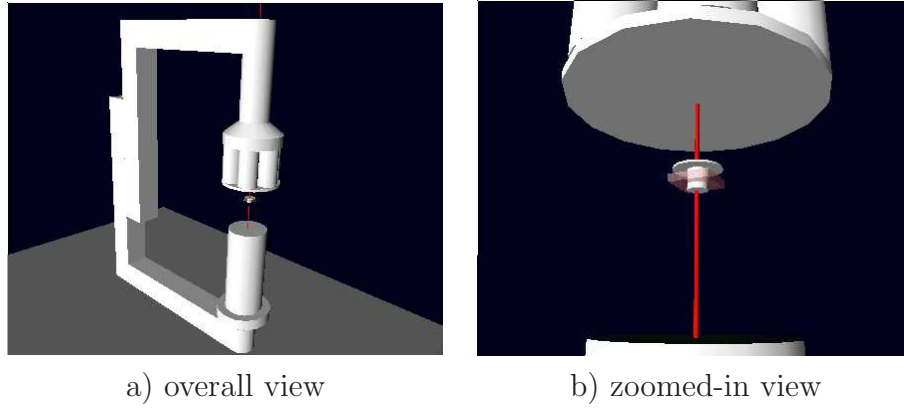
Figure 6.17: 3D computer graphics created by display unit



Red line

Pink region

a) initial position

b) x-axis motion

a) y-axis motion

b) z-axis motion
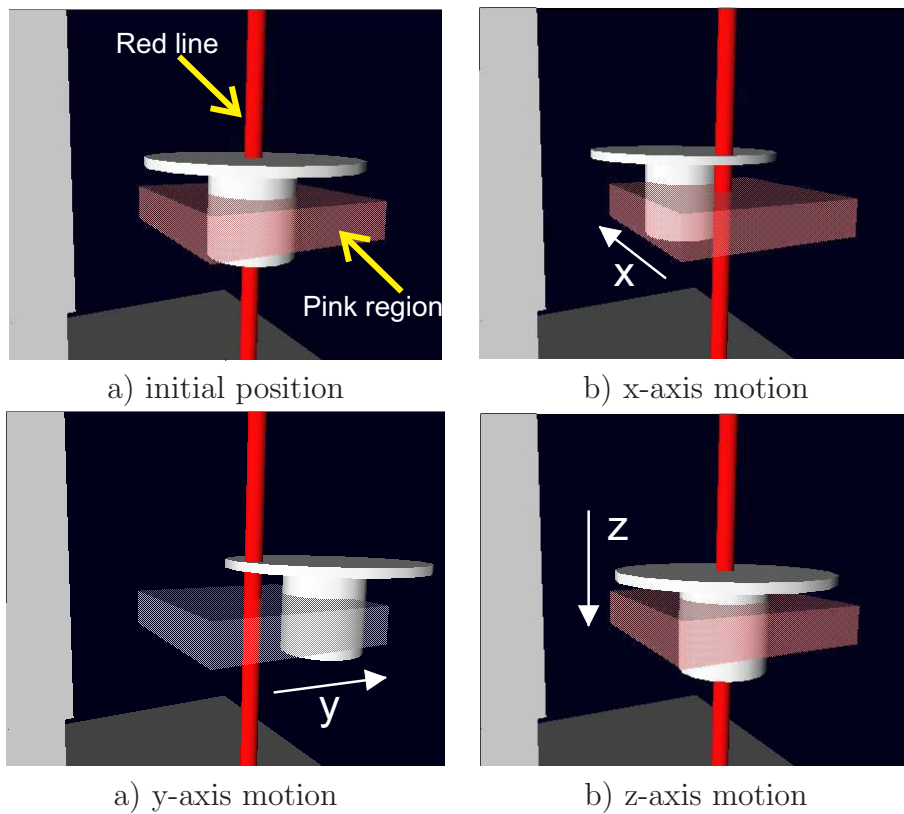
Figure 6.18: General 3D visualization of the microrobot motion by the display unit

134
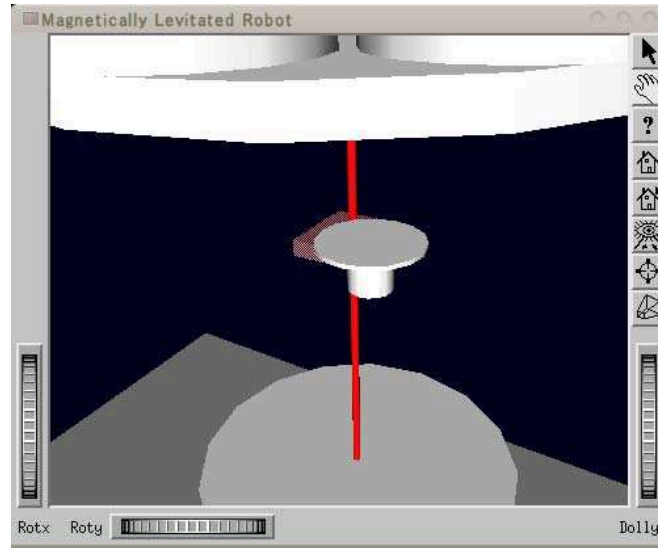
Figure 6.19: Description of the display unit's menu bar

## 6.5   Case study of the VRI

In order to demonstrate the virtual reality motion simulator, a preliminary application of the developed interface has been performed. A cylindrical microrobot has been created on the simulation engine as well as a fixed cubic object that acts as a hard contact in an environment. The human operator uses the Phantom Omni device to command the microrobot on the proposed virtual reality platform in "simulation mode". The operator moves the microrobot in free motion and hard contact with the defined cubic obstacle; Fig. 6.20 demonstrates the 3D computer graphics generated by the display unit.

The experimental results are shown in Fig. 6.21. This figure shows the vertical motion of the microrobot relative to the pole-piece. A hard contact was placed in the z-direction at 0.093 mm from the pole-piece. The gain-switching from free motion to hard contact takes place, and the haptic device applies force to the human operator's hand in the opposite direction. This opposite force allows the human operator to gain information about the obstacle in the microrobot's motion path.

| a) Free motion | b) Hard Contact |
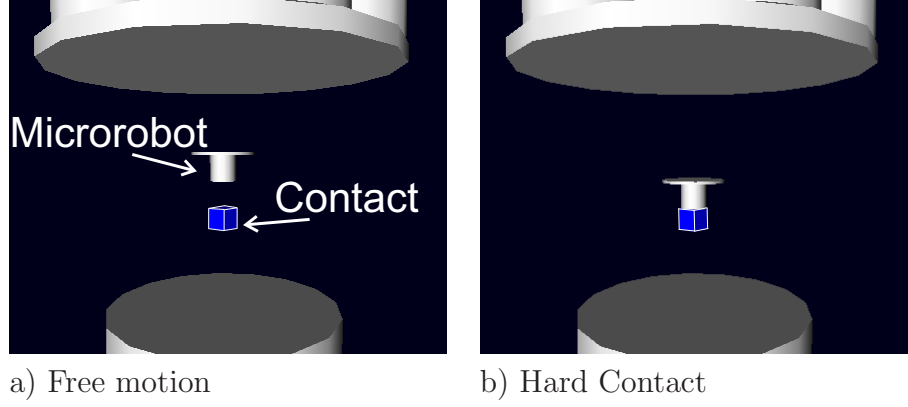
Figure 6.20: 3D visual display of the microrobot in the interaction with an environment

## 6.6 Summary

The MHMP was firstly equipped with position-position teleoperation for free and hard contact conditions in z-direction motions. From several experimental results, it was confirmed that when the slave, microrobot, was in free motion, the slave tracked the scaled trajectory of the master with $RMS$ of tracking error $20 - 40$ $\mu m$, and when the slave was in a contact with an object, an operator could perceive it and keep the contact situation. The robustness of platform in unknown environments has been investigated in various manipulation tasks. The levitated microrobot can be remotely manipulated in a $20 \times 20 \times 30$ $mm^3$ workspace.

Direct-force-reflection teleoperation was also employed to transfer the environmental force to the human operator's hand in the horizontal motion. The Hall-effect based force sensor fedback the applied environmental force to the bilateral control system for the force and position scaling.

This chapter introduced a virtual reality interface (VRI) for a magnetic-haptic micromanipulation platform (MHMP). This interface was constructed based on an experimental dynamical modeling of the magnetic-haptic micromanipulation platform. The VRI enables human operators to improve their skills in using the MHMP, before carrying out an actual dexterous task. The VRI is made up of three main components: a haptic station, a simulation engine, and a display unit. The haptic station provides the operator with the force/torque information from
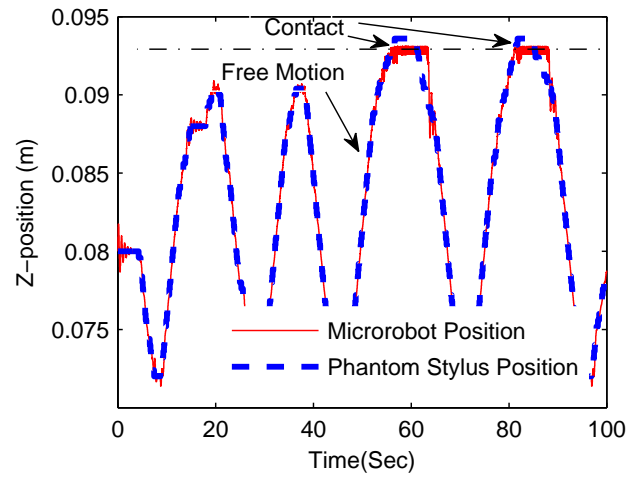
a) Full view
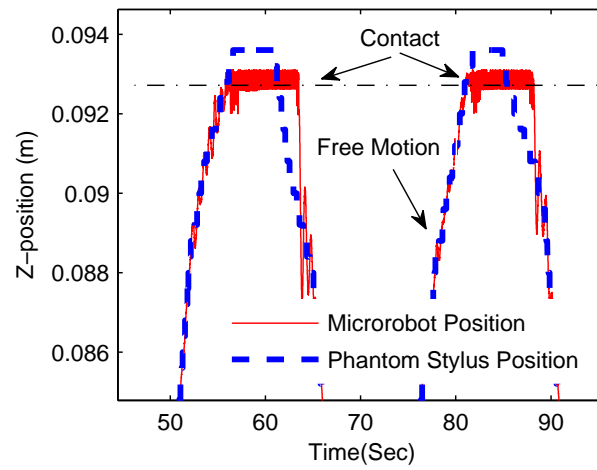


b) Zoomed-in view for the contact status

Figure 6.21: Using PhanTom haptic in experimental measurement of the virtual reality interface in z-direction motions

virtual or remote environments, and is also used to recognize the operator's hand motion command. Dynamical computation and control system modeling have been carried out on the simulation engine. Based on the real-time computation, this engine, as the heart of the system, provides force applied to the operator's hand and the microrobot's position for the haptic station and the display unit, respectively. The display unit employs 3D computer graphics to demonstrate the micromanipulation tasks and environments. The VRI is also developed in such a way that it can be separately used in parallel with the MHMP for the 3D visualization of a real task by providing multiple virtual viewports. This paper introduces the configuration of the proposed VRI, and reports the result

# Chapter 7

# Conclusions and Recommendation

## 7.1  Conclusions

Large gap magnetic actuation systems have provided promise for use in micro-robotic applications such as clean room operations, biological manipulations, and surgical operations. The controlled magnetic field, generated by a series of electromagnets connected by a pole-piece, is used to manipulate a magnetic-based microrobot for high precision manipulations. This magnetic-based propulsion mechanism is integrated with a haptic interface that enables the human operator to intervene in dexterous micro-manipulations or micro-assemblies to compensate the lack of information from the micro-task's environment.

One of the challenges in modeling the dynamics and controlling the system is determining the magnetic force model produced by the magnetic drive unit.With the aid of finite element analyses coupled with the experimental measurements attempts were made to develop mathematical model for the magnetic force. In contrast with most of the proposed magnetic force models in the literature, a simplified linear relations between the magnetic forces and and electromagnets' current are found, these formulas were able to estimate the general trend of the produced magnetic force by the magnetic drive unit. The model was used for the designing of control systems, PID and LQG\LTR methods , with the purpose of the microrobot's high precision manipulation with using the magnetic drive unit.

In experimental investigation of the designed controllers, the 3-D motion of a 11.2 g microrobot prototype was demonstrated in a workspace of $30 \times 32 \times 32$ $mm^3$. The PID control system strategy provides the RMS error at a steady state position is on the order of 9.2 $\mu$m in a vertical direction and 1.9 $\mu$m in a horizontal direction. The second major finding was the axes cross coupling errors, horizontal motion produces an RMS error cross coupling on the order of 170 $\mu$m in the vertical direction. Vertical motion causes insignificant cross coupling in the horizontal direction. However, the LQG\LTR controller reduces the RMS error cross coupling from the previous best of 170 $\mu$m with the PID controller to 18 $\mu$m. The LQG\LTR control system provides high resolution position control very similar to the PID controller, the RMS errors of steady state in horizontal and vertical motion are 10.1 $\mu$m and 2.1 $\mu$m, respectively.

In order to reduce the platform power consumption,a pre-magnetized pole-piece was used that led to a "proof-of-concept" for the system, which is capable of 66% enrgey consumption reduction for our specific microrobot. This pole-piece generates uniform vertical magnetic gradients inside the system workspace to compensate a portion of the microrobot weight, more pole-peice magnetization results in more horzontal and vertical magnetic garadients. Experimental analysis shows that there is trade-off to keep the maneuverability of microrobot on the horizontal plane and to reduce energy consumption, since the horizontal gradients produced by electromagnets cannot overcome the horizontal gradients of the pole-piece in some conditions.

A Higher precision for the horizontal motion of the microrobot was archived by placing an aluminum disk beneath the microrobot's workspace. Coil representation model, loop-of-current equivalent, was employed. to derive the magnetic vector potential of any point in the space. The change in magnetic field of magnetic drive unit was made equivalent with a moving loop of current. Eddy-current density due to the change of magnetic field in the circular plate was calculated. The eddy-current force applied to the aluminum plate was obtained. Since the aluminum plate's position is fixed, equal but opposite in direction force is applied to the microrobot. The experimental measurements coupled with process model system identification validated the proposed analytical relation for the horizontal eddy-current damping. The experiments also verified that placing a conductive

plate underneath the the microrobot, effectively dissipated the excessive portion of levitation force that caused vibrations.

A Hall-effect-based position estimation technique was originated to estimate the microrobot's position in free levitation status when the optical positioning signal was unavailable because of an opaque/blocked environment.A relation was defined between the position of the microrobot and the produced magnetic flux by the magnetic drive unit. The magnetic flux was measured by an arrangement of Hall-effect sensors. Various arrangements of Hall-effect sensors were investigated to find an effective configuration for high accuracy position estimation. Based on the selection of the most effective configuration, the microrobot's motion performance was evaluated through experiment. The experimental investigations led to the "proof-of-concept" of substituting the laser sensors position feedback with Hall-effect sensors. The proposed position estimation technique provided 0.3 mm accuracy in most of the platform working envelope.

To allow the human operator the feeling of a micro-domain task, the micro-domain force estimation method is developed based on the measurement of magnetic flux to measure the environmental force in a single-axis direction . The zero gradient position in the horizontal plane, $B_{max}$ location, was determined based on the magnetic flux measurement. In case that the microrobot is stabilized with environmental force at a position which is not not $B_{max}$ location, the environmental force can be estimated as the function of real-position of the microrobot and estimated $B_{max}$ location. The experimental measurements showed that the accuracy of 1.27 $\mu$N for this novel Hall-effect-based method force estimation. As the main advantage of this method,no force sensor was attached to the microrobot to measure the force, that kept the microrobot's size restriction and made the microrobot inexpensive and disposable for widespread biological applications.

The platform was equipped with position-position and direct-force-reflection teleoperation control systems .Firstly,the position-position teleoperation for free and hard contact conditions in z-direction motions were demonstrated. From several experimental results, it was confirmed that when the slave, microrobot, was in free motion, the slave tracked the scaled trajectory of the master with $RMS$ of tracking error $20 - 40$ $\mu m$, and when the slave was in a contact with an object, an operator could perceive it and keep the contact situation. The

robustness of platform in unknown environments has been investigated in various manipulation tasks. The levitated microrobot can be remotely manipulated in a $20 \times 20 \times 30$ $mm^3$ workspace. Direct-force-reflection teleoperation was also employed to transfer the environmental force to the human operator's hand in the horizontal motion. The Hall-effect based force sensor fedback the applied environmental force to the bilateral control system for the force and position scaling.

A virtual reality interface (VRI) for the MHMP was developed. This interface was constructed based on an experimental dynamical modeling of the magnetic-haptic micro-manipulation platform. The VRI enables human operators to improve their skills in using the MHMP, before carrying out an actual dexterous task. The VRI is made up of three main components: a haptic station, a simulation engine, and a display unit. The haptic station provides the operator with the force/torque information from virtual or remote environments, and is also used to recognize the operator's hand motion command. Dynamical computation and control system modeling have been carried out on the simulation engine. Based on the real-time computation, this engine, as the heart of the system, provides force applied to the operator's hand and the microrobot's position for the haptic station and the display unit, respectively. The display unit employs 3D computer graphics to demonstrate the micro-manipulation tasks and environments. The VRI is also developed in such a way that it can be separately used in parallel with the MHMP for the 3D visualization of a real task by providing multiple virtual viewports.

## 7.2 Recommendations

The developed single-axis force sensing method using magnetic flux measurement serves as suitable starting point for multiple-axes force sensing mechanism. In the proposed method, two Hall-effect sensors were used for the force sensing in y-axis. In a similar way, two Hall-effect sensor can be used for x-axis force measurements. The $B_{max}$ location in the horizontal plane can be estimated by using the measured flux differential for each axis. As explained in the single-axis, the distance of the

microrobot's position from the estimated $B_{max}$ location can be linearly mapped to the environmental force applied to the microrobot in the horizontal plane.

Although the position-position and direct-force-reflection methods have shown promise for bilateral teleoperation, it would be more beneficial to employ a 4-channel bilateral teleoperation method that provides higher order of transparency. In the 4-channel bilateral teleoperation, the force and position for both master and slave are required to be measured. The applied force applied to the haptic device from the human operator can be measured by attaching a force sensor to the haptic device or can be estimated by designing an observer.

The microrobot's position can be precisely controlled by the magnetic drive unit presented in this thesis. It would be more beneficial to modify the microrobot and the magnetic drive unit structure for controlling the microrobot orientations. As initial step toward the orientation control with minimal changes in the current platform, the rolling of the microrobot can be controlled by modifying the microrobot's magnetic head and the control allocation matrix.

# APPENDICES

# Appendix A

# Matlab Source Programs For

# UDP Communication

```
% Initialize dSPACE MLIB
mlib('SelectBoard','DS1006');


% check if the application smdtf_1006_sl.x86 is running
DemoApplName = lower([pwd 'Haptic2CH.x86']);
if mlib('IsApplRunning'),
    ApplInfo = mlib('GetApplInfo');
    if strcmp(DemoApplName,lower(ApplInfo.name)) ~= 1
        err_msg = sprintf('*** This MLIB demo file needs the
         real-time processor application\n*** ''%s'' running!',...
                            DemoApplName);
        error(err_msg);
```

```
    end;
else
    err_msg = sprintf('*** This MLIB demo file needs the real-time
     processor application*** ''%s'' running!',...
                                DemoApplName);
    error(err_msg);
end;


on_off_while={'Model Root/Boolean_while/Value'};

[onoff_while_desc] = mlib('GetTrcVar',on_off_while);

onoff_while = mlib('Read',onoff_while_desc);



on_off_UDP={'Model Root/Boolean_UDP/Value'};

[onoff_UDP_desc] = mlib('GetTrcVar',on_off_UDP);


Pos = {'Model Root/Com/Value'};

[Pos_desc] = mlib('GetTrcVar',Pos);

mlib('SetVarProperty',Pos_desc, 'type','int16');


Forc={'Model Root/Data Type Conversion2/Out1'};

[Forc_desc]=mlib('GetTrcVar',Forc);

mlib('SetVarProperty',Forc_desc, 'type','int16');
```

```
while onoff_while > 0

    onoff_UDP = mlib('Read',onoff_UDP_desc);

    if onoff_UDP > 0

         [mssg,sourceHost] = judp('receive',9081,8,5000);

        Pos_R=str2num(char(mssg)');

        Pos_R=Pos_R*10;

        mlib('Write',Pos_desc,'Data',Pos_R);


        ForceC = mlib('Read',Forc_desc);

        ForceC = num2str(double(ForceC)/1000)

        Force_R= str2num((sprintf('%d %d %d %d %d %d',((ForceC)))));

        judp('send',9081,'129.97.185.67',int8(Force_R))  ;

        judp('send',9081,'129.97.185.71',int8(Force_R))  ;

    end

onoff_while = mlib('Read',onoff_while_desc);

end
```

# Appendix B

# Cantilever-based Force Measurement Accuracy

To investigate the accuracy of the force estimation, firstly the accuracy of force measurement method, cantilever technique, has been calculated. Based on the geometry and material properties tolerances and accuracy of the deflection measurement, the accuracy can calculated by using EulerBernoulli beam deflection and its differential as

$$P = \frac{3EI\delta}{l^3} \tag{B.1}$$

where $E$, $I$, $l$, and $\delta$ are modulus of elasticity, area moment of inertia $(\frac{bh^3}{12})$, length, and elastic deflection, respectively. The error of force measurement by the cantilever method can be derived by differentiating the Eq. 5.14 as,

$$\partial P = \frac{\partial P}{\partial E}dE + \frac{\partial P}{\partial b}db + \frac{\partial P}{\partial h}dh + \frac{\partial P}{\partial l}dl \tag{B.2}$$

The error for modulus of elasticity is 10 percent ($dE = 0.1$), for cantilever cross-section geometrical parameter ($b$ and $l$) the tolerances is $100\mu$m, for the cantilever thickness (h) is 5 $\mu$m, and for leaser accuracy is 5 $\mu$m [Fig. B.1 and Fig. B.2
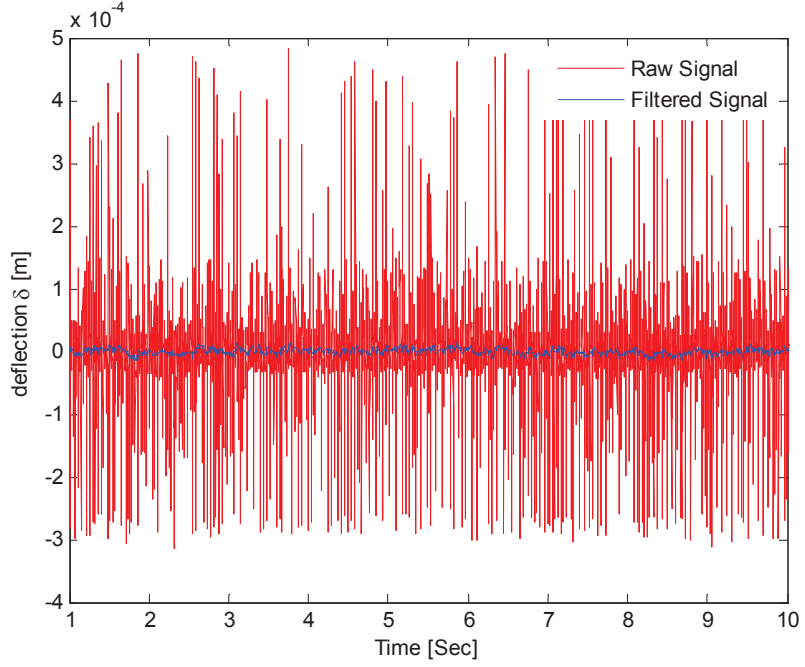
Figure B.1: Comparison of the raw with low-passed filtered measurement of the laser signal

demonstrate the recorded measurement by the laser sensor, the raw and filtered measurement. The RMS of filtered measurement errors is 4.5 $\mu$m. Since a 16 bit analogue output card in the working range of $\pm5$ volt (V) is used for capturing laser outputs in the range of $\pm15$ mm, the resolution for capturing the laser measurements is 0.45 $\mu$m. Therefore the highest accuracy for measuring the cantilever's tip deflection can be calculated as 5 $\mu$m]. Using Eq. B.2, the accuracy of 0.4 $\mu$N for measuring force can be achieved.
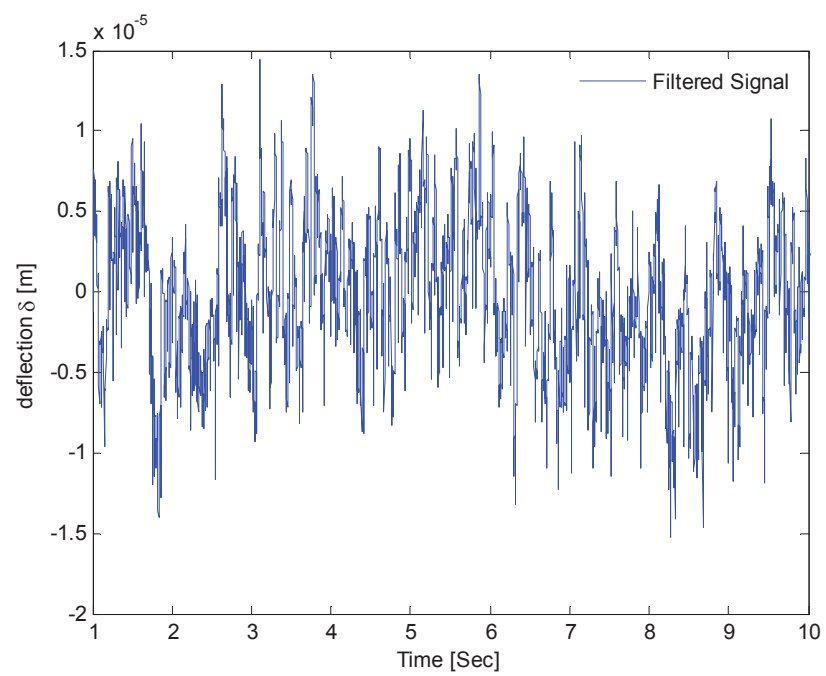
Figure B.2: The filtered measurement of the laser signal

# Appendix C

# List of Publications

## C.1   Patent

1. Non-contact force measurement system for magnetic-based propulsion systems, Provisional USPTO61/850,902,Filed :Feb 26. 2013, M. Mehrtash and M.B. Khamesee

## C.2   Selected Journal Publications

1. <u>Moein Mehrtash</u> and Mir Behrad Khamesee, 2013, "**Modeling and Analysis of Eddy Current Damping for High Precision Magnetic Microrobotic Platform**", Magnetics, IEEE Transactions on (Accepted for publication-In press)

2. <u>Moein Mehrtash</u> and Mir Behrad Khamesee, 2013, "**Micro-domain Force Estimation Using Hall-effect Sensors For A Magnetic Microrobotic Station**", Journal of Advanced Mechanical Design, Systems, and Manufacturing , 7(1). pp. 1-13, DOI : 10.1299/jamdsm.7.1.

3. <u>Moein Mehrtash</u>, Mir Behrad Khamesee, Susumu Tarao, Naoaki Tsuda, and Jen-Yuan Chang, 2012, "**Human-Assisted Virtual Reality for a**

**Magnetic-Haptic Micromanipulation Platform**", Microsystem Technologies, 18(9-10), pp. 1407-1415, Springer, DOI : 10.1007/s00542-012-1560-7.

4. <u>Moein Mehrtash</u>, Mir Behrad Khamesee, Naoaki Tsuda, and Jen-Yuan Chang, 2012, "**Motion Control of a Magnetically Levitated Micro-robot Using Magnetic Flux Measurement**", Microsystem Technologies, 18(9-10), pp. 1417-1424, Springer, DOI : 10.1007/s00542-012-1561-6.

5. <u>Moein Mehrtash</u>, Noaoki Tsuda, and Mir Behrad Khamesee, 2011, "**Bilateral Macro-Micro Teleoperation Using Magnetic Levitation**", *Mechatronics, IEEE/ASME Transactions on*, 16(3), pp. 459-469, DOI : 10.1109 /TMECH.2011.2121090.

6. Saman Hosseini, <u>Moein Mehrtash</u> and Mir Behrad Khamesee, 2011, "**Design, Fabrication and Control of a Magnetic Capsule Robot for the Human Esophagus**", Microsystem Technologies, 17(5-7), pp. 1135-1143, Springer, DOI: 10.1007/s00542-011-1231-0.

7. <u>Moein Mehrtash</u> and Mir Behrad Khamesee, 2011, "**Design and Implementation of LQG\LTR Controller for A Magnetic Telemanipulation System- Performance Evaluation and Energy Saving**", *Microsystem Technologies*, 17(5-7), pp. 1145-1152, Springer, DOI : 10.1007/s00542-010-1210-x.

8. <u>Moein Mehrtash</u>, Ehsan Shameli and Mir Behrad Khamesee, 2010, "**Magnetic Telemanipulation Device With Mass Uncertainty: Modeling, Simulation and Testing**" , *International Journal of Electromagnetics and Mechanics*, 34(4).

# C.3 Selected Conference Publications

1. Susumu Tarao, <u>Moein Mehrtash</u>, Naoaki Tsuda and Mir Behrad Khamesee, "Motion Simulator for Coarse and Fine Motion of Combination of a Magnetically Levitated Micro Robot and an Industrial Macro Robot", *(IEEE ICMA 2013) IEEE International Conference on Mechatronics and Automation (ICMA 2013)*, Takamatsu, Kagawa, Japan, 2013.

2. <u>Moein Mehrtash</u>, and Mir Behrad Khamesee "Micro-domain Force Estimation Using Hall-effect Sensor", *(ASME-ISPS/JSME-IIP 2012) Joint International Conference on Micromechatronics for Information and Precision Equipment* , Santa Clara, California, USA, 2012

3. Susumu Tarao, <u>Moein Mehrtash</u>, Naoaki Tsuda and Mir Behrad Khamesee,"Motion Simulator for a Multi-Degree-of-Freedom Magnetically Levitated Robot",*IEEE/SICE International Symposium on System Integration (SII2011)*, Kyoto, Japan, 2011

4. Susumu Tarao, Naoaki Tsuda, <u>Moein Mehrtash</u> and Mir Behrad Khamesee, "Development of Experimental System for Collaborative Work between a Magnetically Levitated Robot and an Industrial Robot", *JSME Conference on Robotics and Mechantronics*, Okayama, Japan, 2011

5. <u>Moein Mehrtash</u>, Naoaki Tsuda, Tatsuya Nobori, and Mir Behrad Khamesee, "Position Control of a Magnetically Levitated Robot based on Magnetic Flux Measurement ", *ASME International Mechanical Engineering Congress and Exposition*, Denver, Colorado, USA, 2011.

6. Susumu Tarao, Naoaki Tsuda, <u>Moein Mehrtash</u> and Mir Behrad Khamesee, "Motion Simulator for Development of Collaborative Work Planning between a Magnetically Levitated Robot and an Industrial Robot", *ASME International Mechanical Engineering Congress and Exposition*, Denver, Colorado, USA, 2011.

7. <u>Moein Mehrtash</u> and Mir Behrad Khamesee, "Design and Implementation of LQG/LTR for a Magnetic Telemanipulation System", *20th ASME An-*

*nual Conference on Information Storage and Processing Systems*, Santa Clara, CA, USA, 2010.

8. Moein Mehrtash and Mir Behrad Khamesee, "Optimal Motion Control of Magnetically Levitated Microrobot", *6th annual IEEE Conference on Automation Science and Engineering*, Toronto, ON, Canada, 2010.

# Bibliography

[1] Alonso, O., Freixas, L., Canals, J., Susilo, E., Dieguez, A.: Control electronics integration toward endoscopic capsule robot performing legged locomotion and illumination. In: VLSI System on Chip Conference (VLSI-SoC), 2010 18th IEEE/IFIP, pp. 241–246 (2010). ID: 1 7, 8

[2] Ammi, M., Ferreira, A.: Path planning of an afm-based nanomanipulator using virtual force reflection. In: Intelligent Robots and Systems, 2004. (IROS 2004). Proceedings. 2004 IEEE/RSJ International Conference on, vol. 1, pp. 577–582 vol.1 (2004) 125

[3] Ando, N., Korondi, P., Hashimoto, H.: Networked telemicromanipulation systems "haptic loupe". Industrial Electronics, IEEE Transactions on **51**(6), 1259–1271 (2004) 13

[4] Arai, F., Maruyama, H., Sakami, T., Ichikawa, A., Fukuda, T.: Pinpoint injection of microtools for minimally invasive micromanipulation of microbe by laser trap. Mechatronics, IEEE/ASME Transactions on **8**(1), 3–9 (2003) 3

[5] Asbury, C.L., van den Engh, G.: Trapping of dna in nonuniform oscillating electric fields. Biophysical journal **74**(2), 1024–1030 (1998) 3

[6] Basset, P., Kaiser, A., Legrand, B., Collard, D., Buchaillot, L.: Complete system for wireless powering and remote control of electrostatic actuators by inductive coupling. Mechatronics, IEEE/ASME Transactions on **12**(1), 23–31 (2007) 13

[7] Bethea, B., Okamura, A., Kitagawa, M., Fitton, T., Cattaneo, S., Gott, V., Baumgartner, W., Yuh, D.: Application of haptic feedback to robotic surgery. Journal of Laparoendoscopic and Advanced Surgical Techniques-Part A **14**(3), 191–195 (2004) 13

[8] van Breugel, F., Regan, W., Lipson, H.: From insects to machines. Robotics & Automation Magazine, IEEE **15**(4), 68–74 (2008) 7

[9] Burdea, G.C.: Invited review: the synergy between virtual reality and robotics. Robotics and Automation, IEEE Transactions on **15**(3), 400–410 (1999) 125

[10] Butt, H., Cappella, B., Kappl, M.: Force measurements with the atomic force microscope: Technique, interpretation and applications. Surface Science Reports **59**(1), 1–152 (2005) 91

[11] Campbell, J.D., Pillai, P., Goldstein, S.C.: The robot is the tether: Active, adaptive power routing for modular robots with unary inter-robot connectors. In: IEEE/RSJ International Conference on Intelligent Robots and Systems (IROS 2005), pp. 4108–15. Edmonton, Alberta Canada (2005) 7

[12] Carl Zeiss Corp.: Micromanipulation platform. URL http://microscopy.zeiss.com 6

[13] Carpi, F., Pappone, C.: Magnetic robotic manoeuvring of gastrointestinal video capsules: preliminary phantom tests. Biomedicine & Pharmacotherapy **62**(8), 546–549 (2008) 11

[14] Carpi, F., Pappone, C.: Magnetic maneuvering of endoscopic capsules by means of a robotic navigation system. Biomedical Engineering, IEEE Transactions on **56**(5), 1482–1490 (2009) 11

[15] Chen, B.K., Zhang, Y., Sun, Y.: Active release of microobjects using a mems microgripper to overcome adhesion forces. Microelectromechanical Systems, Journal of **18**(3), 652–659 (2009) x, 9, 11, 68

156

[16] Choi, J.S., Yoo, J.: Design of an eddy current brake system using microstructures. Magnetics, IEEE Transactions on **45**(6), 2720 –2723 (2009) 68

[17] Chronis, N., Lee, L.P.: Electrothermally activated su-8 microgripper for single cell manipulation in solution. Microelectromechanical Systems, Journal of **14**(4), 857–863 (2005) x, 9

[18] Clévy, C., Chaillet, N., et al.: Micromanipulation and micro-assembly systems. IEEE/RAS International Advanced Robotics Programm, IARP'06. (2006) x, 5, 9

[19] CPOL: Solving ordinary differential equations in c++ (2009). URL http://www.codeproject.com/KB/recipes/odeint.aspx 131

[20] Craig, D.: Modeling and Control of a Magnetically Levitated Microrobotic System. University of Waterloo, Waterloo, Ont. (2006) 62

[21] Craig, D., Khamesee, M.B.: Motion control of a large gap magnetic suspension system for microrobotic manipulation. Journal of Physics D: Applied Physics **40**(11), 3277 (2007) 11, 12

[22] Craig, D.G., Khamesee, M.B.: Derivation of an analytical model for the force produced during the motion of a magnetically suspended object. In: Mechatronics and Automation, 2005 IEEE International Conference, vol. 2, pp. 970–974 Vol. 2 (2005) 44

[23] Dario, P., Carrozza, M.C., Stefanini, C., D'Attanasio, S.: A mobile microrobot actuated by a new electromagnetic wobble micromotor. Mechatronics, IEEE/ASME Transactions on **3**(1), 9–16 (1998) 6

[24] Desai, J.P., Pillarisetti, A., Brooks, A.D.: Engineering approaches to biomanipulation. Annual Review of Biomedical Engineering pp. Vol. 9, p (2007) 4

[25] Doll, J., Park, S., Pruitt, B.: Design optimization of piezoresistive cantilevers for force sensing in air and water. Journal of applied physics **106**(6), 064,310–064,310 (2009) 91

[26] Doyle, J.: Guaranteed margins for lqg regulators. Automatic Control, IEEE Transactions on **23**(4), 756–757 (1978) 62

[27] Doyle, J.C., Stein, G.: Robustness with observers. In: Decision and Control including the 17th Symposium on Adaptive Processes, 1978 IEEE Conference on, vol. 17, pp. 1–6 (1978) 62

[28] dSPACE Inc., Germany: Hardware installation and configuration reference, release 6.3 (2010) 35

[29] Dubey, R.V., Chan, T.F., Everett, S.E.: Variable damping impedance control of a bilateral telerobotic system. Control Systems Magazine, IEEE **17**(1), 37–45 (1997) 13

[30] Duc, T., Creemer, J., Sarro, P.: Piezoresistive cantilever beam for force sensing in two dimensions. Sensors Journal, IEEE **7**(1), 96–104 (2007) 91

[31] Ebrahimi, B., Khamesee, M.B., Golnaraghi, F.: A novel eddy current damper: theory and experiment. Journal of Physics D: Applied Physics **42**(7), 075,001 (2009) 68

[32] Elbuken, C.: Magnetic levitation of polymeric photo-thermal microgrippers. University of Waterloo, Waterloo, Ont. (2009) x, 4, 8

[33] Elbuken, C., Khamesee, M.B., Yavuz, M.: Eddy current damping for magnetic levitation: downscaling from macro- to micro-levitation. Journal of Physics D: Applied Physics **39**(18), 3932 (2006) 56, 67, 68, 69, 85

[34] Elbuken, C., Khamesee, M.B., Yavuz, M.: Design and implementation of a micromanipulation system using a magnetically levitated mems robot. Mechatronics, IEEE/ASME Transactions on **14**(4), 434–445 (2009) 7, 11

[35] Elbuken, C., Shameli, E., Khamesee, M.B.: Modeling and analysis of eddy-current damping for high-precision magnetic levitation of a small magnet. Magnetics, IEEE Transactions on **43**(1), 26 –32 (2007) xii, 56, 67, 68, 69, 78, 79

[36] Estevez, P., Khan, S., Lambert, P., Porta, M., Polat, I., Scherer, C., Tichem, M., Staufer, U., Langen, H., Schmidt, R.: A Haptic Tele-operated System for Microassembly, *Precision Assembly Technologies and Systems*, vol. 315, pp. 13–20. Springer Boston (2010) 13

[37] Fallaha, C., Kanaan, H., Saad, M.: Real time implementation of a sliding mode regulator for current-controlled magnetic levitation system. In: Intelligent Control, 2005. Proceedings of the 2005 IEEE International Symposium on, Mediterrean Conference on Control and Automation, pp. 696–701 (2005) 44

[38] Fatikow, S., Seyfried, J., Fahlbusch, S., Buerkle, A., Schmoeckel, F.: A flexible microrobot-based microassembly station. J. Intell. Robotics Syst. **27**(1-2), 135–169 (2000) 5

[39] Ferreira, A., Cassier, C., Hirai, S.: Automatic microassembly system assisted by vision servoing and virtual reality. Mechatronics, IEEE/ASME Transactions on **9**(2), 321–333 (2004) 125

[40] Fukuda, T., Hosokai, H., Ohyama, H., Hashimoto, H., Arai, F.: Giant magnetostrictive alloy (gma) applications to micro mobile robot as a micro actuator without power supply cables. In: Micro Electro Mechanical Systems, 1991, MEMS '91, Proceedings. An Investigation of Micro Structures, Sensors, Actuators, Machines and Robots. IEEE, pp. 210–215 (1991) 10

[41] Fung, C.K.M., Elhajj, I., Li, W.J., Xi, N.: A 2-d pvdf force sensing system for micro-manipulation and micro-assembly. In: Robotics and Automation, 2002. Proceedings. ICRA '02. IEEE International Conference on, vol. 2, pp. 1489–1494 vol.2 (2002) 10

[42] Goldstein, S.C., Mowry, T.C.: Claytronics: A scalable basis for future robots. In: RoboSphere 2004. Moffett Field, CA (2004) 6

[43] Gosline, A.H.C., Hayward, V.: Dual-channel haptic synthesis of viscoelastic tissue properties using programmable eddy current brakes. The International Journal of Robotics Research **28**(10), 1387–1399 (2009) 68

[44] Gosse, C., Croquette, V.: Magnetic tweezers: Micromanipulation and force measurement at the molecular level. Biophysical journal **82**(6), 3314–3329 (2002) 3

[45] Griesbach, T., Wurz, M., Rissing, L.: Modular eddy current micro sensor. Magnetics, IEEE Transactions on **47**(10), 3760 –3763 (2011) 68

[46] Guo, S., Pan, Q., Khamesee, M.: Development of a novel type of microrobot for biomedical application. Microsystem Technologies **14**(3), 307–314 (2008) 7, 8

[47] Hamdi, M., Ferreira, A.: Microassembly planning using physical-based models in virtual environment. In: Intelligent Robots and Systems, 2004. (IROS 2004). Proceedings. 2004 IEEE/RSJ International Conference on, vol. 4, pp. 3369–3374 vol.4 (2004) 125

[48] Hoffmann, T., Eilebrecht, B., Leonhardt, S.: Respiratory monitoring system on the basis of capacitive textile force sensors. Sensors Journal, IEEE **11**(5), 1112–1119 (2011) 91

[49] Ida, N.: Electromagnetics and calculation of fields. Springer, New York (1997) 29, 30

[50] Jalili-Kharaajoo, M.: Robust variable structure control applied to voltage-controlled magnetic levitation systems. In: Industrial Informatics, 2004. INDIN '04. 2004 2nd IEEE International Conference on, pp. 335–338 (2004) 44

[51] Jung, K.S., Baek, Y.S.: Study on a novel contact-free planar system using direct drive dc coils and permanent magnets. Mechatronics, IEEE/ASME Transactions on **7**(1), 35–43 (2002) 11

[52] Kasaya, T., Miyazaki, H., Saito, S., Sato, T.: Micro object handling under sem by vision-based automatic control. In: Robotics and Automation, 1999. Proceedings. 1999 IEEE International Conference on, vol. 3, pp. 2189–2196 vol.3 (1999) 9, 10

[53] Keyence Corporation, Japan: High speed laser scan micrometer ls-5000 series instruction manual (1996) xi, 38

[54] Khamesee, M.B., Kato, N., Nomura, Y., Nakamura, T.: Design and control of a microrobotic system using magnetic levitation. Mechatronics, IEEE/ASME Transactions on **7**(1), 1–14 (2002) 12, 24, 25

[55] Khamesee, M.B., Shameli, E.: Pole piece effect on improvement of magnetic controllability for noncontact micromanipulation. Magnetics, IEEE Transactions on **43; 43**(2), 533–542 (2007) 11, 12, 24, 25, 27

[56] Khan, S., Sabanovic, A.: Force feedback pushing scheme for micromanipulation applications. Journal of Micro - Nano Mechatronics **5**(1), 43–55 (2009) 13

[57] Kim, B., Park, S., Park, J.O.: Microrobots for a capsule endoscope. In: Advanced Intelligent Mechatronics, 2009. AIM 2009. IEEE/ASME International Conference on, pp. 729–734 (2009) 7

[58] Kim, D.H., Kim, B., Kang, H., Ju, B.K.: Development of a piezoelectric polymer-based sensorized microgripper for microassembly and micromanipulation. In: Intelligent Robots and Systems, 2003. (IROS 2003). Proceedings. 2003 IEEE/RSJ International Conference on, vol. 2, pp. 1864–1869 vol.2 (2003) 10

[59] Kim, J.H., Menq, C.H.: Visual servo control achieving nanometer resolution in . Robotics, IEEE Transactions on **25**(1), 109–116 (2009) 5

[60] jong Kim, W., Verma, S.: Multiaxis maglev positioner with nanometer resolution over extended travel range. Journal of Dynamic Systems, Measurement, and Control **129**(6), 777–785 (2007) 11

[61] Koyano, K., Sato, T.: Micro object handling system with concentrated visual fields and new handling skills. In: Robotics and Automation, 1996. Proceedings., 1996 IEEE International Conference on, vol. 3, pp. 2541–2548 vol.3 (1996) 9

[62] Lan, C.C., Lin, C.M., Fan, C.H.: A self-sensing microgripper module with wide handling ranges. Mechatronics, IEEE/ASME Transactions on **PP**(99), 1–10 (2010) 5

[63] Lawrence, D.A.: Stability and transparency in bilateral teleoperation. Robotics and Automation, IEEE Transactions on **9**(5), 624–637 (1993) 14, 109, 111

[64] Lee, H., Hunt, T.P., Westervelt, R.M.: Magnetic and electric manipulation of a single cell in fluid. In: Nanoengineered Assemblies and Advanced Micro-Nanosystems, pp. 17–24. (1)Dept. of Phys., Harvard Univ., Cambridge, MA, USA, USA (2004) 4

[65] Lewis, F.L.: Optimal control. New York ; Toronto : Wiley, New York ; Toronto (1986) 62

[66] Li, Y., Xu, Q.: A totally decoupled piezo-driven xyz flexure parallel micropositioning stage for micro/nanomanipulation. Automation Science and Engineering, IEEE Transactions on **8**(2), 265 –279 (2011) x, 4

[67] Lin, F.J., Teng, L.T., Shieh, P.H.: Intelligent adaptive backstepping control system for magnetic levitation apparatus. Magnetics, IEEE Transactions on **43**(5), 2009–2018 (2007) 44

[68] Liu, W., Jia, X., Wang, F., Jia, Z.: An in-pipe wireless swimming micro-robot driven by giant magnetostrictive thin film. Sensors and Actuators A: Physical **160**(1-2), 101–108 (2010) 7

[69] Ljung, L.: System Identification Toolbox – For Use With MATLAB. The Mathworks, Inc., Natick, MA (2006) 83

[70] Lu, Z., Chen, P.C.Y., Lin, W.: Force sensing and control in micromanipulation. Systems, Man, and Cybernetics, Part C: Applications and Reviews, IEEE Transactions on **36**(6), 713–724 (2006) 10

[71] Mathieu, J.B., Martel, S.: Mri-based magnetic navigation of nanomedical devices for drug delivery and hyperthermia in deep tissues. In: Nanotechnol-

ogy, 2007. IEEE-NANO 2007. 7th IEEE Conference on, vol. 1, pp. 312–315 (2007) 11

[72] Maxwell, J.C.: On the induction of electric currents in an infinite plane sheet of uniform conductivity. Proceedings of the Royal Society of London **20**(130-138), 159–168 (1871) 72

[73] Mehrtash, M., Shameli, E., Khamesee, M.B.: Magnetic telemanipulation device with mass uncertainty: Modeling, simulation and testing. International Journal of Applied Electromagnetic and Mechanics **34**(4), 211–223 (2010) 82

[74] Mehrtash, M., Tsuda, N., Khamesee, M.B.: Bilateral macro/micro teleoperation using magnetic levitation. Mechatronics, IEEE/ASME Transactions on **16**(3), 459 –469 (2011) xii, 68, 80, 82

[75] Mlhave, K., Wich, T., Kortschack, A., Bggild, P.: Pick-and-place nanomanipulation using microfabricated grippers. Nanotechnology **17**(10), 2434 (2006) 8

[76] Nakamura, T., Khamesee, M.: A prototype mechanism for three-dimensional levitated movement of a small magnet. Mechatronics, IEEE/ASME Transactions on **2**(1), 41–50 (1997) 11, 12, 91

[77] Ni, L., Wang, D.W.L.: A gain-switching control scheme for position-error-based bilateral teleoperation: Contact stability analysis and controller design. The International Journal of Robotics Research **23**(3), 255–274 (2006) 14, 109, 110, 113, 115

[78] Ohji, T., Hara, H., Amei, K., Sakui, M.: Three-dimensional motion of a small object by using a new magnetic levitation system having four i-shaped electromagnets. Magnetics, IEEE Transactions on **44; 44**(11), 4159–4162 (2008) 11

[79] Oppenheimer, M.W., Doman, D.B., Bolender, M.A.: Control allocation for over-actuated systems. In: Control and Automation, 2006. MED '06. 14th Mediterranean Conference on, pp. 1–6 (2006) 60

[80] Palmer, B.S.: Current density and forces for a current loop moving parallel over a thin conducting sheet. European Journal of Physics **25**(5), 655 (2004) 72, 73, 74

[81] Park, H., Park, S., Yoon, E., Kim, B., Park, J., Park, S.: Paddling based microrobot for capsule endoscopes. In: Robotics and Automation, 2007 IEEE International Conference on, pp. 3377–3382 (2007) 7

[82] Park, S., Doll, J., Pruitt, B.: Piezoresistive cantilever performancepart i: Analytical model for sensitivity. Microelectromechanical Systems, Journal of **19**(1), 137–148 (2010) 91

[83] Park, S., Doll, J., Rastegar, A., Pruitt, B.: Piezoresistive cantilever performancepart ii: optimization. Microelectromechanical Systems, Journal of **19**(1), 149–161 (2010) 91

[84] Park, S., Petzold, B., Goodman, M., Pruitt, B.: Piezoresistive cantilever force-clamp system. Review of Scientific Instruments **82**(4), 043,703–043,703 (2011) 91

[85] Peterson, K.S., Grizzle, J.W., Stefanopoulou, A.G.: Nonlinear control for magnetic levitation of automotive engine vales. Control Systems Technology, IEEE Transactions on **14**(2), 346–354 (2006) 44

[86] Phuah, J., Lu, J., Yasser, M., Yahagi, T.: Neuro-sliding mode control for magnetic levitation systems. In: Circuits and Systems, 2005. ISCAS 2005. IEEE International Symposium on, pp. 5130–5133 Vol. 5 (2005) 44

[87] Plissi, M.V., Torrie, C.I., Barton, M., Robertson, N.A., Grant, A., Cantley, C.A., Strain, K.A., Willems, P.A., Romie, J.H., Skeldon, K.D., Perreur-Lloyd, M.M., Jones, R.A., Hough, J.: An investigation of eddy-current damping of multi-stage pendulum suspensions for use in interferometric gravitational wave detectors. Review of Scientific Instruments **75**(11), 4516–4522 (2004) 68

[88] Polit, S., Dong, J.: Development of a high-bandwidth xy nanopositioning stage for high-rate micro-/nanomanufacturing. Mechatronics, IEEE/ASME Transactions on **16**(4), 724 –733 (2011) x, 4

[89] Probst, M., Hurzeler, C., Borer, R., Nelson, B.: Virtual reality for microassembly. In: Society of Photo-Optical Instrumentation Engineers (SPIE) Conference Series, vol. 6718 (2007) 125

[90] Rakotondrabe, M., Haddab, Y., Lutz, P.: Development, modeling, and control of a micro-/nanopositioning 2-dof stickslip device. Mechatronics, IEEE/ASME Transactions on **14**(6), 733–745 (2009) 5

[91] Reitz, J.R.: Forces on moving magnets due to eddy currents. Journal of Applied Physics **41**(5), 2067–2071 (1970) 72

[92] Saito, S., Miyazaki, H., Sato, T.: Pick and place operation of a micro-object with high reliability and precision based on micro-physics under sem. In: Robotics and Automation, 1999. Proceedings. 1999 IEEE International Conference on, vol. 4, pp. 2736–2743 (1999) 9

[93] Salcudean, S.E., Hashtrudi-Zaad, K., Tafazoli, S., DiMaio, S.P., Reboulet, C.: Bilateral matched impedance teleoperation with application to excavator control. In: Robotics and Automation, 1998. Proceedings. 1998 IEEE International Conference on, vol. 1, pp. 133–139 vol.1 (1998) 13

[94] Salerno, M., Ciuti, G., Lucarini, G., Rizzo, R., Valdastri, P., Menciassi, A., Landi, A., Dario, P.: A discrete-time localization method for capsule endoscopy based on on-board magnetic sensing. Measurement Science and Technology **23**(1), 015,701 (2012) 11

[95] Savia, M., Koivo, H.N.: Contact micromanipulationsurvey of strategies. Mechatronics, IEEE/ASME Transactions on **14**(4), 504–514 (2009) 1, 12

[96] Schmoeckel, F., Fatikow, S.: Smart flexible microrobots for scanning electron microscope (sem) applications. Journal of Intelligent Material Systems and Structures **11**(3), 191–198 (2000) 5, 8

[97] Schweikardt, E.: Current trends and miniaturization challenges for modular self-reconfigurable robotics Modrobotics 6

[98] Sensible Technologies: Phantom omni technical specification (2010) ix, xi, 39, 41

[99] Shameli, E.: Design, implementation and control of a magnetic levitation device. University of Waterloo, Waterloo, Ont. (2008) 19, 28, 36, 44, 50

[100] Shen, Y., Xi, N., Wejinya, U.C., Li, W.J.: High sensitivity 2-d force sensor for assembly of surface mems devices. In: Intelligent Robots and Systems, 2004. (IROS 2004). Proceedings. 2004 IEEE/RSJ International Conference on, vol. 4, pp. 3363–3368 vol.4 (2004) 10

[101] Sieber, A., Valdastri, P., Houston, K., Eder, C., Tonet, O., Menciassi, A., Dario, P.: A novel haptic platform for real time bilateral biomanipulation with a mems sensor for triaxial force feedback. Sensors and Actuators A: Physical **142**(1), 19 (2008) 13

[102] Simi, M., Sardi, G., Valdastri, P., Menciassi, A., Dario, P.: Magnetic levitation camera robot for endoscopic surgery. In: Robotics and Automation (ICRA), 2011 IEEE International Conference on, pp. 5279–5284. IEEE (2011) 11

[103] Simi, M., Valdastri, P., Quaglia, C., Menciassi, A., Dario, P.: Design, fabrication, and testing of a capsule with hybrid locomotion for gastrointestinal tract exploration. Mechatronics, IEEE/ASME Transactions on **15**(2), 170–180 (2010) 7

[104] Sleep, J., Wilson, D., Simmons, R., Gratzer, W.: Elasticity of the red cell membrane and its relation to hemolytic disorders: An optical tweezers study. Biophysical journal **77**(6), 3085–3095 (1999) 3

[105] Smith, S.B., Cui, Y., Bustamante, C.: Overstretching b-dna: The elastic response of individual double-stranded and single-stranded dna molecules. Science **271**(5250), 795–799 (1996) 3

[106] Smythe, W.R.: Static and Dynamic Electricity, 2ed edn. McGraw-Hill, New York (1950) 73

[107] Sodano, H.A., Bae, J.S.: Eddy current damping in structures. The Shock and Vibration Digest **36**(6), 469478 (2004) 68

[108] Souza, G.R., Molina, J.R., Raphael, R.M., Ozawa, M.G., Stark, D.J., Levin, C.S., Bronk, L.F., Ananta, J.S., Mandelin, J., Georgescu, M.M., Bankson, J.A., Gelovani, J.G., C., K., Arap, W., Pasqualini, R.: Three-dimensional tissue culture based on magnetic cell levitation. Nat Nano **5**(4), 291–296 (2010) 3, 5

[109] Spero, R., Vicci, L., Cribb, J., Bober, D., Swaminathan, V., O'Brien, E., Rogers, S., Superfine, R.: High throughput system for magnetic manipulation of cells, polymers, and biomaterials. Rev Sci Instrum **79**(8), 083,707 (2008) 4, 5

[110] Srivastava, R., Kumar, S.: An alternative approach for calculation of braking force of an eddy-current brake. Magnetics, IEEE Transactions on **45**(1), 150 –154 (2009) 68

[111] Stratton, J.A.: Electromagnetic theory. Hoboken, New Jersey : John Wiley and Sons, Inc, Hoboken, New Jersey (2007) 20, 21

[112] Sun, Y., Ho, Y.S., Yu, L.: Dynamic stiffnesses of active magnetic thrust bearing including eddy-current effects. Magnetics, IEEE Transactions on **45**(1), 139 –149 (2009) 68

[113] Talasaz, A., Patel, R.V., Naish, M.D.: Haptics-enabled teleoperation for robot-assisted tumor localization. In: Robotics and Automation (ICRA), 2010 IEEE International Conference on, pp. 5340–5345 (2010) 13

[114] Tamadazte, B., Piat, N.L.F., Dembl, S.: Robotic micromanipulation and microassembly using monoview and multiscale visual servoing. Mechatronics, IEEE/ASME Transactions on **16**(2), 277–287 (2011) 5

[115] Tamaz, S., Gourdeau, R., Chanu, A., Mathieu, J.B., Martel, S.: Real-time mri-based control of a ferromagnetic core for endovascular navigation. Biomedical Engineering, IEEE Transactions on **55; 55**(7), 1854–1863 (2008) 11, 68

[116] Tavakoli, M.: Haptics for teleoperated surgical robotic systems. Hackensack, N.J. : World Scientific (2008) 13, 118, 121

[117] Vertessy, B.G., Steck, T.L.: Elasticity of the human red cell membrane skeleton. effects of temperature and denaturants (1989) 3

[118] Vlachos, K., Papadopoulos, E.: Analysis and experiments of a haptic telemanipulation environment for a microrobot driven by centripetal forces. Journal of Computing and Information Science in Engineering **8**(4), 041,007–9 (2008) 13

[119] Wang, J., Atallah, K., Chin, R., Arshad, W., Lendenmann, H.: Rotor eddy-current loss in permanent-magnet brushless ac machines. Magnetics, IEEE Transactions on **46**(7), 2701 –2707 (2010) 68

[120] Wang, L., Mills, J., Cleghorn, W.: Automatic microassembly using visual servo control. Electronics Packaging Manufacturing, IEEE Transactions on **31**(4), 316 –325 (2008) 6

[121] Wernecke, J.: The Inventor Mentor: Programming Object-Oriented 3D Graphics with Open Inventor, Release 2. Addison-Wesley Publishing Company, Boston, Massachusetts (1994) 132

[122] Xie, H., Rgnier, S.: Three-dimensional automated micromanipulation using a nanotip gripper with multi-feedback. Journal of Micromechanics and Microengineering **19**(7), 075,009 (2009) 91

[123] Yamamoto, Y., Konishi, R., Negishi, Y., Kawakami, T.: Prototyping ubiquitous micro-manipulation system. In: Advanced Intelligent Mechatronics, 2003. AIM 2003. Proceedings. 2003 IEEE/ASME International Conference on, vol. 2, pp. 709–714 vol.2 (2003) 10

[124] Yim, S., Sitti, M.: Design and rolling locomotion of a magnetically actuated soft capsule endoscope. Robotics, IEEE Transactions on **28**(1), 183–194 (2012) 11

[125] Yoshida, E., Murata, S., Kokaji, S., Tomita, K., Kurokawa, H.: Micro self-reconfigurable robotic system using shape memory alloy. Distributed autonomous robotic systems **4**, 145–154 (2000) 7

[126] Zareinejad, M., Rezaei, S.M., Abdullah, A., Ghidary, S.S.: Development of a piezo-actuated micro-teleoperation system for cell manipulation. International Journal of Medical Robotics and Computer Assisted Surgery **5**(1), 66–76 (2009) 13

[127] Zhang, H., Burdet, E., Poo, A.N., Hutmacher, D.W.: Microassembly fabrication of tissue engineering scaffolds with customized design. Automation Science and Engineering, IEEE Transactions on **5**(3), 446–456 (2008) x, 5, 9, 13

[128] Zhang, Y., Chen, B.K., Liu, X., Sun, Y.: Autonomous robotic pick-and-place of micro-objects. Robotics, IEEE Transactions on **26**(1), 200–207 (2010) 5

[129] Zhang, Y., Cong, M., Guo, D., Wang, D.: Design optimization of a bidirectional microswimming robot using giant magnetostrictive thin films. Mechatronics, IEEE/ASME Transactions on **14**(4), 493–503 (2009) 7

[130] Zhang, Z., Menq, C.H.: Six-axis magnetic levitation and motion control. Robotics, IEEE Transactions on **23**(2), 196–205 (2007) 11

[131] Zhou, Q., Kallio, P., Koivo, H.N.: Virtual environment for operations in the microworld. In: B. Nelson, B. J., J.-M. (eds.) Microrobotics and Microassembly II, pp. 56–64. SPIE, USA (2000) 125